Spring 2006

Measurement of the partial cross-sections sigmaTT, sigmaLT and sigmaT + epsilon-sigmaL of the p(e,e'pion+)n reaction at the Delta(1232) resonance

John M. Kirkpatrick
University of New Hampshire, Durham

Measurement of the Partial Cross Sections σ_{TT}, σ_{LT} and $\sigma_T + \varepsilon\sigma_L$ of the $p(e, e'\pi^+)n$ Reaction at the $\Delta(1232)$ Resonance

BY

John M. Kirkpatrick

B.A., University of Southern Maine, 1996
M.S., University of New Hampshire, 2001

DISSERTATION

Submitted to the University of New Hampshire
in partial fulfillment of
the requirements for the degree of

Doctor of Philosophy

in

Physics

May 2006

UMI Number: 3217427

INFORMATION TO USERS

The quality of this reproduction is dependent upon the quality of the copy
submitted. Broken or indistinct print, colored or poor quality illustrations and
photographs, print bleed-through, substandard margins, and improper
alignment can adversely affect reproduction.

In the unlikely event that the author did not send a complete manuscript
and there are missing pages, these will be noted. Also, if unauthorized
copyright material had to be removed, a note will indicate the deletion.

UMI®

UMI Microform 3217427

Copyright 2006 by ProQuest Information and Learning Company.

All rights reserved. This microform edition is protected against

unauthorized copying under Title 17, United States Code.

ProQuest Information and Learning Company
300 North Zeeb Road
P.O. Box 1346
Ann Arbor, MI 48106-1346

This dissertation has been examined and approved.

Director, John R. Calarco
Professor of Physics

F. W. Hersman
Professor of Physics

John F. Dawson
Professor of Physics

Maurik Holtrop
Professor of Physics

Aron Bernstien
Professor of Physics (Massachusetts Institute of Technology)

10/5/05
Date

Dedication

For Jane, Kalli, Erica and Mary, who have been my constant support.

Table of Contents

v

List of Tables

List of Figures

x

ABSTRACT

MEASUREMENT OF THE PARTIAL CROSS SECTIONS σ_{TT}, σ_{LT} AND $\sigma_T + \varepsilon\sigma_L$ OF

THE $p(e,e'\pi^+)n$ REACTION AT THE $\Delta(1232)$ RESONANCE

by

John M. Kirkpatrick
University of New Hampshire, May, 2006

The partial cross-sections σ_{LT}, σ_{TT}, and $\sigma_T + \varepsilon\sigma_L$ have been measured for the $H(e,e'\pi^+)n$ reaction, at $Q^2 = 0.127$ (GeV/c)^2, $W = 1232$ MeV and $\theta_{\pi q} = 44.45°$, in a recent experiment at the MIT/Bates Linear Accelerator Center. The experiment was done with the Bates Out Of Plane Spectrometer system (OOPS) using a high duty factor ($> 50\%$) 950 MeV unpolarized electron beam. The One Hundred Inch Proton Spectrometer (OHIPS) detected electrons, and three OOPS modules provided out of plane ha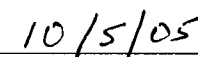dron detection in two sequential sets of simultaneous measurements. The σ_{LT} partial cross section is sensitive to the coulombic quadrupole amplitude C2, and can be used to extract the ratio (CMR) of C2 to the dominant magnetic dipole (M1) amplitude, and σ_{TT} is similarly sensitive to the electric quadrupole (E2) amplitude and can be used to evaluate the E2 to M1 ratio (EMR). These measurements in the π^+ channel complement π^0 channel measurements of the same responses which were made during the same experiment; the different sensitivities to background terms in the two charge channels will provide increased precision in the CMR and EMR extraction, and permit isospin decomposition of the multipoles.

CHAPTER 1

Introduction

1.1 Physics Motivation

The proton is one of the primary building blocks of our day-to-day world; a full understanding of its structure and properties, as well as the properties of the other hadrons, are of basic importance to our scientific understanding of nature. This is one of the primary goals of nuclear physics. In an ideal situation, such properties should be calculable from fundamental principles. The development of the quark hypothesis in the late 1960's represented a major step toward this goal. Indeed, a broad range of hadronic phenomenology can be explained in terms of the $SU(2) \otimes SU(3)$ spin-flavor group structure of the quark picture alone. In this modern viewpoint, the proton is the bound state of three spin-1/2 quarks interacting through the exchange of virtual gluons – the mediating Bosons of the strong nuclear force. The strong force is believed to be well understood at the fundamental level, and to be completely described by the theory of Quantum Chromodynamics (QCD)[1].

Ideally, then, a fundamental nuclear theory should be able to describe the properties of the proton (or any other hadron) exactly, in terms of QCD and quark degrees of freedom. This would be analogous to the situation in Quantum Electrodynamics (QED), where, for example, the structure of the hydrogen atom may be solved *exactly* in terms of the

---

[1]That is, we know how to write down the Lagrangian and from it derive the field equations

1

electromagnetic interaction between the proton and electron.

The strong force is not so cooperative. Unlike QED, where the photons carry no charge themselves, the gluons do carry (color) charge and interact not only with the quarks but with each other. This self-coupling of the field makes the group structure non-Abelian, and the equations describing strong interactions much more complicated. There is no such thing in QCD as a simple 2-body analog to the hydrogen atom.

In QED complexity is not in and of itself an insurmountable problem; by means of well established perturbation techniques one is able to treat atoms of much greater complexity than hydrogen, to (in principle) arbitrary accuracy. Such techniques fail when applied to strong interactions, however, due to another effect of the field self-coupling: quark confinement. Whereas the electromagnetic coupling factor is small ($\alpha \approx 1/137$) and nearly independent of the momentum transfer Q^2, the strong force coupling constant increases dramatically with decreasing energy (and therefore increasing distance) scales. In the low-Q^2 region appropriate to the exploration of nucleon structure, perturbation expansions do not converge.

Instead one is left to rely on models that include some basic features of QCD while making simplifying assumptions in order to predict hadron properties. Fundamental quark models – constituent quark models, bag models, N_c models, and non-perturbative lattice QCD are among these – are difficult to relate directly to experimental results, since they include neither reaction mechanisms nor pions in the final state. For the calculation of observables accessible to experiment, more phenomenologically based models have been developed which can make predictions on the level of response functions.

1.2   Nucleon Deformation

The spatial distribution of the ground state wavefunction of the proton, *i.e.* its shape, is a property of fundamental interest. The possibility of nucleon deformation was initially raised by Glashow [1] a quarter of a century ago. In the modern view of the nucleon as a complex many-body system, one does not expect a spherically symmetric ground state. In a

2

naive constituent quark model, the nucleon is primarily an S-state wavefunction, but there is also expected to be some D-state admixture due to the tensor interaction between the quarks (analogous to the well known nucleon-nucleon and atomic hyperfine interactions) leading to a small, but nonzero, quadrupole deformation. Dynamical models of the nucleon explain the same quadrupole structure by pion cloud effects; this is due to the spontaneously broken chiral symmetry of QCD, in which the pion appears as an almost-Goldstone Boson interacting with the nucleon primarily in the P-wave state. In relativistic quark models such mixing of higher angular momentum states can be explained through relativistic invariance, without invoking tensor interactions [2].

Any static quadrupole moment of the $J = 1/2$ nucleon is experimentally inaccessible, due to spin-parity selection rules. Instead, we look for the signature of quadrupole admixture in the transition of the nucleon to its first excited state, the $\Delta(1232)$ resonance with $J = 3/2$. The $N \rightarrow \Delta$ transition takes place primarily via the Magnetic dipole (M1) interaction, which flips the spin of one of the quarks and so takes the $J^P = 1/2^+$ nucleon to the $J^P = 3/2^+$ Δ.

1.3   Resonance and Background

Because we experimentally detect only the decay products of the isospin $I = 3/2$, $I_3 = 1/2$ Δ resonance, we will see also background contributions from other reactions

$$\gamma^* + p \rightarrow \pi^+ + n \tag{1.1}$$

in which no delta resonance is produced. These correspond to $I = 1/2$ final states, will not obey the same spin-parity selection rules, as the restrictions imposed by the $J^P = 3/2^+$ intermediate state in the $I = 3/2$ channel do not apply. These background processes introduce non-resonant multipoles, greatly complicating the analysis.

Figure 1-1 diagrams all of the processes contributing to pion production. The first four in the sequence are the Born terms (a – d); the last of these is the Kroll – Ruderman

3

"contact" term [3]. The last two diagrams show the resonant $I = 3/2$ Δ channel (e), and a term representing higher resonances (f). The crossed graphs of (e) and (f) are not shown but also contribute.
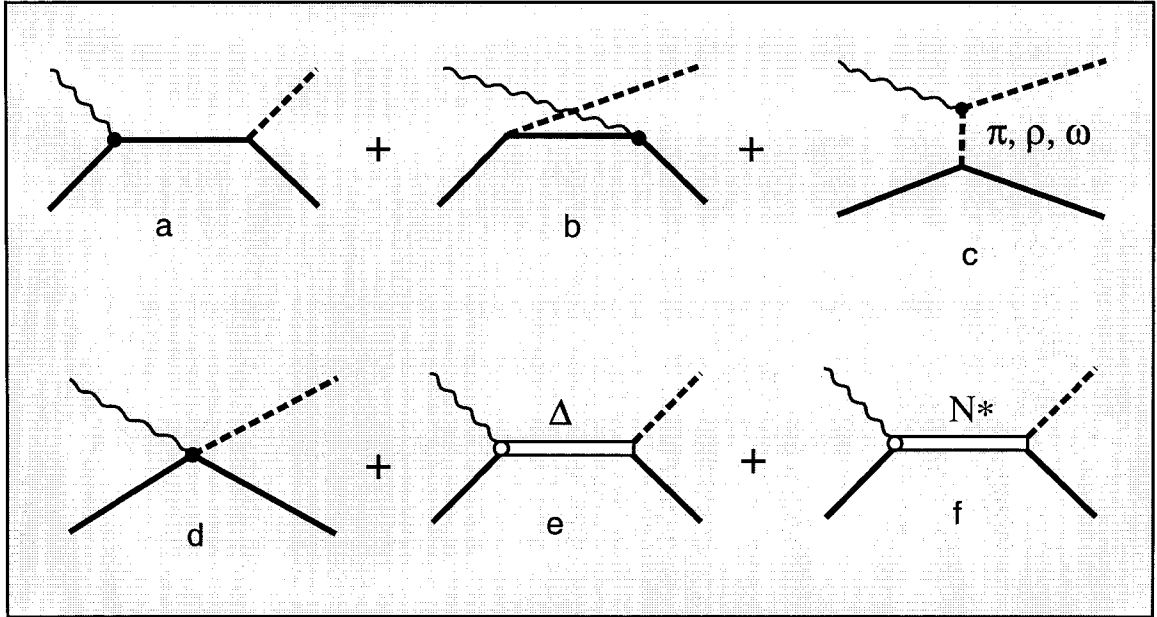
Figure 1-1: First order Feynman diagrams contributing to $\gamma * p \rightarrow \pi N$ cross section. Figures (a) through (d) are the Born Terms — the s-channel, u-channel, t-channel and contact terms, respectively. Figure (e) is the resonant Δ channel, and figure (f) represents higher resonances.

1.4   Previous Measurements

The quadrupole amplitudes of the $N \rightarrow \Delta$ transition have been the subject of vigorous recent study. These experiments can be divided into two categories, according to the means by which the excitation is induced: Photoproduction experiments absorb *real* photons on the nucleon, while in Electroproduction *virtual* photons are exchanged between the nucleon and an electron probe.

Photoproduction experiments offer the advantage of a greatly simplified model-independent analysis by limiting the multipole content of the cross section to combinations of transverse multipoles only. Recent measurements using real polarized tagged photons at Brookhaven [5] and Mainz [6] have yielded values for EMR of $(-3.0 \pm 0.3)\%$ and $(-2.5 \pm 0.3)\%$ re-

4

spectively, in good agreement both with one another and with the predictions of current pion production models [7], [8], [9]. Both the $\gamma p \to \pi^0 p$ and $\gamma p \to \pi^+ n$ charge channels were observed, allowing an isospin separation of the resonant $I = \frac{3}{2}$ channel. While the agreement between the two experiments is excellent with regard to the EMR ratio, it must be noted that there is significant deviation in the unpolarized cross sections, which is so far unresolved.

Exploring the Q^2 dependence of the EMR ratio, or measuring CMR at all, may only be done via electroproduction techniques. Because of the additional longitudinal multipoles in the electroproduction cross section, there are more observables which must be measured in order for a model independent analysis to be done. The experiment reported in this thesis is a part of the broader effort in the nuclear physics community to produce a database to allow such an analysis.

Numerous such studies have been carried out in recent years, involving all of the intermediate energy laboratories: Bates (See references [10],[11],[12], [13] and [14]), Mainz([15],[16]), and JLAB ([17],[18],[19] and [20]). To date, these efforts have focused primarily on the $\gamma^* p \to \pi^0 p$ reaction, with the exception of reference [20] which measures the polarized interference cross section $\sigma_{LT'}$ for Q^2 between 0.4 and 0.65 GeV^2. As a result, there is now a growing and rather extensive database available in the π^0 channel.

There has so far been a dearth of available data in the $p(e, e'\pi^+)n$ reaction channel, however. In the previous round of OOPS $N \to \Delta$ experiments at Bates, some π^+ data were taken, but these unfortunately have so far not been analyzed. More recently, fairly extensive π^+ data were taken with CLAS [21] at JLAB, in the Δ resonance region, but covering a higher Q^2 range than the present experiment [22]. Other than these, one must look back more than twenty years to find π^+ electroproduction data in the resonance region from only three experiments: the most recent dates from 1982 by Breuker [23], and two earlier reports from 1978 and 1974 by Breuker [24] and Evangelides [25], respectively. The existing data are thus insufficient for isospin decomposition and a model-independent analysis.

The present experiment is a step toward correcting this situation. By providing mea-

5

surements in the π^+ channel of all three separable unpolarized partial cross sections, in a critical low-Q^2 region corresponding to the maximum sensitivity to long-range pion cloud effects, we can provide important constraints on the fitting of background terms in the current round of model dependent analyses.

6

CHAPTER 2

Pion Electroproduction Formalism

The Δ resonance is very shortlived ($\tau \sim 5.5 \times 10^{-24}$s), decaying $> 99\%$ of the time into the nucleon ground state and a pion, which are the end products detected in coincidence with the scattered electron. The search for nucleon deformation via the $N \to \Delta$ thus falls within the broader study of pion electroproduction.

This chapter examines the spin-parity selection rules in detail, develops the formalism of pion electroproduction and defines the relationships between the multipole amplitudes and experimental observables.

2.1 Selection Rules

In addition to the dominant M1 amplitude, the spin-parity selection rules also allow transverse electric (E2) and Coulombic, (C2) quadrupole amplitudes to participate in the transition; the appearance of such quadrupole amplitudes is taken, in constituent quark models, as evidence of D-state deformation in the nucleon and/or Δ wave function.

The multipoles contributing to the resonant cross section are determined by the conservation of angular momentum and parity. The reaction of interest is

$$\gamma^* + p \to \Delta^+ \to \pi^+ + n \tag{2.1}$$

7

In the initial state is a photon with parity P and integer angular momentum L coupled to a proton with $J^P = 1/2^+$. The $J^P = 3/2^+$ delta resonance in the intermediate state limits the values of L and P that can be involved:

$$L^P \oplus \frac{1}{2}^+ = \frac{3}{2}^+ \qquad (2.2)$$

By inspection, any electromagnetic multipole with even parity and $L = 1$ or 2 is allowed. The electromagnetic multipoles (and their parities) are listed in Table 2.1. The multipoles are designated as Magnetic, Electric (transverse) and Coulomb (longitudinal) and labeled by the photon angular momentum L. Clearly, the multipoles of interest are M1, E2 and C2.

L	Long.	Trans.	Mag
0	C0 (+)	–	–
1	C1 (-)	E1(-)	M1(+)
2	C2 (+)	E2(+)	M2(-)
3	C3 (-)	E3(-)	M3(+)

Table 2.1: Electromagnetic Multipoles and their Parities

The Δ then decays into a pion ($J^P = 0^-$) and a ground state nucleon ($J^P = 1/2^+$), with orbital angular momentum l in the $\pi - N$ center of mass system, and overall parity $(-1)^{l+1}$ (due to the negative intrinsic parity of the pion). The requirement that

$$l^{(-)^l} \oplus \frac{1}{2}^+ \oplus 0^- = \frac{3}{2}^+ \qquad (2.3)$$

restricts the orbital angular momentum of the final state to $l = 1$.

In contrast to this, the spin-parity selection rules of the non-resonant background terms in the pion electroproduction cross section (see figure 1-1) are not constrained by the presence of an intermediate state. The background terms therefore contribute in all multipoles to the measured cross section. The estimation and subtraction of these background amplitudes from the experimental $N \rightarrow \Delta$ cross section remains a great technical challenge in the

8

investigation of hadron deformation. In principle, the background multipoles can be empirically fit once the world database of pion electroproduction measurements is sufficiently large. Until then, we are forced to rely on model-based calculations.

In the literature of pion electroproduction, it is common to label the interaction multipoles by the angular momenta of the final states. So the pion-production multipole associated with the magnetic dipole M1 is designated as M_{1+}; the subscript indicating that the orbital angular momentum $l = 1$, and that the spin of the neutron *adds* to it to give a total angular momentum of 3/2. The mapping of electromagnetic multipoles to n-π multipoles is:

$$M1 \rightarrow M_{1+}$$

$$E2 \rightarrow E_{1+}$$

$$C2 \rightarrow L_{1+}$$

Often the scalar multipoles $S_{l\pm}$ are used in place the longitudinal $L_{l\pm}$. The two are related by

$$S_{l\pm} = \frac{|\vec{q}^*|}{\omega^*} L_{l\pm} \tag{2.4}$$

The magnitudes of the quadrupole amplitudes are normally expressed in terms of their ratios compared to the dominant M1 amplitude. The Electric-to-Magnetic (EMR) and Coulomb-to-Magnetic (CMR) ratios are:

$$\text{EMR} = \frac{E2}{M1} = \frac{\Re(E_{1+}^* M_{1+})}{|M_{1+}|^2} \tag{2.5}$$

and

$$\text{CMR} = \frac{C2}{M1} = \frac{\Re(S_{1+}^* M_{1+})}{|M_{1+}|^2} \tag{2.6}$$

Since CMR is defined in terms of S_{1+}, the scalar multipole will generally be used instead of L_{1+} in this thesis.

9

2.2 Reaction Channels

In isospin space Δ^+ is described by the state $|I, I_3\rangle = |\frac{3}{2}, \frac{1}{2}\rangle$. The decomposition of this state into a multiplet of pion ($|I_\pi = 1, I_{\pi_3}\rangle$) and nucleon ($I_N = 1/2$) two-body states is given by the Clebsch – Gordon coefficients, which are derived by applying the step-down operator $\hat{I}_- = \hat{I}_{\pi_-} + \hat{I}_{N_-}$ to the maximally stretched $I = 3/2$ state, just as is done for composite angular momentum states:

$$\Delta^{++} = |\frac{3}{2}, \frac{3}{2}\rangle = |1, 1\rangle |\frac{1}{2}, \frac{1}{2}\rangle \tag{2.7}$$

In general, the result of operation on any state $|I, I_3\rangle$ with $\hat{I}_-$ is

$$\hat{I}_- |I, I_3\rangle = \sqrt{I(I+1) - I_3(I_3 - 1)} |I, I_3 - 1\rangle, \tag{2.8}$$

so operating on both sides of equation 2.7 gives, on the left,

$$\hat{I}_- |\frac{3}{2}, \frac{3}{2}\rangle = \sqrt{3} |\frac{3}{2}, \frac{1}{2}\rangle \tag{2.9}$$

which is equal to, on the right,

$$(\hat{I}_{\pi_-} + \hat{I}_{N_-}) |1, 1\rangle |\frac{1}{2}, \frac{1}{2}\rangle = \sqrt{2} |1, 0\rangle |\frac{1}{2}, \frac{1}{2}\rangle + |1, 1\rangle |\frac{1}{2}, -\frac{1}{2}\rangle \tag{2.10}$$

Therefore

$$|\frac{3}{2}, \frac{1}{2}\rangle = \sqrt{\frac{2}{3}} |1, 0\rangle |\frac{1}{2}, \frac{1}{2}\rangle + \sqrt{\frac{1}{3}} |1, 1\rangle |\frac{1}{2}, -\frac{1}{2}\rangle \tag{2.11}$$

where the first term represents a $\pi^0 + p$ final state, while the second is $\pi^+ + n$. From the amplitudes we see that there is a 2:1 branching ratio for the two decay channels.

2.2.1 Isospin Amplitudes

In the initial state the target proton has $I = \frac{1}{2}$, $I_3 = +\frac{1}{2}$, and couples to an electromagnetic current with isospin structure $\sim \frac{1}{2}(f^s + f^v \tau_0)$, which contains both an isoscalar and an

isovector component [26]. In the final state, the pion is an isovector particle (ϕ). Assuming the hadronic system conserves isospin, the interaction in isospin-space has to be proportional to $\tau \cdot \phi$. Arranging the Pauli matrices that appear in the interaction into a symmetrical form, the overall matrix element may be written as

$$A = \frac{1}{2} A^{(-)} [\tau_\alpha, \tau_0] + A^{(+)} \delta_{\alpha 0} + A^{(0)} \tau_\alpha .$$ (2.12)

The first two terms here are the commutator and anticommutator of τ_α with the isovector electromagnetic current, and the last term corresponds to the isoscalar current. The amplitudes for the two reaction channels available for a proton target can be written in terms of the three isospin amplitudes:

$$A(\gamma p \rightarrow n\pi^+) = \sqrt{2}(A^{(-)} + A^{(0)})$$ (2.13)

$$A(\gamma p \rightarrow p\pi^0) = (A^{(+)} + A^{(0)})$$ (2.14)

In order to analyze the resonances of the πN system in terms of I, the three amplitudes of equation 2.12 can be combined as

$$
\begin{aligned}
A^{3/2} &= A^{(+)} - A^{(-)} \\
A_p^{1/2} &= A^0 + \frac{1}{3} A^{(+)} + \frac{2}{3} A^{(-)} \\
A_n^{1/2} &= A^0 - \frac{1}{3} A^{(+)} - \frac{2}{3} A^{(-)}
\end{aligned}
$$ (2.15)

where $A^{3/2}$ gives the resonant amplitude, and $A_p^{1/2}$ and $A_n^{1/2}$ give the non-resonant amplitudes associated with scattering from proton and neutron targets, respectively. For this experiment we ignore $A_n^{1/2}$, and the amplitudes for the charge channels of interest can be

11

written as

$$A(\gamma p \to n\pi^+) = \sqrt{2}\left(A_p^{1/2} - \frac{1}{3}A^{(3/2)}\right) \tag{2.16}$$

$$A(\gamma p \to p\pi^0) = A_p^{1/2} + \frac{2}{3}A^{(3/2)} \tag{2.17}$$

It appears that the resonant $I = \frac{3}{2}$ amplitude is reduced in magnitude, relative to the non-resonant part $A^{(0)} + \frac{1}{3}A^{(1/2)} \equiv A_p^{1/2}$, by a factor of two in the $\pi^+ n$ channel compared to the $\pi^0 p$. It is clear that measurements in the $\pi^+ n$ channel are much more sensitive to the background terms, and so afford an opportunity to check the assumptions made by the pion production models about the strengths of these non-resonant interactions. For a full isospin decomposition, measurements of a neutron target will also be necessary in order to isolate $A_n^{1/2}$ as well.

2.3 Coincidence Electron Scattering

2.3.1 Laboratory Frame Kinematics

Particle	4-Vector
Incident Electron	$k_i = (\varepsilon_i, \vec{k}_i)$
Scattered Electron	$k_f = (\varepsilon_f, \vec{k}_f)$
Target Nucleus	$p_i = (E_i, \vec{p}_i)$
Virtual Photon	$q = (\omega, \vec{q})$
Intermediate State	$W^\mu = (W_0, \vec{q})$
Detected Pion	$p_\pi = (E_\pi, \vec{p}_\pi)$
Undetected Neutron	$p_n = (E_n, \vec{p}_n)$

Table 2.2: Four-vectors in the kinematic analysis of the $p(e, e'\pi^+)n$ reaction

The kinematics of the inclusive pion electroproduction reaction $p(e, e'\pi^+)n$ are diagrammed in figure 2-1. Table 2.3.1 defines the four-vectors involved. Figure 2-2 defines the coordinate system used in the laboratory frame to describe out-of-plane kinematics.

The scattering plane is defined by the momentum vectors of the incoming $(\vec{k}_i)$ and

12
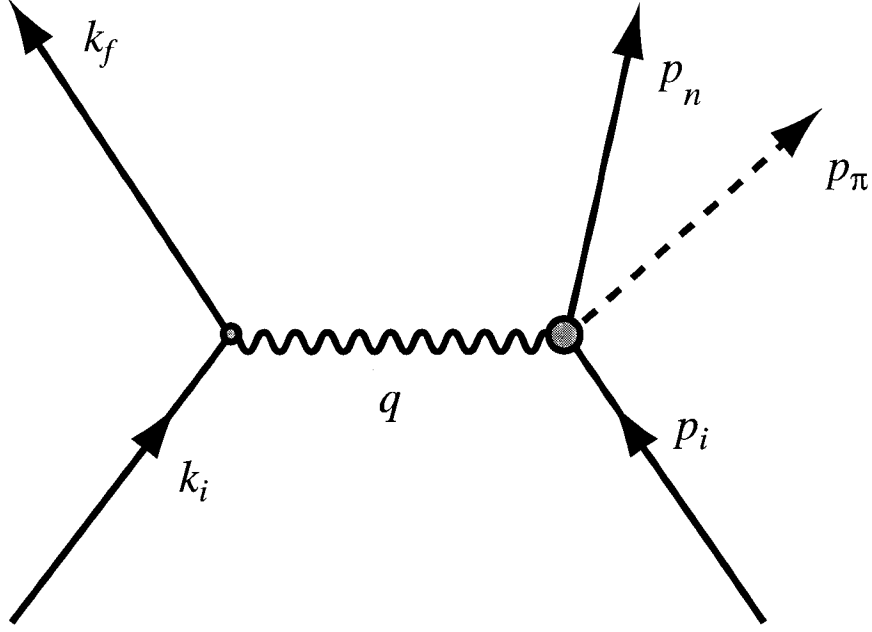
Figure 2-1: Kinematic analysis of pion electroproduction in the one photon exchange approximation

outgoing ($\vec{k}_f$) electrons. The angle between them is the electron scattering angle θ_e. The momentum transfer $\vec{q}$ and detected pion momentum $\vec{p}_\pi$ similarly define the reaction plane. The azimuthal angle $\phi_{\pi q}$ describes the rotation between the two planes, and $\theta_{\pi q}$ gives the polar angle of the pion emission relative to the momentum transfer vector.

At the electron vertex, the initial electron four-vector k_i is known, and the final electron momentum $\vec{k}_f$ measured in the experiment. The four-momentum transfer is

$$q = k_i - k_f = (\omega, \vec{q}),$$ (2.18)

with $\omega = \varepsilon_i - \varepsilon_f$ and $\vec{q} = \vec{k}_i - \vec{k}_f$. The square of the four-momentum transfer is

$$q^2 = \omega^2 - |\vec{q}|^2,$$ (2.19)

Since $q^2 \leq 0$, it is common to define the positive quantity

$$Q^2 = -q^2 \geq 0.$$ (2.20)

13
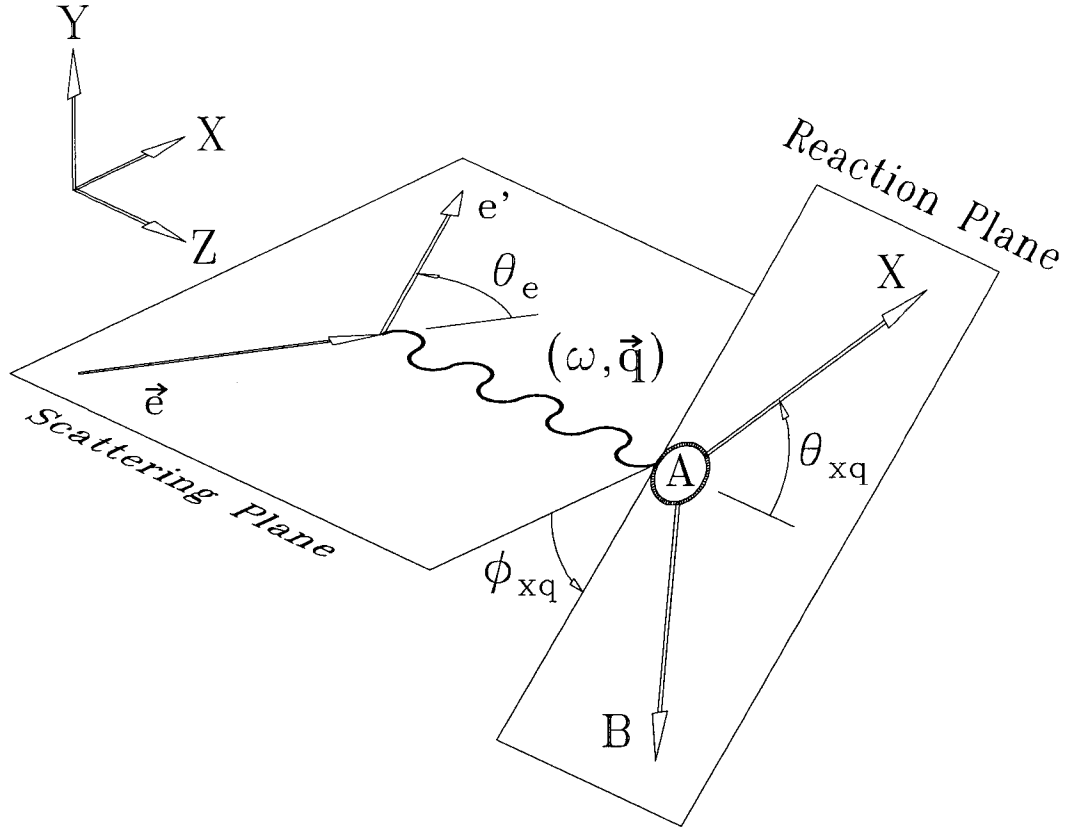
Figure 2-2: Kinematic diagram for the general coincidence reaction A(e, e' x)B with out-of-plane detection.

In the Extreme Relativistic Limit (ERL), $\varepsilon_i \Longrightarrow |\vec{k}_i|$, and Q^2 takes on a simple form:

$$Q^2 \approx 4\varepsilon_i \varepsilon_f \sin^2 \frac{\theta_e}{2} \qquad (2.21)$$

At the energies involved in this experiment, this approximation is accurate to about one part in 20,000.

At the hadronic vertex, the kinematics are fully determined by the detection of the pion momentum, since in the laboratory frame the initial target proton is at rest: $p_i = (m_p, 0)$. The undetected neutron four-momentum is given by:

$$p_n = p_i + q - p_\pi \qquad (2.22)$$

14

The energy component of the undetected vector is called the *missing energy*,

$$E_{\text{miss}} = m_p + \omega - E_\pi \,, \tag{2.23}$$

and the momentum 3-vector the *missing momentum*

$$\vec{p}_{\text{miss}} = \vec{q} - \vec{p}_\pi \,. \tag{2.24}$$

The invariant amplitude is the *missing mass*:

$$M_{\text{miss}} = \sqrt{E_{\text{miss}}^2 - \vec{p}_{\text{miss}}^2} \,, \tag{2.25}$$

For this experiment, $M_{\text{miss}} = m_n = 939.56536 \pm 0.00008$ MeV [27]. The missing mass is a useful quantity for selecting true, coincident $p(e, e'\pi^+)n$ events from accidental backgrounds.

Since four of the five momenta are measured or prepared in the experiment, there remain only three independent scalars involved in the kinematics. Following Raskin and Donnelly [28], we choose Q^2, the pion emission polar angle in the center of mass frame $\theta_{\pi q}^*$, and the center of mass energy or invariant mass W, defined by

$$W^2 = (p_i + q)^2 = m_p^2 + 2m_p\omega - Q^2 \,. \tag{2.26}$$

For the Δ resonance, the invariant mass is $W = 1232$ MeV/c^2. The sum of the target and virtual photon four-vectors appearing here, $(p_i + q)$, is the *intermediate state* four-vector, describing the excited nucleon state which is not directly detected. In the laboratory frame it is given by

$$p_i + q = (m_p + \omega, \vec{q}) \equiv (W_0, \vec{q}) \tag{2.27}$$

2.3.2   The Center of Mass System

The Center of Mass (CM) system is defined as the reference frame in which the excited nucleon is at rest, which moves with some speed β relative to the laboratory along the

direction of the q-vector, which we take to define the z-axis.

The Lorentz transformation between the two frames is defined by β and the relativistic factor $\gamma = 1/\sqrt{1-\beta^2}$. Since we know the lab energy and momentum of the intermediate state and its invariant mass, the transformation parameters can be easily identified from the basic relativistic energy and momentum relationships. The result is

$$\gamma = \frac{W_0}{W} \tag{2.28}$$

$$\beta = \frac{|\vec{q}|}{W_0} \tag{2.29}$$

The CM energies and momenta of the final state hadrons are completely determined. Energy and momentum conservation require that

$$E_n^* + E_{\pi+}^* = W \tag{2.30}$$

and

$$\vec{p}^*_{\pi+} = -\vec{p}^*_{n} \tag{2.31}$$

where the asterisks flag quantities that are explicitly to be evaluated in the CM frame. By squaring both sides and using the Einstein identity

$$E^2 = p^2 + m^2, \tag{2.32}$$

equation (2.31) can be rewritten as

$$E_n^{*\,2} - m_n^2 = E_{\pi+}^{*\,2} - m_{\pi+}^2 \tag{2.33}$$

Combining equations (2.33) and (2.30) and solving for the pion energy in the CM frame yields

$$E^*_{\pi+} = \frac{W^2 - m_n^2 + m_{\pi+}^2}{2W} \tag{2.34}$$

16

The neutron CM energy is similarly

$$E^*{}_n = \frac{W^2 + m_n^2 - m_{\pi^+}^2}{2W}$$

(2.35)

The CM momenta then follow directly from (2.32).

2.4 Coincidence Cross Section

The coincidence cross section for pion electroproduction is five-fold differential in the electron and pion solid angles and the energy transfer, ω. The hadron vertex is traditionally calculated in the CM frame. Following Drechsel and Tiator [7] we write:

$$\frac{d\sigma}{d\Omega_e \, d\Omega_\pi^* \, d\omega} = \Gamma \frac{d\sigma}{d\Omega_\pi^*} \, .$$

(2.36)

Γ is the virtual photon flux, which is completely determined by the kinematics at the electron vertex:

$$\Gamma = \frac{\alpha}{2\pi^2} \frac{E_f}{E_i} \frac{k_\gamma}{Q^2} \frac{1}{1 - \varepsilon}$$

(2.37)

where ε_i and ε_f are the initial and final electron energies and k_γ is the so-called photon equivalent energy

$$k_\gamma = \frac{W^2 - m_p^2}{2m_p},$$

(2.38)

which is the energy that would be required by a real photon to excite the target proton to CM energy W.

The transverse polarization ε of the virtual photon is given by

$$\varepsilon = \{1 + 2\vec{q}^{\,2}/Q^2 \tan^2(\theta_e/2)\}^{-1} \, .$$

(2.39)

The remaining two-fold differential cross section contains the details of the hadron vertex, and in the absence of beam, target or final state polarization it is separable into four independent response functions, labeled according to the polarization components of the vir-

17

tual photon as the longitudinal (L), transverse (T), and interference (LT and TT) response functions:

$$\frac{\mathrm{d}\sigma}{\mathrm{d}\Omega_\pi^*} = \frac{|\vec{q}^{\,*}|}{k_\gamma^*}\left\{R_T + \varepsilon_L R_L + \varepsilon R_{TT}\cos 2\phi + \sqrt{2\varepsilon_L(1+\varepsilon)}\,R_{LT}\cos\phi\right\} \qquad (2.40)$$

where $k_\gamma^* \equiv k_\gamma\frac{m_p}{W}$ is the photon equivalent energy in the center of mass[1], and $\varepsilon_L = \frac{Q^2}{(\omega^*)^2}\varepsilon$ is the longitudinal polarization of the virtual photon. The use of ε_L is inconvenient for comparison with the MAID and DMT models, which do not use it, so the cross section is re-written to eliminate it as

$$\frac{\mathrm{d}\sigma}{\mathrm{d}\Omega_\pi^*} = \frac{|\vec{q}^{\,*}|}{k_\gamma^*}\left\{R_T + \varepsilon\frac{Q^2}{(\omega^*)^2}R_L + \varepsilon R_{TT}\cos 2\phi + \sqrt{2\varepsilon(1+\varepsilon)}\,\frac{Q}{\omega^*}R_{LT}\cos\phi\right\}, \qquad (2.41)$$

The results of the MAID and DMT calculations are expressed in terms of partial cross sections:

$$\frac{\mathrm{d}\sigma}{\mathrm{d}\Omega_\pi^*} = \frac{\mathrm{d}\sigma_T}{\mathrm{d}\Omega_\pi^*} + \varepsilon\frac{\mathrm{d}\sigma_L}{\mathrm{d}\Omega_\pi^*} + \varepsilon\frac{\mathrm{d}\sigma_{TT}}{\mathrm{d}\Omega_\pi^*}\cos 2\phi + \sqrt{2\varepsilon(1+\varepsilon)}\,\frac{\mathrm{d}\sigma_{LT}}{\mathrm{d}\Omega_\pi^*}\cos\phi \qquad (2.42)$$

By direct comparison of equations 2.41 and 2.42, the relationships between the partial cross sections and the response functions are:

$$\frac{\mathrm{d}\sigma_T}{\mathrm{d}\Omega_\pi^*} = \frac{|\vec{q}^{\,*}|}{k_\gamma^*}R_T \qquad (2.43)$$

$$\frac{\mathrm{d}\sigma_L}{\mathrm{d}\Omega_\pi^*} = \frac{|\vec{q}^{\,*}|}{k_\gamma^*}\frac{Q^2}{(\omega^*)^2}R_L \qquad (2.44)$$

$$\frac{\mathrm{d}\sigma_{TT}}{\mathrm{d}\Omega_\pi^*} = \frac{|\vec{q}^{\,*}|}{k_\gamma^*}R_{TT} \qquad (2.45)$$

$$\frac{\mathrm{d}\sigma_{LT}}{\mathrm{d}\Omega_\pi^*} = \frac{|\vec{q}^{\,*}|}{k_\gamma^*}\frac{Q}{\omega^*}R_{LT} \qquad (2.46)$$

---

[1]Note that the "center of mass" frame with regard to this quantity is the hypothetical center of mass system of the target and a real photon, not the true CM of the experiment in which all other starred quantities are evaluated. The photon equivalent energy in the true CM frame would be

$$k_\gamma^* = k_\gamma\frac{m_p + \omega - |\vec{q}|}{W}$$

As a shorthand for both the full and the partial two-fold differential cross sections, we will frequently use the notation

$$\sigma \equiv \frac{d\sigma}{d\Omega_\pi^*} \tag{2.47}$$

This creates no possible source of confusion, as in the context of this thesis the total cross section is never used.

Because the partial cross sections σ_T and σ_L are both ϕ-independent, they can not be individually isolated except by performing a Rosenbluth separation, which was not done during this experiment. Instead we combine them and define the partial cross section

$$\sigma_0 \equiv \sigma_T + \varepsilon \sigma_L \tag{2.48}$$

The full hadronic cross section is then a sum of three independent terms in ϕ. By measuring the cross section at a minimum of three different $\phi_{\pi q}$ angles, it is possible to separate the partial cross sections σ_{TT}, σ_{LT} and $\sigma_0 \equiv \sigma_T + \varepsilon \sigma_L$.

2.5 Multipole Expansion

The electromagnetic multipoles of interest are not directly observable, but appear in combination with one another, and with non-resonant multipoles due to background processes, in the pion production partial cross sections.

The five response functions may be expanded in terms of the pion production multipoles. This is explicitly worked out in references [28] and [7]. It is convenient for the present analysis to re-write the results of [7] in terms of partial cross sections instead of response functions, and to convert the longitudinal multipoles $L_{l\pm}$ to scalar multipoles $S_{l\pm}$ according to equation 2.4. Keeping only terms to first order in the S- and P-wave ($\ell \leq 1$) multipoles

19

$(E_{l\pm}/M_{1+})$ or $(S_{l\pm}/M_{1+})$, we have:

$$\sigma_T = \frac{|\vec{q}\,|^*}{k_\gamma^*}\left\{ |E_{0+}|^2 + \frac{1}{2}|2M_{1+} + M_{1-}|^2 + \frac{1}{2}|3E_{1+} - M_{1+} + M_{1-}|^2 \right.$$
$$- 2\cos\theta_{\pi q}^* \Re\{E_{0+}^*(M_{1+} - M_{1-} + 3E_{1+})\}$$
$$+ \cos^2\theta_{\pi q}^* \left\{ |3E_{1+} + M_{1+} - M_{1-}|^2 - \frac{1}{2}|2M_{1+} + M_{1-}|^2 \right.$$
$$\left. \left. - \frac{1}{2}|3E_{1+} - M_{1+} + M_{1-}|^2 \right\} \right\}$$

(2.49)

$$\sigma_L = \frac{Q^2}{k_\gamma^*|\vec{q}\,|^*}\left\{ |S_{0+}|^2 + 4|S_{1+}|^2 + |S_{1-}|^2 - 4\Re\left\{S_{1+}^*S_{1-}\right\} \right.$$
$$\left. - 2\cos\theta_{\pi q}^* \Re\{S_{0+}^*(S_{1-} + 4S_{1+})\} + 12\cos^2\theta_{\pi q}^* \left[|S_{1+}|^2 + \Re\left\{S_{1+}^*S_{1-}\right\} \right] \right\}$$

(2.50)

$$\sigma_{TT} = 3\sin^2\theta_{\pi q}^* \frac{|\vec{q}\,|^*}{k_\gamma^*}\left[\frac{3}{2}|E_{1+}|^2 - \frac{1}{2}|M_{1+}|^2 \right.$$
$$\left. - \Re\left\{E_{1+}^*(M_{1+} - M_{1-}) + M_{1+}^*M_{1-}\right\} \right]$$

(2.51)

$$\sigma_{LT} = -\sin\theta_{\pi q}^* \frac{Q}{k_\gamma^*}\Re\left\{ S_{0+}^*\left[M_{1-} - M_{1+} + 3E_{1+}\right] - \left[2S_{1+}^* - S_{1-}^*\right]E_{0+} \right.$$
$$\left. - 6\cos\theta_{\pi q}^* \left[S_{1+}^*(M_{1-} - M_{1+} + E_{1+}) + S_{1-}^*E_{1+}\right] \right\}$$

(2.52)

20

CHAPTER 3

Experimental Setup

3.1 Overview

The experiment was part of a larger set of experiments, carried out in the South Hall at the MIT-Bates Linear Accelerator Center during 2000 and 2001 using the Out Of Plane Spectrometer (OOPS) system, which were explicitly designed to isolate response functions in $(e, e'x)$ reactions by exploiting the different dependencies on the azimuthal pion angle ϕ_{xq} in the scattering cross section (see figure 2-2). In addition to the $p(e, e'\pi^+)n$ measurements described here, data were also taken in the π^0 channel of the $N \rightarrow \Delta$ reaction [29] as well as on Virtual Compton Scattering [30] [31]. The π^+ data were taken over the course of eleven days, beginning on April 4, 2001.

An unpolarized 950 MeV electron beam was directed onto the liquid hydrogen target, the MIT Basel Loop, a detailed description of which may be found in reference [32]. The scattered electrons were detected using the One-Hundred Inch Proton Spectrometer (OHIPS), and three OOPS modules were used for pion detection. Two OOPS modules were mounted vertically above and below one another on a movable gantry for measuring the out-of-plane cross sections, while the third was mounted on a satellite platform for in-plane measurements.

21
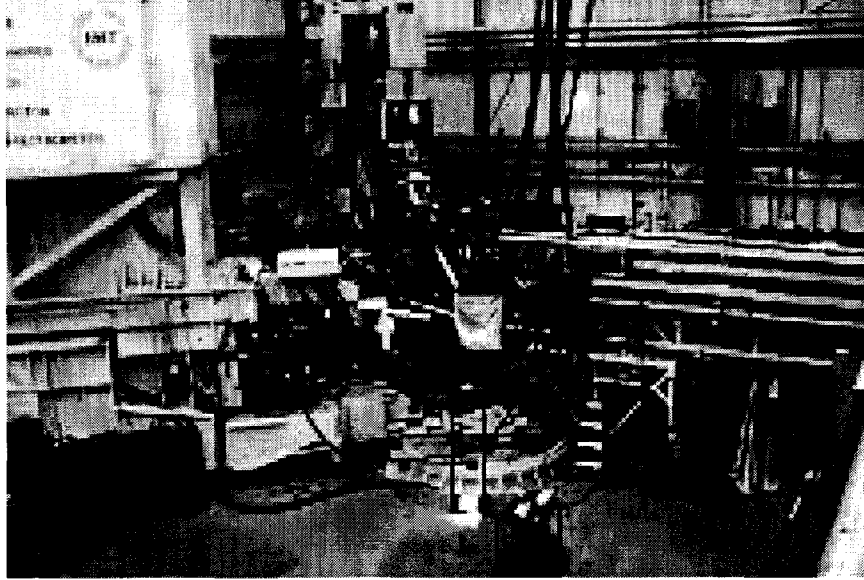
Figure 3-1: The OOPS system in a typical arrangement for data taking in the South Experimental Hall. OHIPS is seen in profile on the left. In the center of the photo all four OOPS modules are arranged in a cluster facing the target, which is covered here with a tarp. the picture. The leftmost module seen here, OOPS D, was not used in this experiment.

Data were taken in two consecutive setups, each using all three OOPS modules to make simultaneous measurements at different $\phi_{\pi q}$ angles about the q-vector. These are shown schematically in figure 3-2. One OOPS spectrometer (OOPS A) was positioned in-plane at $\phi_{\pi q} = 180°$ and CMS polar angle $\theta^*_{\pi q} = 44.45°$ in both setups to provide a consistency check between the two setups.

In the first setup ("Kinematics a"), the remaining two OOPS modules were positioned below and above the scattering plane at $\phi_{\pi q} = -60°$ and $\phi_{\pi q} = +60°$, both on the $\theta^*_{\pi q} = 44.45°$ cone (OOPS B and C,respectively). Because the ϕ-dependences in the (unpolarized) cross section go as the cosines of ϕ and 2ϕ, the cross section is a function only of $|\phi|$, and OOPS B and C make redundant measurements, doubling the statistics at $|\phi| = 60°$.

22
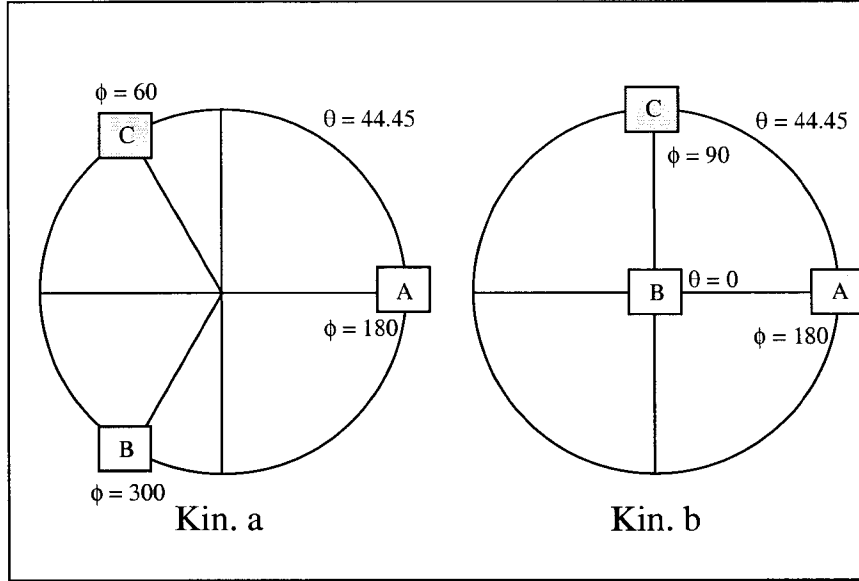
Figure 3-2: OOPS spectrometer positions in the two π^+ kinematic settings. The circle shows the projection of the cone $\theta*_{\pi q} = 44.45°$, with the q-vector pointing into the page at the center.

In the second setup ("Kinematics b") OOPS C is placed above the scattering plane at $\phi_{\pi q} = 90°$, providing the third measurement required to separate the response functions on the $\theta^*_{\pi q} = 44.45°$ cone. OOPS B is placed in-plane directly on the q-vector ($\theta^*_{\pi q} = 0°$) to measure the so-called "parallel cross section".

The relevant kinematic parameters for both settings are shown in tables 3.1 and 3.2. In both settings the cross section is measured on the Δ resonance at $W = 1232$ MeV, at a four-momentum transfer of $Q^2 = 0.127$ GeV^2/c^2 where the contributions to the quadrupole amplitudes due to pion cloud effects are predicted to be maximal.

23
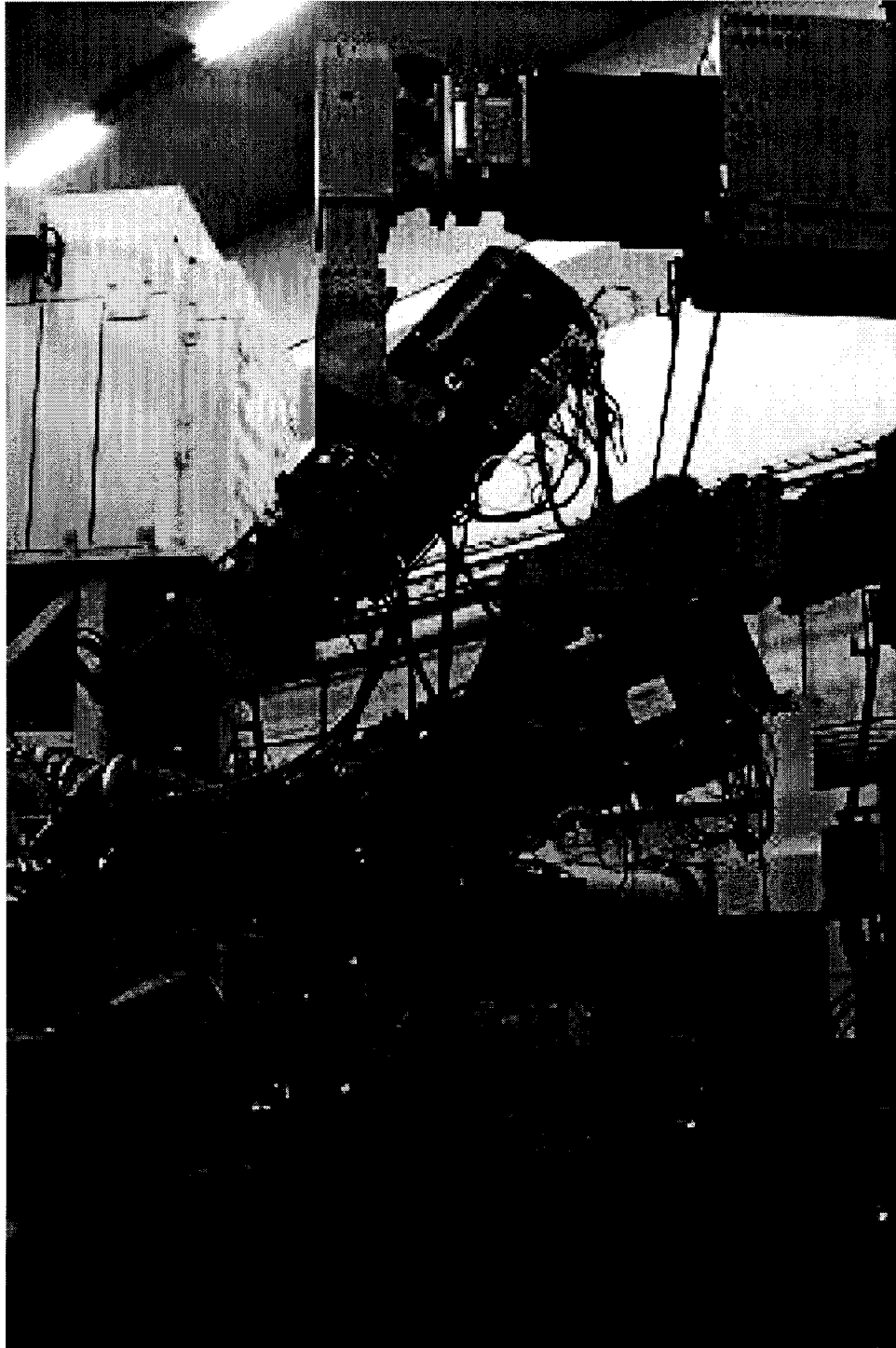
Figure 3-3: OOPS modules B and C mounted on the gantry in the South Hall. OHIPS can be seen in the background on the left hand side of the picture

24

Beam Energy	E	950.0 MeV
Beam Current	I [μA]	5 – 7
Scattered Electron Momentum	p'_e [MeV/c]	542.62
Electron Scattering Angle	θ_e [deg.]	28.74
Virtual Photon Angle	θ_q [deg.]	-28.82
Energy Transfer	ω [MeV]	407.38
Momentum Transfer	$|\vec{q}|$ [MeV/c]	541.26
Invariant Mass	W [MeV]	1232.0
4-Momentum Transfer	Q^2 [GeV^2/c^2]	0.127
Virtual Photon Flux	Γ [μb/MeV/sr]	2.43×10^{-6}
Virtual photon polarization	ε	0.7676

Table 3.1: Experimental Design Parameters I: Lepton Vertex Kinematics

Kinematics a		OOPS A	OOPS B	OOPS C
Pion Momentum	p_π [MeV/c]	332.92	332.92	332.92
Pion polar angle	$\theta_{\pi q}$ [deg.]	28.38	28.38	28.38
Pion CMS polar angle	$\theta^*_{\pi q}$ [deg.]	44.45	44.45	44.45
Pion azimuthal angle	$\phi_{\pi q}$ [deg.]	180	300	60
OOPS floor angle	α [deg.]	-57.20	-13.70	-13.70
OOPS elevation angle	β [deg.]	0.00	-24.31	24.31
Solid angle Jacobian	J	2.188	2.188	2.188

Kinematics b		OOPS A	OOPS B	OOPS C
Pion Momentum	p_π [MeV/c]	332.92	363.56	332.92
Pion polar angle	$\theta_{\pi q}$ [deg.]	28.38	0.00	28.38
Pion CMS polar angle	$\theta^*_{\pi q}$ [deg.]	44.45	0.00	44.45
Pion azimuthal angle	$\phi_{\pi q}$ [deg.]	180	–	90
OOPS floor angle	α [deg.]	-57.20	-28.82	-28.82
OOPS elevation angle	β [deg.]	0.00	0.00	28.39
Solid angle Jacobian	J	2.188	2.588	2.188

Table 3.2: Experimental Parameters II: Hadron Vertex Kinematics and OOPS Spectrometer Settings

25

The partial cross sections are given in terms of the measured cross sections at $|\phi_{\pi q}| = 180°$, $60°$ and $90°$ by:

$$\sigma_0 = \frac{\sigma(180°) + 2\sigma(60°)}{3} \tag{3.1}$$

$$\sigma_{TT} = \frac{\sigma(180°) + 2\sigma(60°) - 3\sigma(90°)}{3\varepsilon} \tag{3.2}$$

$$\sigma_{LT} = \frac{4\sigma(60°) - 3\sigma(90°) - \sigma(180°)}{3\sqrt{\varepsilon(1+\varepsilon)}} \tag{3.3}$$

for $\theta_{\pi q}^* = 44.45°$. In addition, the "parallel cross section" provides a second measurement of the response function σ_0 at $\theta_{\pi q}^* = 0°$, where σ_{LT} and σ_{TT} both go identically to zero .

26

3.2   Accelerator and Beamline

The layout of the MIT-Bates Linear Accelerator Center is shown if figure 3-4. The injector room containing the thermionic source is located at the top of the figure, at the west end of the facility. From here pulsed beams of electrons, with average currents up to 50 μA, are accelerated over a distance of 160 meters to a maximum energy of 500 MeV. A recirculator loop returns the beam to the beginning of the accelerator section where it is re-accelerated, doubling the maximum energy to 1 GeV.

After the acceleration section the beam passes through the Energy Compression System which consists of four dipole magnets, an energy-defining slit, and an RF cavity which together control the beam energy spread.

The beam is then diverted to either the North or South Experimental Halls. In the South Hall, the South Hall Ring (SHR) has been constructed to provide increased duty factors for use in coincidence experiments. The SHR can operate in beam storage mode, for use in internal gas targets with the BLAST detector, as well as pulse-stretching mode with resonant extraction of quasi-CW beam to the OOPS beamline for use with the MIT external Basel Loop Target.

For this experiment pulsed beam was injected into the SHR operating in stretching mode, and extracted to the OOPS beamline at a 580 Hz repetition rate. The central beam energy was 950 MeV $\pm$0.3%, with a beam energy spread of $\pm$0.3%. The average duty factor was $\sim$ 50%, with typical average currents of 7 μA in the experimental gate. A typical extraction profile is shown in figure 3-5.

27
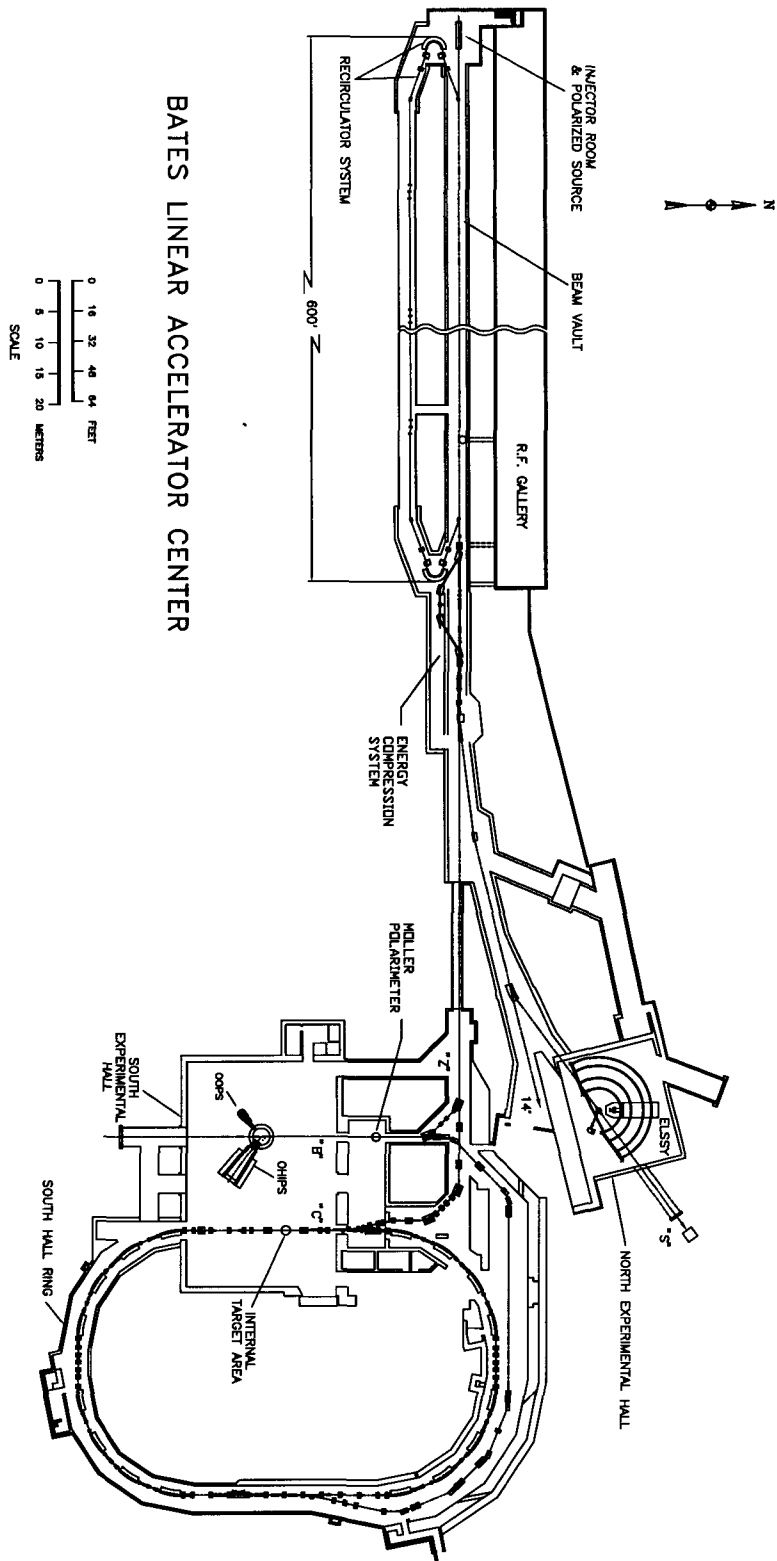
Figure 3-4: Schematic view of the MIT-Bates Linear Accelerator Center

28
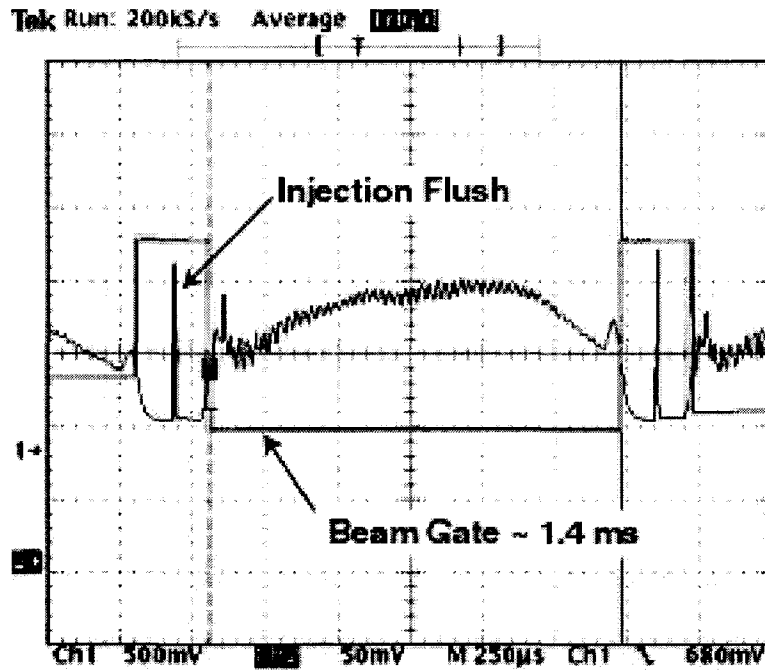
Figure 3-5: Extracted Beam Profile

3.2.1 Beam Charge Instrumentation

Standard Instrumentation

The basic beam charge measurement instrumentation is shown schematically in figure 3-6. Beam charge collected at the Faraday cup during production is separated into two parts by a gate box. During data production runs, the gate box is triggered on the 580 Hz beam spill pulse. The gated current represents the stable portion of the each beam spill that is used for the experiment. The ungated portion includes the interval between beam spills; during this time, the front-end veto shuts down data collection.

The gated and ungated portions of the current are directed to separate Brookhaven Instruments Corporation current integrators, hereafter called BIC 1 and BIC 2. Each integrator sums the charge fed into it onto 10-second increments, and the charges for each of the increments are stored in scalers in the data acquisition system. The two scaler channels are labeled as Faraday Cup Gated (FCG) and Faraday Cup Ungated (FCU), respectively. The FCU channel is not used in the analysis.

29
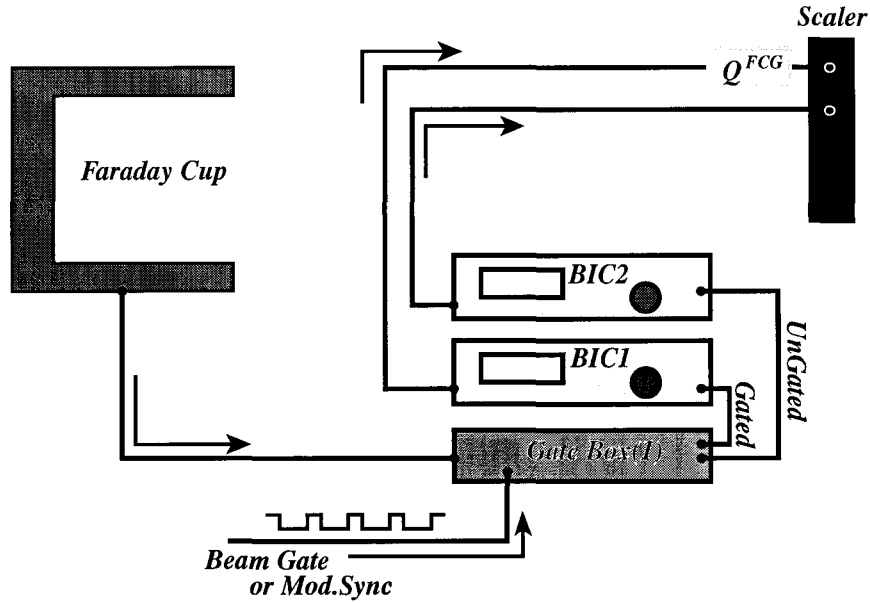
Figure 3-6: The standard OOPS charge measurement instrumentation system

In addition to the true beam current, there are pedestal currents introduced by the instruments themselves which complicate the beam charge measurement.

The Faraday cup was found to draw a current on the order of 1μA, possibly due to some internal contact potential. This is referred to as the "galvanic current", I_{gv}, and it is summed with the beam current at the Faraday cup. The measurement and subtraction of this galvanic current was a critical component in the accurate determination of the beam charge.

Each of the BIC integrators also has its own adjustable pedestal current, which is added to the output of the device to the data acquisition. The BIC 1 pedestal current was set to $I_{BIC1} = 0.1533 \pm 0.0039$ μA for the first portion of data collection, which corresponded to all of kinematics b and roughly the first third of kinematics a. For the remainder of kinematics a, the BIC 1 pedestal current was set to $I_{BIC1} = -0.083 \pm 0.042$ μA. The determination of the BIC pedestal currents is described in detail in Appendix A.

The total of the output of BIC1 to the FCG scaler channel for a given run includes the BIC pedestal current I_{BIC1} summed over the entire 10 second interval, plus the sum of the

30

combined beam current, I_{beam}, and I_{gv} over the number of beam gates:

$$Q_{FCG} = (I_{beam} + I_{gv}) \times \#BG \times \Delta T + I_{BIC1} \times T_{run} \qquad (3.4)$$

where $\#BG$ is the number of beam gates, ΔT is the beam gate width, typically about 1.4 ms, and T_{run} is the total run time. This is shown schematically in figure 3-7.
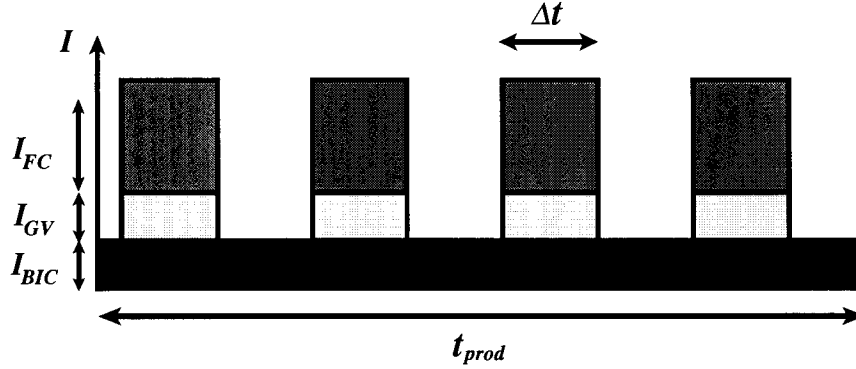
Figure 3-7: Schematic representation of the charge measured by the FCG scaler channel during data production runs.

The true beam charge is therefore given by

$$Q_{beam} = Q_{FCG} - Q_{ped}, \qquad (3.5)$$

where the pedestal charge is

$$Q_{ped} = I_{gv} \times \#BG \times \Delta T - I_{BIC1} \times T_{run} \qquad (3.6)$$

Modified Instrumentation

In order to separate the beam and pedestal currents, an additional gate box and current integrator were added to the beam charge measurement system, as was a visual read-out Hewlett Packard Current Monitor. The modified configuration is shown in figure 3-8.

31
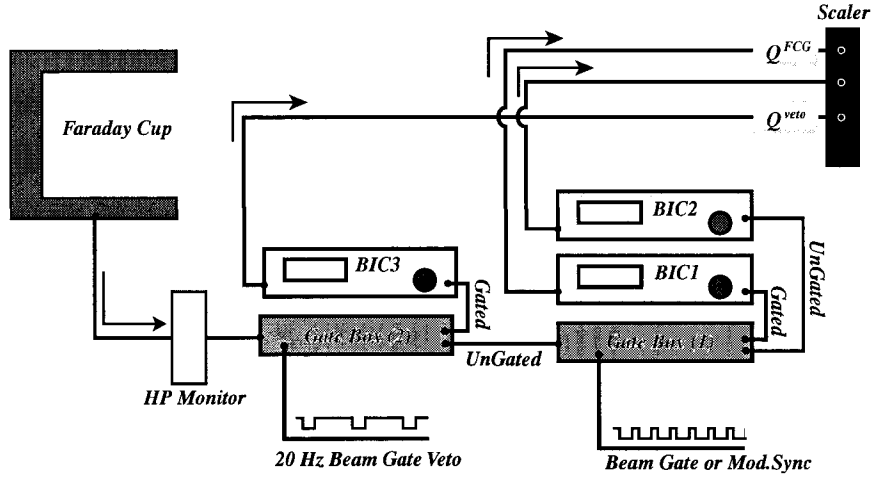
Figure 3-8: The modified beam charge instrumentation system includes a Hewlett-Packard current monitor and additional gate box and current integrator to measure pedestal currents.

The additional gate box was installed between the Faraday cup and the original gate box in order to measure the galvanic current. Because the accelerator uses only 580 of its maximum of 600 beam cycles per second, a second gate was set up to sample the Faraday Cup output during the 20 remaining cycles when no beam is present. The current within this gate was sent to a third BIC integrator (BIC 3), and the integrated charge was stored in a separate scaler Chanel in the data stream, the 20 Hz veto scaler. During a production run, this charge is given by

$$Q_{\text{veto}} = (I_{\text{gv}} \times \text{DF}_{\text{veto}} + I_{\text{BIC3}}) \times T_{\text{run}}, \tag{3.7}$$

where we have introduced a new pedestal current, $I_{\text{BIC3}} = 1.62 \pm 0.40$ nA. The method of determination of the BIC 3 pedestal current is discussed in Appendix A. The quantity DF_{veto} is the veto duty factor, found by multiplying the veto gate width Δt by the 20 Hz sampling rate. The veto gate width was set to 500 μs, so that

$$\text{DF}_{\text{veto}} = 0.01. \tag{3.8}$$

32

This allows the direct measurement of the galvanic current during each production run:

$$I_{gv} = \left(\frac{Q_{veto}}{T_{run}} - I_{BIC3} \right) \times \frac{1}{DF_{veto}} \,. \tag{3.9}$$

The true beam charge can be then obtained on a run-by-run basis using equations 3.5 and 3.6.

3.3 Target

3.3.1 The MIT Basel Loop

The MIT Basel loop target used for this experiment is described in detail in [32]. The liquid hydrogen cell is a vertical cylinder 1.6 cm in diameter with 4.3 μm Havar walls. Because of the limited vertex resolution of the OOPS-OHIPS system, the small target diameter is necessary to provide the degree of vertex definition required to give adequate spatial resolution around the Central momentum-transfer direction. The thin cell walls also help in this regard by minimizing the resolution degrading effects of small angle scattering in the walls, as well as reducing background events due to interactions with the wall material.

The target system also supports a variety of solid targets which can be moved in and out of the beam on a ladder inside the scattering chamber. For this experiment a solid ^{12}C target was used for the calibration of the spectrometers' optical properties, and a BeO target was used to provide a visual check of beam position at the target. The target ladder system is controlled remotely from the Counting Bay, allowing targets to be changed without hall access.

The liquid hydrogen cell was cooled by a helium gas refrigeration system, which has a maximum cooling power of 200W. A remotely controlled heater with variable power up to 50 W was used to maintain a constant temperature at around 22.57 K, and a pressure of 11.7 psi. Both pressure and temperature were monitored throughout the experiment by a number of sensors, indicated in figure 3-9. All target data were displayed and controlled during the experiment on a personal computer running LabView software in the Counting

Bay.
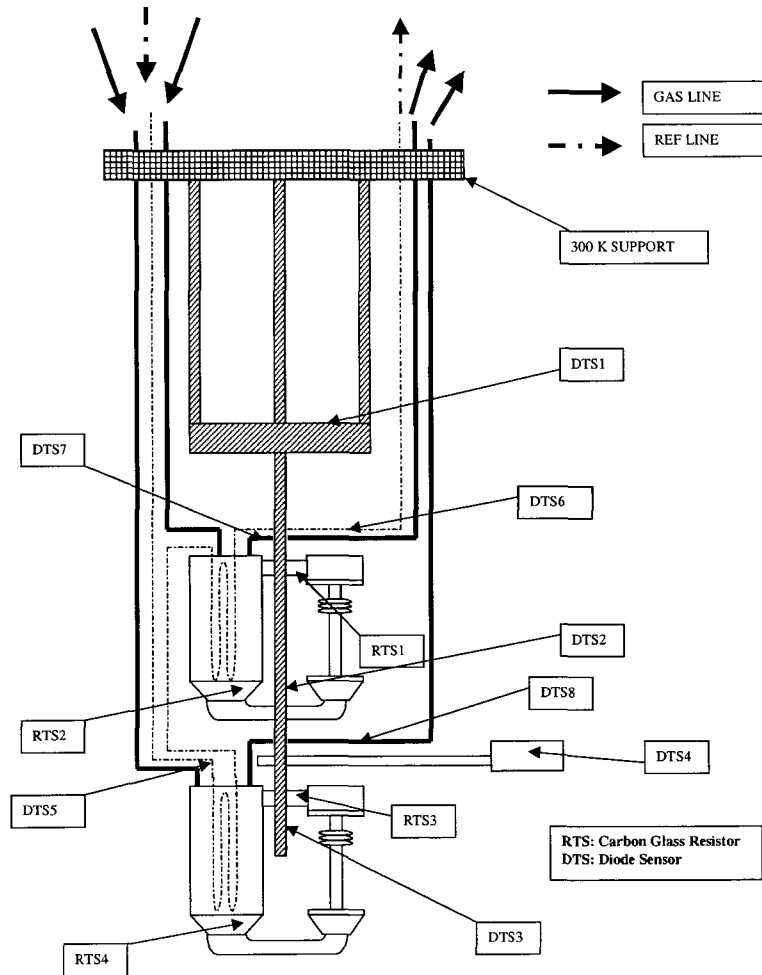
Figure 3-9: The MIT Basel loop target

3.3.2 Target Density Measurements

The target density is calculated from the temperature and pressure readings taken during each run according to an empirical multiparameter fit to the National Institute of Standards and Technology (NIST) database of thermophysical properties of fluids [33]. The paramaterization is of the form

$$\rho(P,T) = (A + BT + CT^2)(1 + D(P - 2.0)) \tag{3.10}$$

34

with temperature T in Kelvins and pressure P in bars. The numerical values of the parameters A–D are listed in table 3.3. This fit is found to agree with the NIST data to better than 0.1% accuracy over the entire range of temperature and pressure given.

$A = 7.32356 \times 10^{-2}$	$C = -5.1501 \times 10^{-5}$
$B = 9.30833 \times 10^{-4}$	$D = 1.9018 \times 10^{-3}$

Table 3.3: Parameters for fitting the target density

Temperature is measured with carbon glass resistor thermocouples at two points in the liquid hydrogen cell (RTS1, RTS2). These were calibrated to target pressure, during the target cool-down period prior to data taking, to an accuracy of ± 0.5 K. Neither the accuracy of the temperature calibration nor of the final density calculation depends upon high-precision pressure measurements. At this level of accuracy, the target density is determined to better than 0.5%. The details of the calibration procedure are described in the Ph.D thesis of Mertz [32].

The target density is stable to within this accuracy from run to run within each data taking period, but between data taking periods there may be some change in density when the target is warmed and re-cooled for hall access, or due to adjustments to the cryosystem made in the interim.

Data set	ρ [g/cm^3]	% error
Kinematics a	0.06794(14)	0.5 %
Kinematics b (1)	0.06775(10)	0.5 %
Kinematics b (2)	0.06813(5)	0.05 %

Table 3.4: Target density ρ

The target density is therefore considered to be constant during each of three uninterrupted data taking periods, with an uncertainty given by the 0.5% measurement accuracy. The data from kinematics a are evaluated as a single run period. The kinematics b target

35

data are evaluated in two stages: the bulk of the data were taken in an uninterrupted series and are evaluated as one set; however an addition six hours of data were taken several days after the first group of measurements, and these are evaluated separately.

All three target data sets are shown with their respective average density values in figures 3-10 and 3-11; the corresponding numerical values and errors are listed in table 3.4.
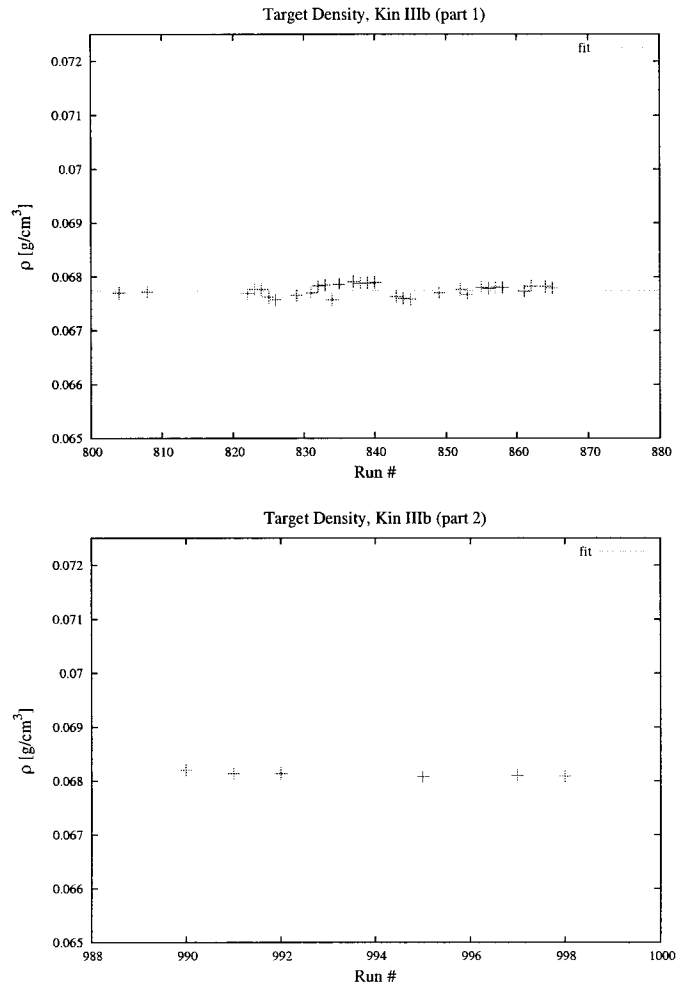
Figure 3-10: Liquid hydrogen target density calculations by run number, kinematics b. The density is taken to be a constant for each plot, and evaluated with a least-squares fit. The error is given by the spread of the data about the mean

36
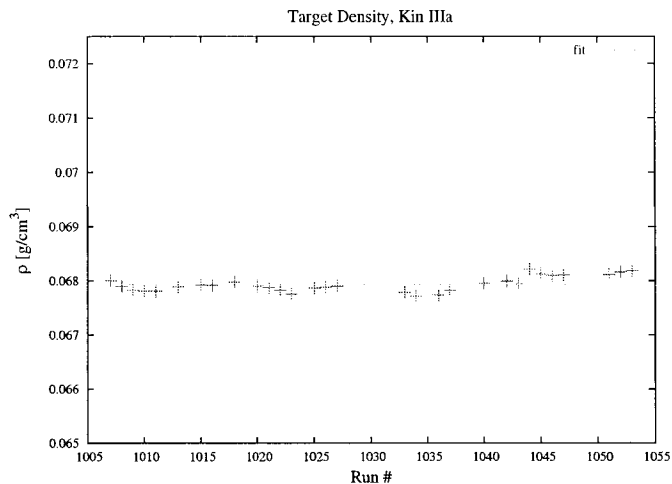
Figure 3-11: Liquid hydrogen target density calculations by run number, kinematics a. The density is taken to be a constant, and evaluated with a least-squares fit. The error is given by the spread of the data about the mean

3.3.3 Target Length

The target length ℓ is defined as the length of the path traversed through the target cell by the beam. The MIT/Bates liquid hydrogen target cell is a cylinder of radius $R = 0.8$ cm, centered at the origin of the lab coordinate system and oriented along the y-axis. The nominal beam defines the z-axis. Ideally, the target length is simply $2R = 1.8$ cm. However, in practice both the finite beam size and the uncertainty in the beam centroid position complicate the calculation. In general, the target length seen by a particle passing through the target parallel to the z-axis, but at some lateral offset x, will be

$$\ell(x) = 2 \times \sqrt{R^2 - x^2}, \tag{3.11}$$

as illustrated in figure 3-12.

37
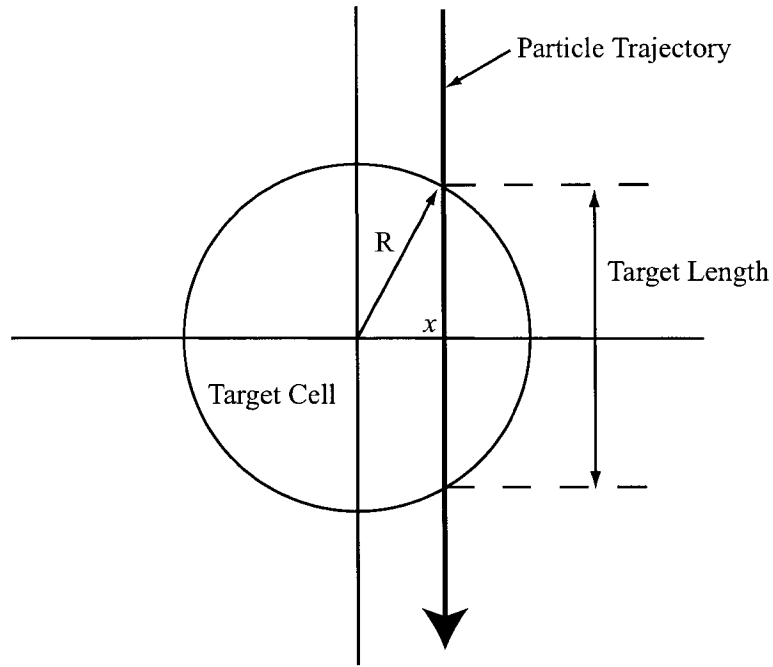
Figure 3-12: The target length for a general incident electron

For a beam of finite size, one needs to average all path-lengths over the x-coordinate, weighting each path-length by the beam intensity profile. The beam has an approximately Gaussian profile, with a width of 0.073 cm (FWHM) projected onto the x–z plane. Assuming that the beam is centered at some position x_0, the weighted average path-length is

$$\langle \ell \rangle_{x_0} = \frac{\int_{-R}^{+R} \ell(x)\, I(x)\, \mathrm{d}x}{\int_{-R}^{+R} I(x)\, \mathrm{d}x} \tag{3.12}$$

where $I(x)$ is the Gaussian weighting function describing the intensity of the beam as a function of position,

$$I(x) = \frac{1}{\sqrt{2\pi}\sigma} e^{-(x-x_0)^2/2\sigma^2} \tag{3.13}$$

with the standard deviation $\sigma = \mathrm{FWHM}/(2\sqrt{2\ln 2}) = .031$ cm. The calculation of the integrals is done numerically; for a beam centered on the origin, $x_0 = 0$, the average target-length is

$$\langle \ell \rangle_0 = 1.5988\,\mathrm{cm}\,. \tag{3.14}$$

38

This is the central value which is used for all cross section calculations. Because there is an uncertainty associated with the central beam position x_0, there is a corresponding uncertainty in the average path-length. During the data taking, the beam position was periodically checked visually by moving the target ladder to position a solid BeO target in the beam path in place of the hydrogen cell. Using a reticule, the beam position was confirmed to be on center within an estimated uncertainty of $\sigma_{\mathrm{pos}} = \pm 0.1$ cm.

The standard deviation of the average target-lengths corresponding to possible beam positions is calculated by

$$\sigma_{\langle \ell \rangle}^2 = \frac{\int_{-R}^{+R} (\langle \ell \rangle_{x_0} - \langle \ell \rangle_0)^2 \, g(x_0) \, \mathrm{d}x_0}{\int_{-R}^{+R} g(x_0) \, \mathrm{d}x_0} \tag{3.15}$$

where $g(x_0)$ is the Gaussian weighting function corresponding to the probability of the beam position being displaced by x_0 from it's nominal position at the origin,

$$g(x_0) = \frac{1}{\sqrt{2\pi}\sigma_{\mathrm{pos}}} e^{-x_0^2/2\sigma_{\mathrm{pos}}^2} \, . \tag{3.16}$$

All integrals over x and x_0 are calculated numerically, as before. The standard deviation is found to be

$$\sigma_{\langle \ell \rangle} = 0.022 \, \mathrm{cm} \, , \tag{3.17}$$

or 1.39% of the central value.

3.4 Spectrometers

3.4.1 Electron Spectrometer: OHIPS

The One-Hundred Inch Proton Spectrometer was originally designed and built, as the name indicates, to detect protons. Its redesign for use as a high-resolution electron detector during the 1998 OOPS program at Bates is documented in a number of Ph.D theses; see, for example Kunz [34], Mertz [32] and Jiang [35].

39
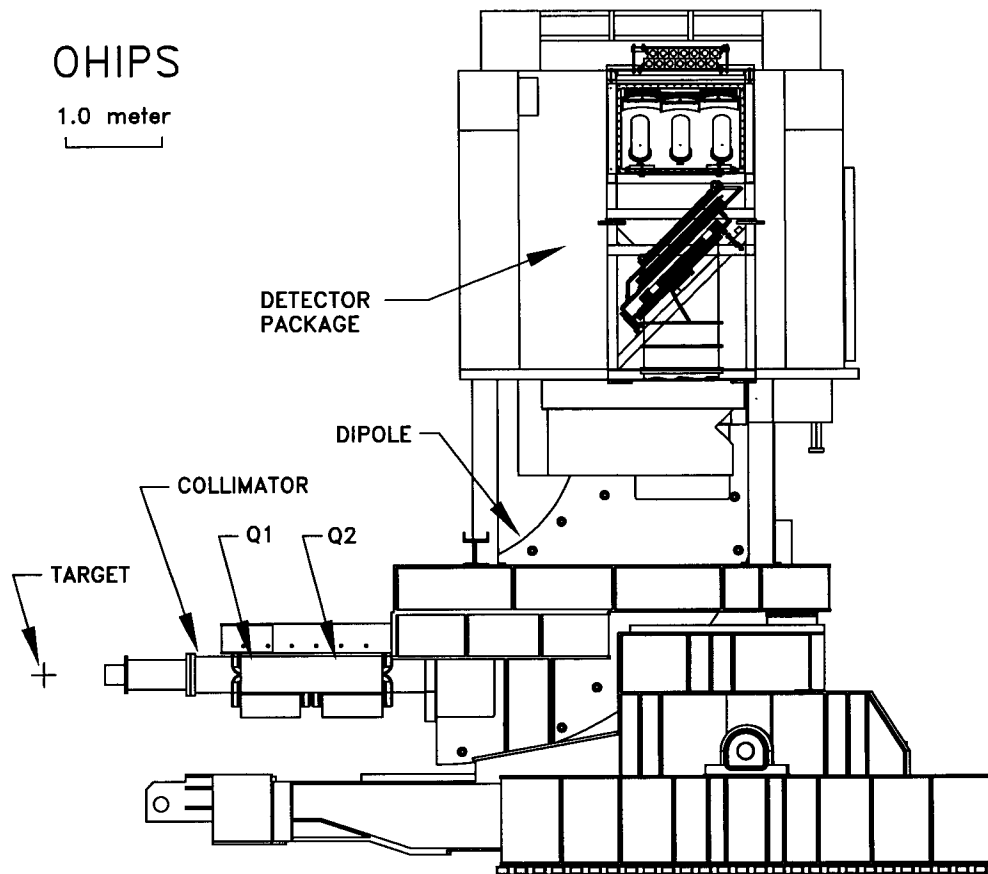
Figure 3-13: Schematic view of the OHIPS spectrometer

OHIPS uses a dual quadrupole, single dipole (Q-Q-D) design to focus in both the x and y planes. It is therefore able to resolve the vertex position along the target length, in addition to electron momentum and angles. The spectrometer configuration is shown in figure 3-13.

The entrance to the first quadrupole magnet was located 2.0 meters from the target center. This length defines the "drift distance". An 8-inch thick lead collimator is located forward of the first quadrupole at a distance of 157.0 cm from the target. The collimator has a rectangular opening measuring 17.3 cm vertically by 7.5 cm horizontally, subtending a nominal solid angle acceptance of 5.26 msr.

Maximum Momentum	1390 MeV
Momentum resolution	1.4×10^{-3}
Drift Distance	2.0 m
Collimator Distance	1.57 m
Momentum Acceptance	$\pm 7\%$
Nominal Solid Angle	5.26 msr
θ Acceptance	$\pm$ 55.0 mrad
ϕ Acceptance	$\pm$ 23.9 mrad
Dipole Radius	2.54 m
Flight Path	9.7 m
Bend Angle	$90°$

Table 3.5: OHIPS properties

The OHIPS detector package is shown in figure 3-14. Two cross-wire vertical drift chambers (VDCX1 and VDCX2) are installed at an angle of 45° with respect to the central ray in order to overlap with the focal plane as much as possible. Three Bicron-408 plastic scintillators , read out by photomultiplier tubes at both sides, create the trigger. Between the second and third layer scintillators is a threshold gas-Čerenkov detector which, along with a double layer of lead glass detectors located behind the third scintillator, can be used for particle identification.

41

SPECTROMETER
CENTER LINE

SHOWER
COUNTER

S3

CHERENKOV
COUNTER

S2

45°

S1

VDCX2

VDCX1

VACUUM
WINDOW

TYPICAL
TRACK

OHIPS DETECTOR
PACKAGE

1 foot
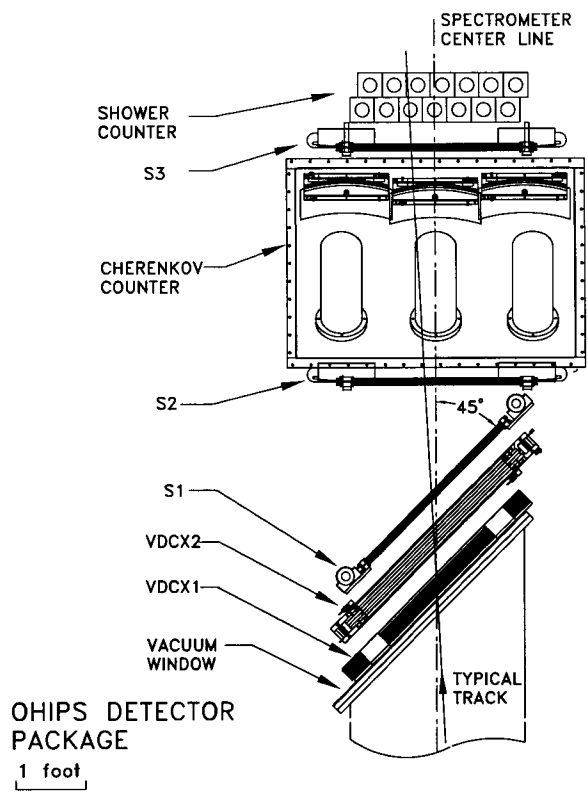
Figure 3-14: The OHIPS detector package

3.4.2 Pion Spectrometers: OOPS

The OOPS system consists of four identical lightweight (16 ton) magnetic spectrometers, with minimal shielding, designed to allow relatively free placement in space around the target. Three of these modules were used for this experiment. The OOPS modules have been previously described in rather extensive detail in [36], [37] and [38]; therefore only a summary of their features and specifications is presented here.

42
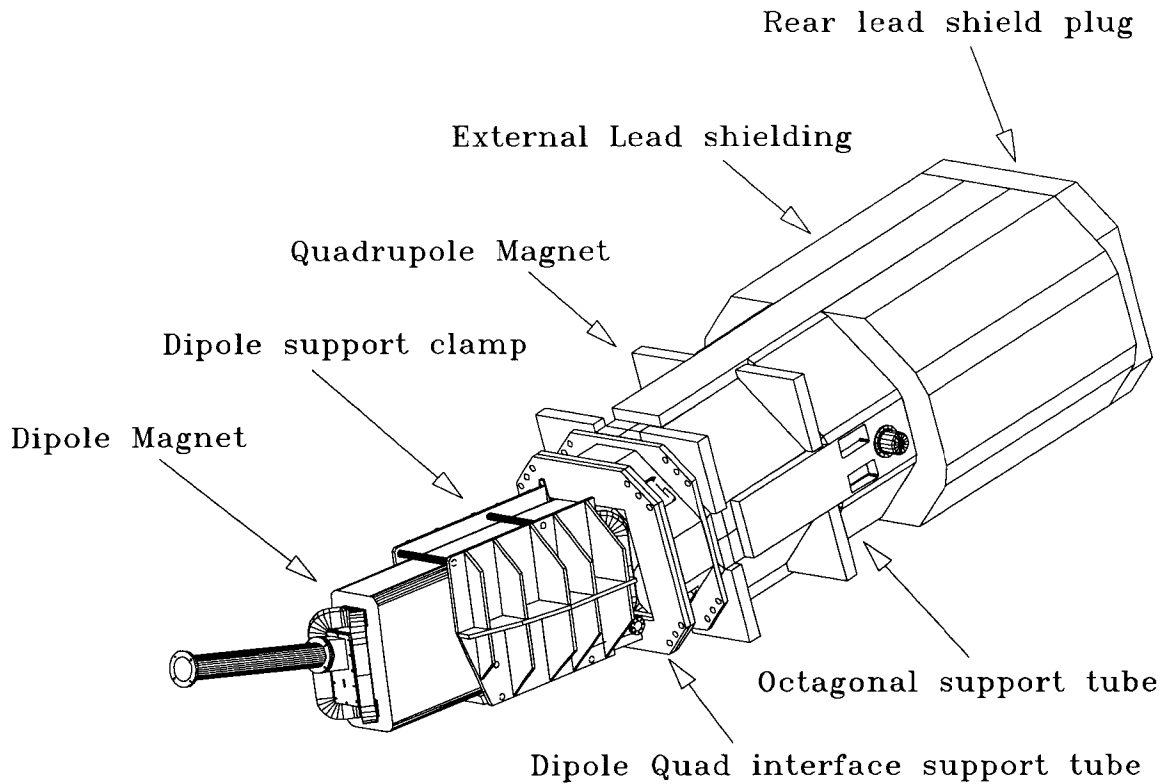
Figure 3-15: Major components of an OOPS spectrometer

The OOPS modules use a dipole-quadrupole design to allow the closest possible packing on multiple-spectrometer configurations. A shallow dipole bending angle of 21.7° allows a maximum possible central momentum setting of 830 MeV/c. Because there is only one quadrupole, the OOPS modules are single focusing, in the dispersive x-direction only. This means that OOPS is able to resolve particle momentum, but not vertex position along the target length. The OOPS focal plane is nearly flat, and lies at an angle of about 13° to the central ray.

43

Maximum Momentum	830 MeV
Momentum resolution	< 0.5%
Drift Distance	1.40 m
Collimator Distance	1.296 m
Momentum Acceptance	±15%
Nominal Solid Angle	1.20 msr
θ Acceptance	± 25.0 mrad
ϕ Acceptance	± 12.0 mrad
Angular Resolution	1.30 mrad
Flight Path	418.3 cm
Dipole Radius	3.18 m
Bend Angle	21.7°

Table 3.6: OOPS properties
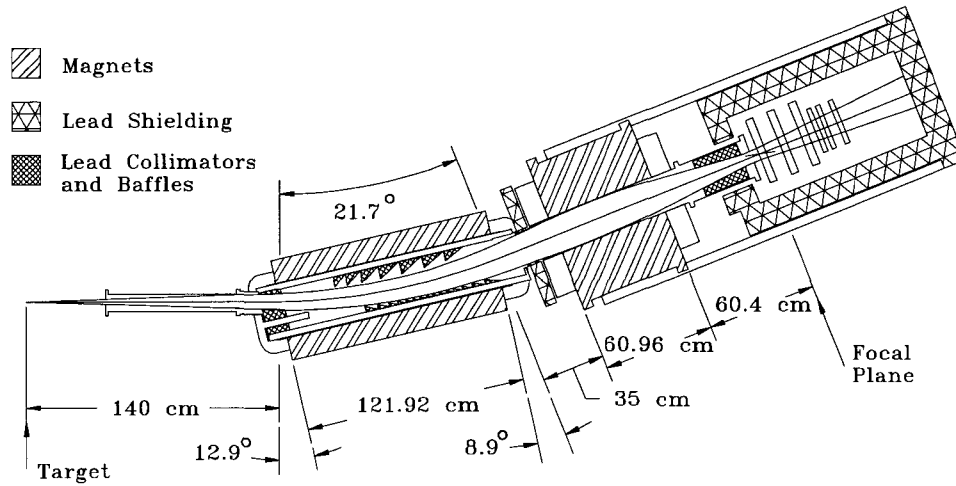
Figure 3-16: Cross sectional view of an OOPS module showing collimators and ray tracing

For this experiment, OOPS A was mounted on a satellite platform for in-plane detection, while OOPS B and C were suspended from the Gantry (see figure 3-3) to make out-of-plane measurements at a common floor angle. All OOPS' were located at a drift distance of 1.40 m from the target. The distance to the OOPS front collimator, located forward of the dipole magnet, was 129.63 cm for all modules. The collimator has dimensions of 8.33 cm vertically, by 3.13 cm horizontally, and subtends a solid angle of 1.20 msr.

The OOPS detector package consists of three Horizontal Drift Chambers (HDC) for

44

particle tracking and three layers of scintillators for triggering and particle identification. Each HDC consists of two orthogonal wire planes for position detection in the x and y directions. Each of the three scintillators is read out by photomultiplier tubes on two sides.
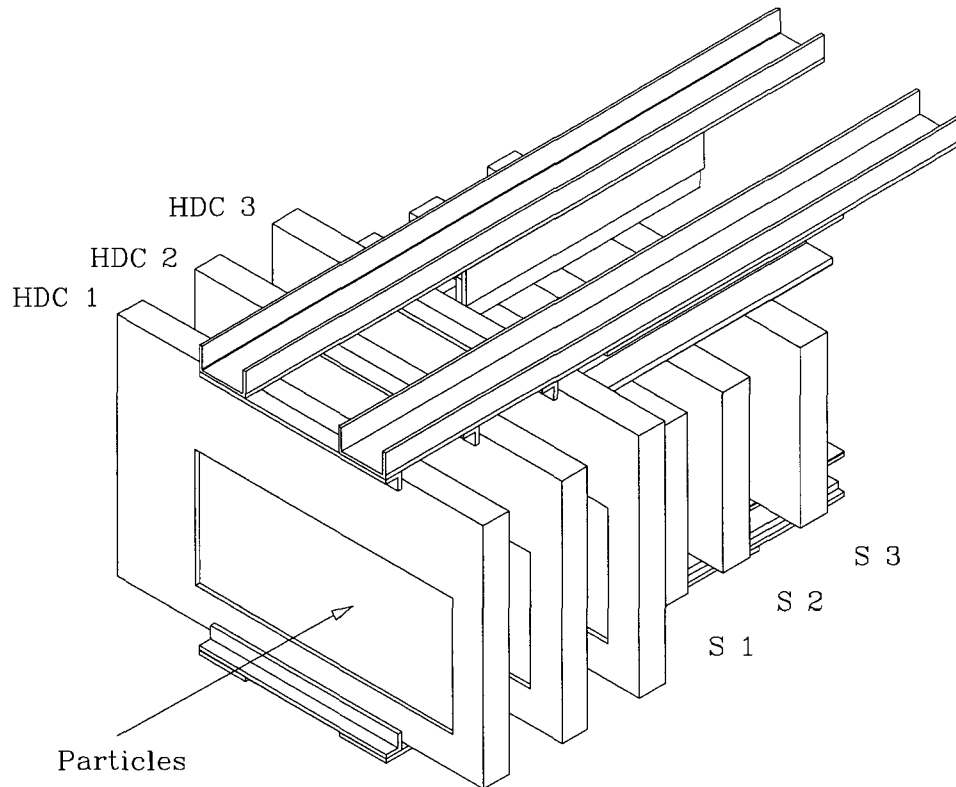
Figure 3-17: The OOPS detector package

3.5 Electronics and Data Acquisition

3.5.1 Coincidence Trigger Electronics

The output of the spectrometer detector systems consists of analog electronic pulses from the individual components: wire chambers, scintillators, lead glass and Čerenkov detectors. This raw detector data must be digitized, decoded and stored before it can be analyzed. The initial signal processing is handled by the Coincidence Trigger electronics, which were housed in a shielded hut in the Bates South Hall itself. A simplified schematic view of the OOPS and OHIPS coincidence electronics is shown in figure 3-19.

45
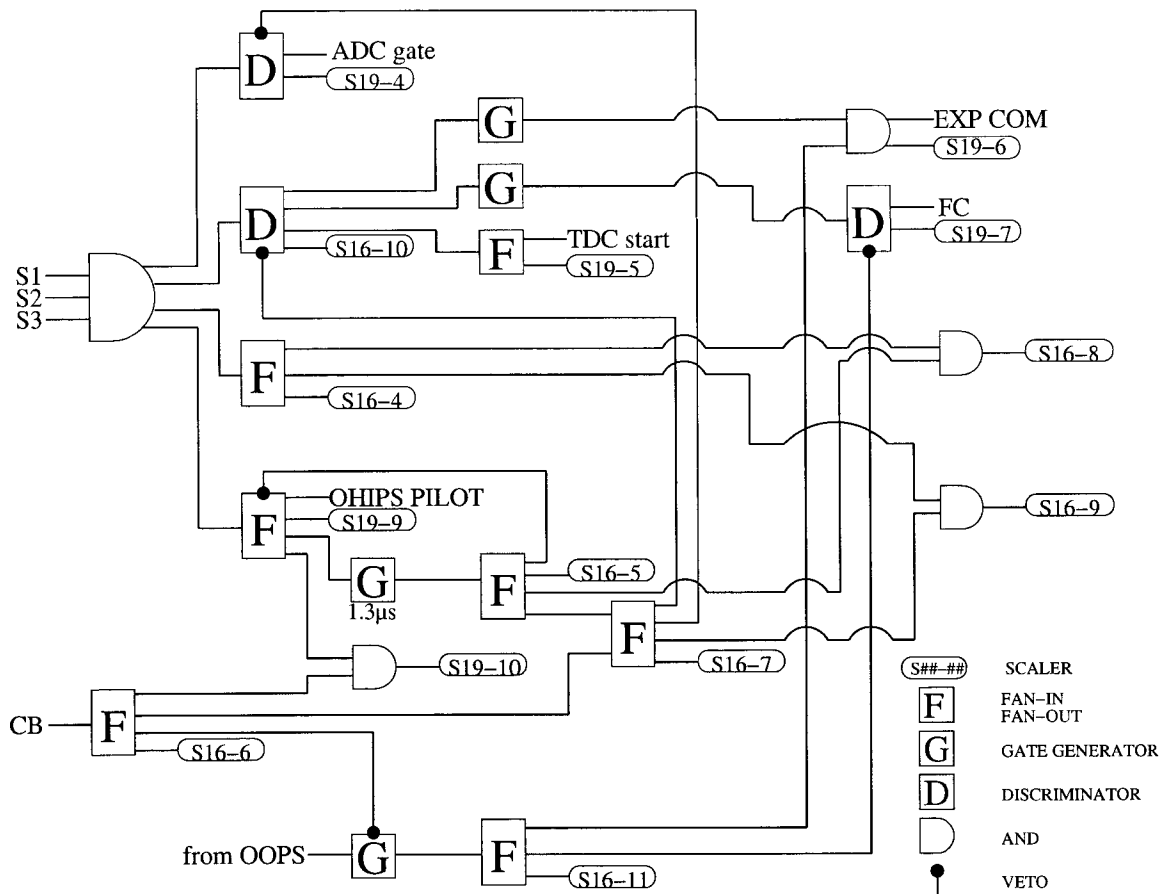
Figure 3-18: Schematic diagram of the OHIPS trigger electronics.

The OOPS trigger is formed by signals from the three scintillators, each of which is read out by phototubes on each side. Each pair of phototube signals is first combined at an AND gate to form a left-right coincidence signal. The left-right coincidence from each of the three layers is fed into an Octal Logic Module (OLM), which can be controlled by software to vary the trigger conditions if necessary during the experiment. All of the data for this experiment were taken with a three scintillator coincidence required to form a trigger.

The OHIPS trigger is similarly formed by the coincidence of all three scintillator layers. Figure 3-18 shows a schematic diagram of the OHIPS trigger electronics. Some portion of the raw OHIPS triggers are not processed any further due to the OHIPS self-inhibit circuit, discussed later in this section. Those signals which survive the self inhibit and proceed through the remaining trigger electronics are referred to as the OHIPS pilot signals.

46
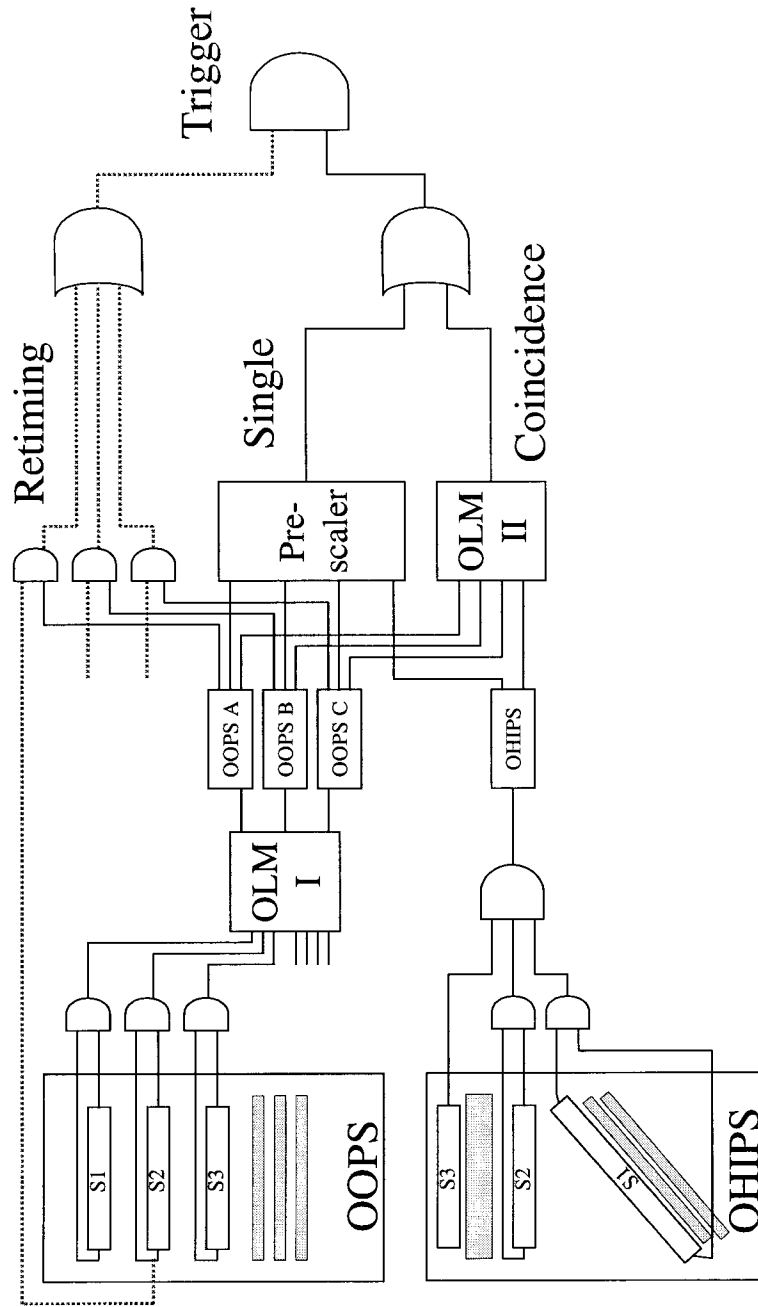
Figure 3-19: Simplified schematic diagram of the OOPS-OHIPS coincidence electronics circuit. Note only one OOPS module is shown explicitly in the diagram; the others are identical.

Both the OOPS trigger and OHIPS pilot signals are then fanned out into single-arm and coincidence branches, which are processed separately.

Single arm events occur with a much higher frequency than coincidences. In order to

47

prevent the single arm signals from swamping the data acquisition, all singles are prescaled through random coincidence with a signal generator, the pulse-rate and width of which can be set to determine what fraction of singles events are kept.

The OOPS-OHIPS coincidence is determined in a second OLM module, which creates an output if any OOPS fires in coincidence with OHIPS, within a 120 ns gate.

Both the single arm and coincidence signals are then sent through an OR gate, which outputs a signal to the final logic stage, an AND with a re-timing signal taken from the left side of the OOPS second layer scintillator (S2L). The S2L re-timing signal is passed through a delay line so that it always arrives at the final AND gate just after the start, but before the end, of the final trigger signal coming from the single and coincidence circuits. In this way, the S2L signal always determines the timing of the trigger, which greatly helps to reduce jitter in the coincidence Time-of-Flight peak.

3.5.2 Veto Circuits

While the electronics are processing one event, veto circuits are used to prevent new events from being recorded and confusing the trigger. Two independent veto circuits are implemented:

1. The OHIPS 1.3 μs self-inhibit

2. The front-end veto

The OHIPS self-inhibit and front-end vetoes create dead times in the data acquisition, which we account for with the Dead-Time correction factor η_{dt} (see section 4.4.1).

OHIPS 1.3 μs self-inhibit

The OHIPS VDC information is processed by the OHIPS on-board Drift Chamber Operating System (DCOS). The DCOS may not receive a new trigger while it is already processing one; therefore whenever a trigger occurs, a fast onboard veto circuit is used to inhibit the scintillators for 1.3 μs before a new trigger can occur. If the event is rejected by the coincidence electronics, a fast clear signal is sent which ends the inhibit earlier in order to

48

maximize live time. If the event is read out, the one-per-beam-burst veto is implemented, taking over the inhibit before the self-inhibit expires.

Front-end veto

The front-end veto inhibits the entire electronics once a coincidence trigger is received. It is also used to shut down data acquisition during times when the system should not be read out. These include the period between beam spills during which cosmic rays could trigger the spectrometers and cause unwanted background, and periods when data acquisition is stopped (run stops, beam trips, etc.).

3.5.3 Data Acquisition System

The data acquisition system is based on the "Q" system developed at the Los Alamos Meson Physics Facility (LAMPF). A LAMPF CAMAC trigger module provides the interface between the trigger electronics and the computer data acquisition system, shown in figure 3-20. The LAMPF trigger receives interrupts for different event types from NIM trigger signals, and initiates the data read out by the Micro-programmable Branch Driver (MBD) front-end computer. The MBD front-end computer initially reads a pattern word from a LATCH module which was fed by triggers from each spectrometer to determine which spectrometers fired in a particular event. The MBD then reads the corresponding CAMAC modules .

The data is shipped to a micro VAX computer running Q, the "producer", which writes the entire data stream to a removable hard disk and ships some fraction to a faster VAX workstation, the "consumer", for online analysis. Data are shipped only if CPU time is still available after reading and writing data; the fraction of data analyzed online therefore depends on the trigger rate and the VAX workload.
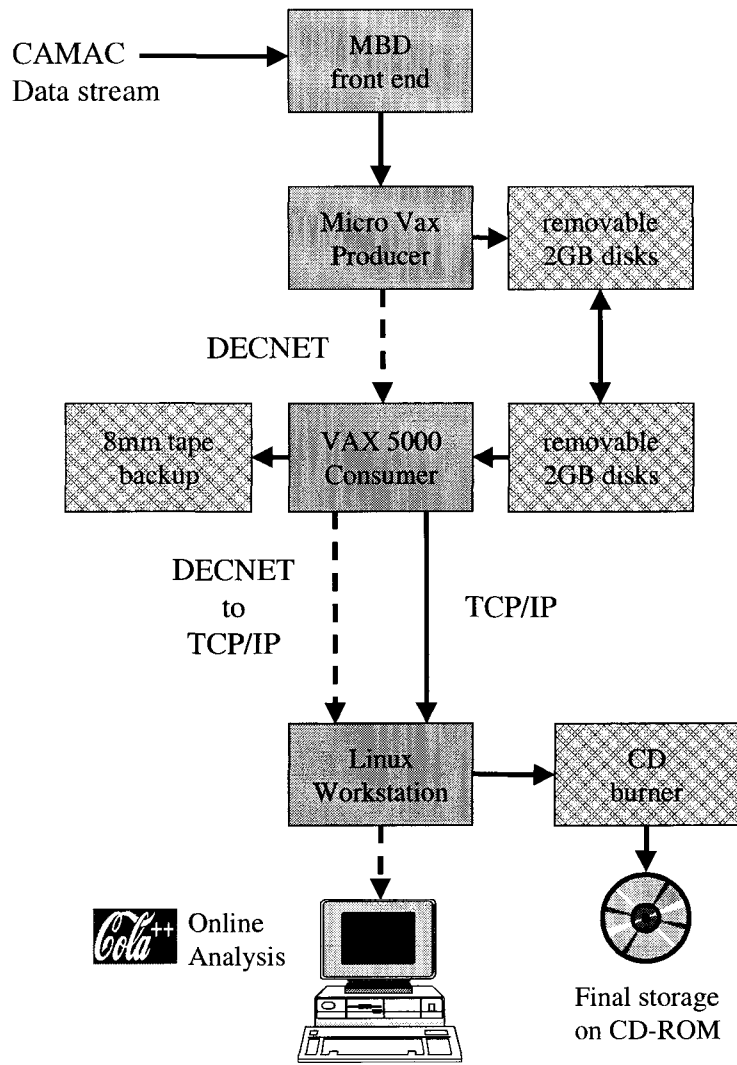
Figure 3-20: Flow diagram of the data acquisition system.

In a previous design the consumer performed online analysis using the analyzer and histogramming packages that are part of the Q system. These packages are outdated, however, and not adequate to the needs of modern data analysis and display. Now, the Q system is used only for the front-end data acquisition, storage and retrieval, and the job of the VAX consumer is only to convert the DECNET data stream into TCP/IP so that it can be transferred via ethernet to a dual Pentium III Linux Workstation. This machine converts the Q data stream to the Cindy format, and then runs a modified version of the Mainz Cindy OnLine Analysis (COLA) system, denoted as ColaMIT, to accomplish the

50

task of on and off line data analysis.

The removable hard disks containing the full data stream written out by the producer were periodically removed and loaded into the consumer workstation. From there the data would be copied to tape, and also be sent to another Linux workstation where they were burned onto CD-ROM for storage.

In the offline analysis, the data were replayed from CD, analyzed with ColaMIT and converted to HBOOK format for final analysis and display using PAW [39] or ROOT [40].

51

CHAPTER 4

Data Analysis

4.1 Electron and Pion Momentum Vectors

The momentum vectors of the electron and pion at the target are determined by the magnetic spectrometers. The raw data recorded from the OOPS and OHIPS drift chambers are the wire numbers struck in each of the chambers' planes, and the drift times for each struck wire. The drift times are converted into drift distances, giving position resolution in each plane much smaller than the actual wire spacing.

Coordinate pairs (x_i, y_i) are thus obtained in the transverse plane at the location z_i, measured along the central ray, of the ith chamber. These three points are used to fit the trajectory through the detector package of each particle. The position and Cartesian angles at which the trajectory of each particle crosses the focal plane is calculated; this n-tuple of chamber coordinates is then transformed using a set of optical matrix elements into the reconstructed momentum, Cartesian angles and, in the case of OHIPS, the vertex location of that particle at the target.

4.1.1 Decoding the Drift Chambers

Each OOPS Horizontal Drift Chamber (HDC) consists of two perpendicular wire planes in the x and y direction. The x and y planes have similar layouts, with 21 signal (anode) wires in the x and 49 in the y directions, with a wire spacing of 8.128 mm. A schematic of

52

a generic wireplane is shown if figure 4-1. Between the signal wires are additional cathode
wires, which are alternately connected to one of two buses, labeled "odd" and "even".
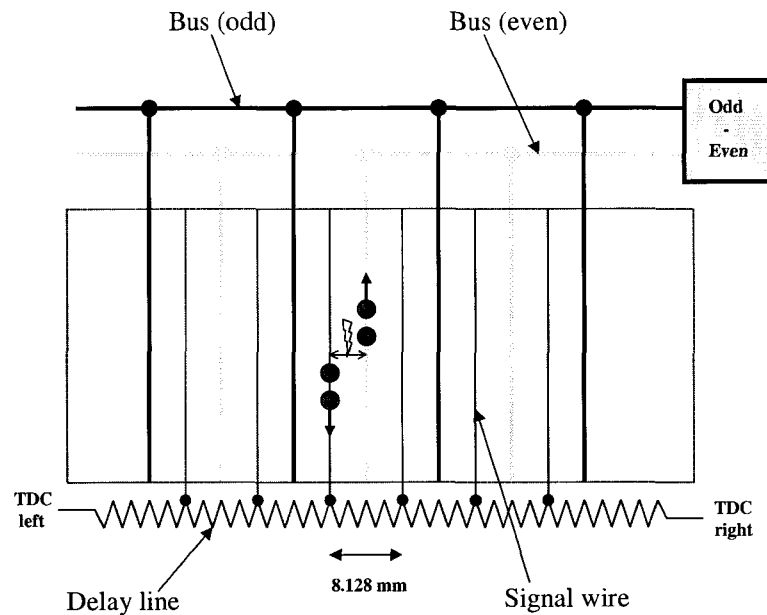
Figure 4-1: The HDC plane internal layout, showing signal (anode) and odd-even (cathode) wires.

When a charged particle passes through the detector package, it deposits energy by
ionization in the chambers and the scintillators. In the scintillators, this results in the
emission of light which is transformed into an electrical pulse by the photomultiplier tubes
at either end.

The ionization in the chamber gas produces electrons and positive ions which are accel-
erated by the electric field inside the chamber toward the signal and cathode wires. The
typical electron drift velocity is around 50 μm/ns. These ionize other atoms along their
path in an avalanche process to create a measurable pulse on the wire. This is registered
by two Time-to-Digital Converter (TDC) channels, one at either end of the delay line. De-
pending on which cell in the particle passed through, each TDC records a different time for
the event.

53

4.1.2 The TDC Difference Spectrum

The time difference between the left and right TDCs is a linear function of the number of the struck signal wire. The time recorded by the left or right TDC is

$$TDC_{l(r)} = \delta t_{\mathrm{drift}} + \delta t_{\mathrm{del}_{l(r)}} \tag{4.1}$$

where $\delta t_{\mathrm{drift}}$ is the drift time of electrons to the signal wire, and $\delta t_{\mathrm{del}_{l(r)}}$ is the signal travel time through the delay line to the left (right) TDC. The TDC difference is then

$$TDC_{\mathrm{diff}} = TDC_l - TDC_r = \delta t_{\mathrm{del}_l} - \delta t_{\mathrm{del}_r} \tag{4.2}$$

The delay time $\delta t_{\mathrm{del}_{l(r)}}$ is proportional to the length $L^n_{l(r)}$ of delay line between the nth signal wire and the left (right) TDC, which is given by

$$L^n_l = n\delta L \tag{4.3}$$

$$L^n_r = (n_{\mathrm{max}} - n)\delta L \tag{4.4}$$

where δL is the inter-wire spacing and n_{max} is the total number of signal wires in the chamber. Therefore,

$$TDC_{\mathrm{diff}} \sim (2n - n_{\mathrm{max}})\delta L \tag{4.5}$$

This structure is clearly seen in figure 4-2, where the distinct peaks in the time difference spectrum relate to the struck signal wires.

In order to fit the wire numbering to the TDC Difference spectrum, a "white" calibration spectrum which illuminates the entire chamber is recorded by turning the focusing quadrupole magnet off. A wire number n is assigned to each peak, and the centroid of the peak, TDC^n_{diff} is determined by fitting the peak with a Gaussian function. The wire numbers are then fit to the TDC spectrum with a linear function:

$$n = A \times TDC^n_{\mathrm{diff}} + B \tag{4.6}$$

54
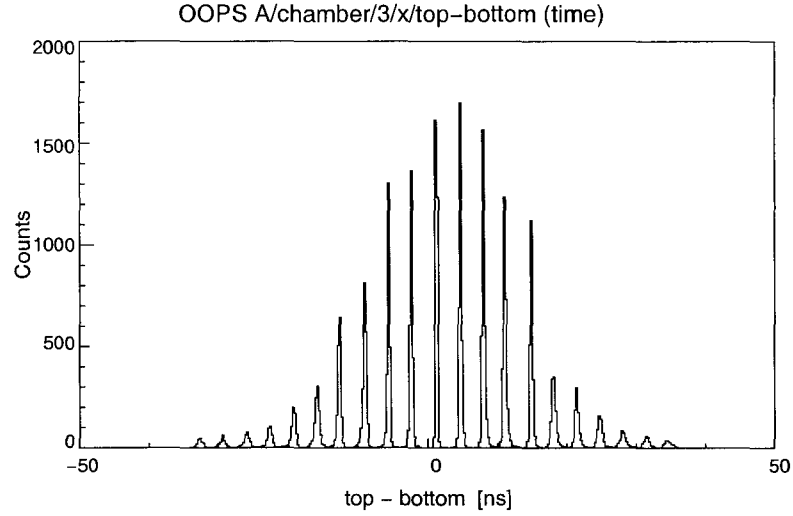
Figure 4-2: The TDC difference spectrum for a typical OOPS HDC x-plane

The wire-number spectrum is shown in figure 4-3.

4.1.3   The TDC Sum Spectrum

The sum of the left and right TDC readings is a direct measure of the drift time, since the sum of the two delay line paths is constant with respect to the wire number:

$$TDC_{\text{sum}} = TDC_l + TDC_r = 2\delta t_{\text{drift}} + \delta t_{\text{del}_l} + \delta t_{\text{del}_r} \tag{4.7}$$

Clearly the sum $\delta t_{\text{del}_l} + \delta t_{\text{del}_r}$ is proportional to the sum of the lengths of the delay lines,

$$\delta t_{\text{del}_l} + \delta t_{\text{del}_r} \sim L_l^n + L_r^n = n_{\text{max}}\delta L \tag{4.8}$$

so we can write

$$TDC_{\text{sum}} = 2\delta t_{\text{drift}} + \text{Const.} \tag{4.9}$$

A typical TDC sum spectrum is shown in figure 4-4.

55
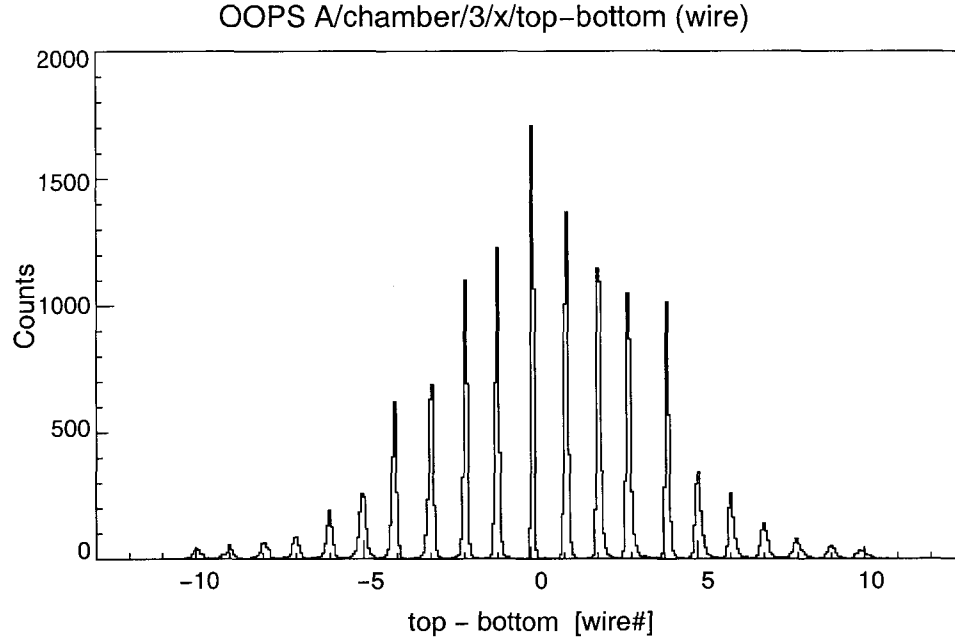
Figure 4-3: The X plane Wire-Number spectrum.

4.1.4 Drift-Time to Distance Conversion

The drift time information at each chamber can be converted into a drift distance measurement to further localize the track within the HDC cell. In order to correlate the drift time with distance, a "white" calibration spectrum is recorded which illuminates all the chambers in the cell homogeneously. To the extent that the cell illumination is uniform, the drift distance as a function of drift time is obtained by the integral of the drift time spectrum,

$$d_{\mathrm{drift}}(T) = N \int_0^T dt_{\mathrm{drift}}\, n(t_{\mathrm{drift}}) \tag{4.10}$$

where the normalization constant is chosen so that for $T = T_{\max}$, the maximum practical drift time for the cell, $d(T_{\max}) = L_{\mathrm{cell}}$, the length of the drift cell. An example of the drift-time to calibration curve is shown in figure 4-5. The conversion is stored for use by the COLA analyzer as a simple look-up table.

A histogram of the drift distances, superimposing all cells, reveals a flat drift-distance spectrum indicating even cell illumination (see figure 4-6). An inhomogeneous drift distance spectrum would indicate that the drift-time to distance conversion is incorrect.

56
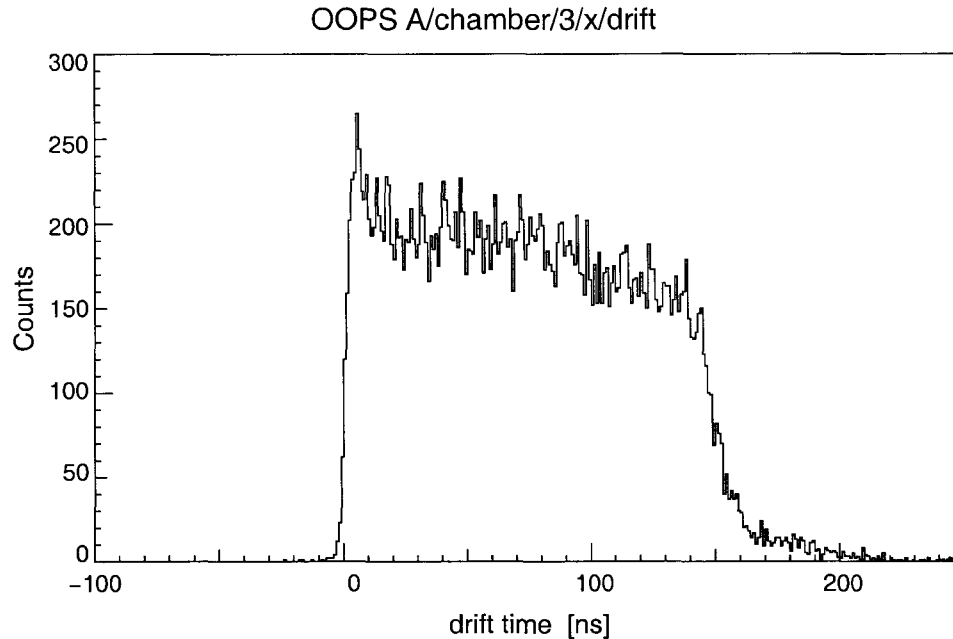
Figure 4-4: The TDC Sum, or Drift-Time, spectrum. The zero-point of the time scale is arbitrary, and chosen for convenience

4.1.5 The Odd-Even ADC Spectrum

The Odd-Even ADC spectrum is used to determine on which side of the signal wire a particle passed through the chamber plane. The signals from the odd and even cathode buses are fed into a fast differential amplifier. The amplifier is strongly re-coupled, so that depending only on the polarity of the two incoming signals the output takes on a threshold value with the respective polarity. A DC offset is added to shift both levels into the positive voltage region. The output of the differential amplifier is fed into an Analog-to-Digital Converter (ADC).

The spectrum is divided into three regions: Events producing signals within 3σ of the right (left) peak are assigned with high confidence to the right (left) side of the signal wire, and the drift distance is added (subtracted) to the wire position to determine the chamber plane coordinate for that event.

In the central region, events are assigned right or left depending on which side of the midpoint of the spectrum they appear. These events are treated with less confidence, and the coordinates determined for such events are weighted in the track-fitting procedure by

57
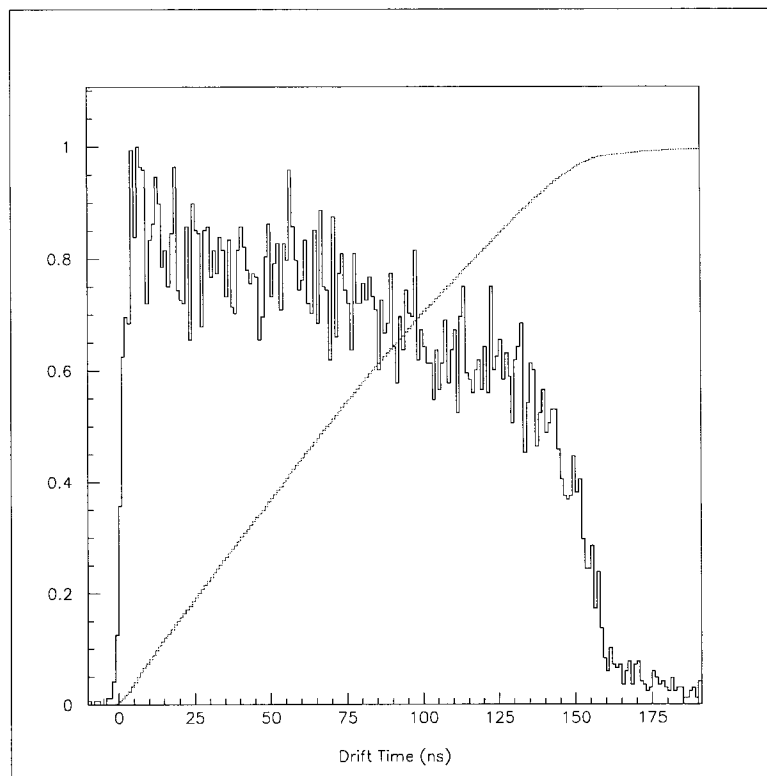
Figure 4-5: The drift-time spectrum, and it's integral. Scaled to the cell size, the integral gives the drift-time to distance conversion.

the inverse of their relative distance from the peak region. Thus, the track fitted to an event with poor Odd-Even resolution in one chamber will be determined largely by the coordinates at the other two chambers

Wire Chamber Resolution

To monitor the resolution of the position measurements in the wire chamber planes, we evaluate the quantities

$$\Delta x = x_2 - \frac{x_1 + x_3}{2} \tag{4.11}$$

$$\Delta y = y_2 - \frac{y_1 + y_3}{2} \tag{4.12}$$

for each event; this is the distance by which the coordinate measured in the second plane deviates from a line drawn between the first and third plane coordinates. This gives a peak

58

OOPS A/chamber/3/x/distance
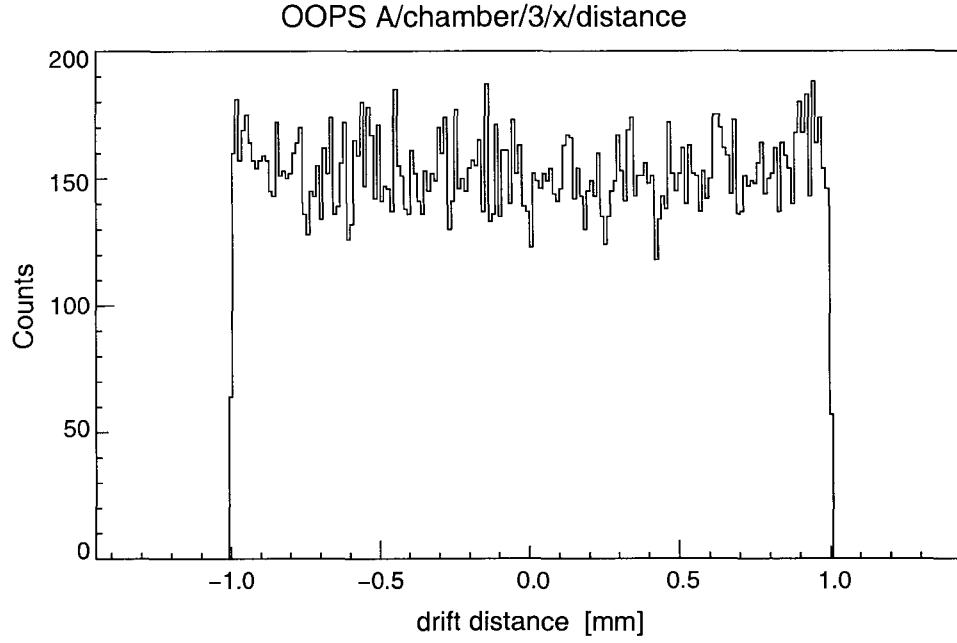
Figure 4-6: The X plane Wire-Number spectrum.

centered at the origin; Figures 4-8 and 4-9 show typical wire chamber resolution peaks from the experiment.

If the errors in the position measurements at each wire plane were zero, these resolution peaks would be delta functions. The spread $\sigma_{\Delta x}$ (and similarly for Δy) in the peak is related to the errors in the individual wire chamber planes by

$$\sigma_{\Delta x}^2 = \sigma_{x_2}^2 + \frac{1}{4}(\sigma_{x_1}^2 + \sigma_{x_3}^2), \tag{4.13}$$

or, with the simplifying assumption that all three wire chamber planes have the same uncertainty,

$$\sigma_x = \frac{\sigma_{\Delta x}}{\sqrt{1.5}}. \tag{4.14}$$

Typical resolution measurements for OOPS are $\sigma_{\Delta x} = 0.24$ mm and $\sigma_{\Delta y} = 0.31$ mm,

59
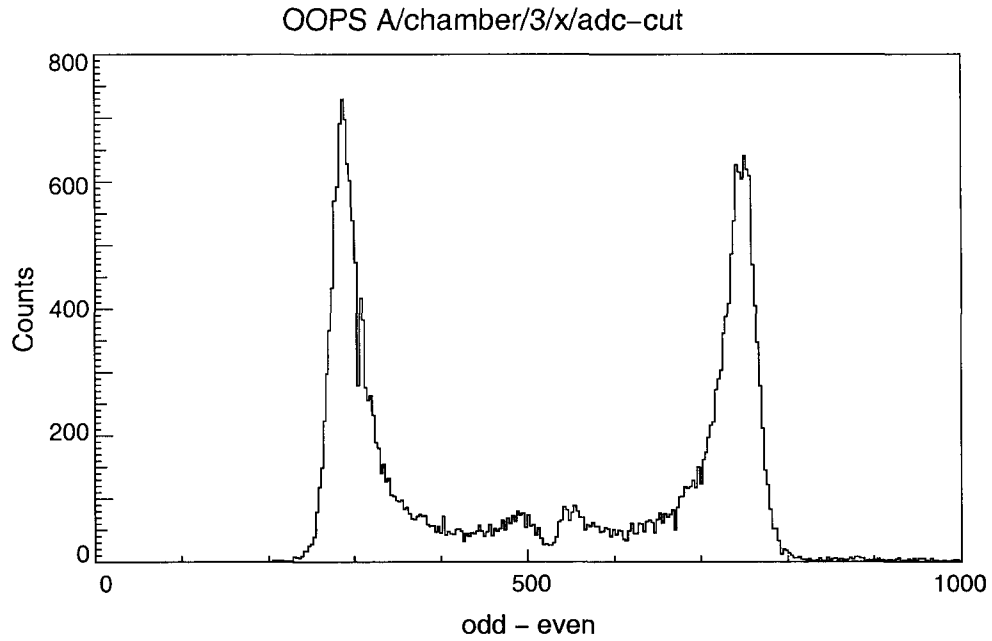
Figure 4-7: The X plane Wire-Number spectrum.

corresponding to errors at the individual wire chamber planes of

$$\sigma_x = 0.20\text{mm} \tag{4.15}$$

$$\sigma_y = 0.27\text{mm} \tag{4.16}$$

Software cuts may be used to eliminate events with poor resolution as necessary; a 3 σ cut around the peaks in figures 4-8 and 4-9 serves to remove from the analysis events that are inaccurately reconstructed. Data lost to such cuts is treated as part of the overall chamber inefficiency, and must be corrected for when calculating the cross sections. This correction factor is calculated in section 4.4.1.

4.1.6 Track Fitting

For each event, transverse coordinate pairs x and y are determined as described above at each of three chamber plane layers, and the longitudinal coordinates z are given by the location of each wire chamber plane. Particle tracks are determined simply by fitting to the three sets coordinates (x, y, z) for each event with a straight line. The x and y-projections

60

OOPS A/chamber/2 − (1+3)/2 (x)
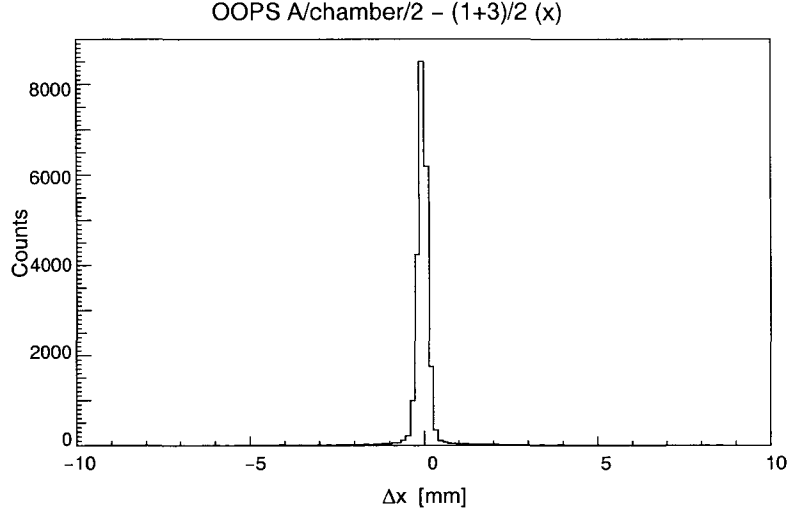
Figure 4-8: OOPS X plane track resolution

are fit separately as functions of the transport z coordinate,

$$x = \tan \theta_{\text{ch.}} \, z + x_{\text{ch.}} \qquad (4.17)$$

$$y = \tan \phi_{\text{ch.}} \, z + y_{\text{ch.}} \, , \qquad (4.18)$$

where the parameters $x_{\text{ch.}}$, θ, $y_{\text{ch.}}$, ϕ are the *virtual chamber coordinates*, or simply "chamber coordinates", which describe the position and Cartesian angles at which the particle trajectory crosses the plane of the first wire chamber.

4.1.7 Target Coordinates

The chamber coordinate ntuple $(x_{\text{ch.}}, \theta_{\text{ch.}}, y_{\text{ch.}}, \phi_{\text{ch.}})$ is mapped to a corresponding ntuple of coordinates for that event at the target $(\Delta p, \Theta, y, \Phi)$ using a set of polynomial matrix elements, which characterize the optical properties of the spectrometers. The general form

61
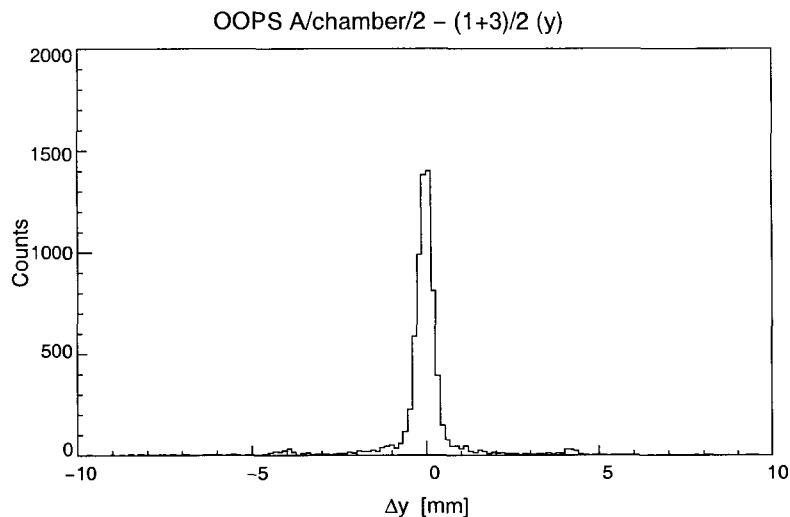
Figure 4-9: OOPS Y plane track resolution

of the coordinate transformations are

$$\Delta p = \sum_{i,j,k,l} \langle \Delta p \,|\, ijkl \rangle \, x_{\mathrm{ch.}}^i \, \theta_{\mathrm{ch.}}^j \, y_{\mathrm{ch.}}^k \, \phi_{\mathrm{ch.}}^l \qquad (4.19)$$

$$\Theta = \sum_{i,j,k,l} \langle \Theta \,|\, ijkl \rangle \, x_{\mathrm{ch.}}^i \, \theta_{\mathrm{ch.}}^j \, y_{\mathrm{ch.}}^k \, \phi_{\mathrm{ch.}}^l \qquad (4.20)$$

$$y = \sum_{i,j,k,l} \langle y \,|\, ijkl \rangle \, x_{\mathrm{ch.}}^i \, \theta_{\mathrm{ch.}}^j \, y_{\mathrm{ch.}}^k \, \phi_{\mathrm{ch.}}^l \qquad (4.21)$$

$$\Phi = \sum_{i,j,k,l} \langle \Phi \,|\, ijkl \rangle \, x_{\mathrm{ch.}}^i \, \theta_{\mathrm{ch.}}^j \, y_{\mathrm{ch.}}^k \, \phi_{\mathrm{ch.}}^l \qquad (4.22)$$

The OOPS spectrometers, which focus in only the momentum-dispersive x-direction, is unable to resolve y at the target. The OOPS optics simply assume a point vertex; the y matrix elements $\langle y \,|\, ijkl \rangle$ are all therefore set identically to zero.

The matrix elements themselves were determined in the commissioning phase of the experiment, during a series of extensive optical studies wherein sieve slit collimators are installed at the spectrometer entrances, allowing only events with precisely determined values of the target coordinates to be recorded. The chamber coordinates measured corresponding to the known target coordinates are fit, and the matrix elements connecting them are determined by a fifth-order, polynomial chi-squared fit in four variables. The procedure has

62

been described in detail in the Ph.D. theses of Mandeville [37] and Kunz [34].

Optical Resolution

The optics also have finite resolution. The combined optical and wire chamber resolution are estimated in Monte-Carlo simulation by generating a large number of events with known target coordinates, transporting them through the spectrometer models and obtaining a set of chamber coordinates for each event. Random Gaussian-distributed errors are added to the chamber coordinates at each layer, consistent with those determined for the actual chambers in equations 4.15 and 4.16. Tracks are then fit to the simulated chamber hits using the same procedure as for real data.

These pseudo-data chamber coordinates are then put through the optics transformation matrix to create reconstructed target coordinates, which may be compared to the original generated target coordinates. The resolution is taken as the width σ of the distribution of the differences between the generated and reconstructed value of each coordinate. We find for OOPS

$$\sigma_\delta = 0.64\% \tag{4.23}$$

$$\sigma_\theta = 0.45\text{mr} \tag{4.24}$$

$$\sigma_\phi = 0.83\text{mr} , \tag{4.25}$$

and for OHIPS

$$\sigma_\delta = 0.25\% \tag{4.26}$$

$$\sigma_\theta = 0.35\text{mr} \tag{4.27}$$

$$\sigma_\phi = 0.42\text{mr} \tag{4.28}$$

$$\tag{4.29}$$

These uncertainties are used in section 4.3.4 in evaluating the systematic errors in the coinci-

63

dence phase-space volume, which is determined largely by software cuts on the reconstructed

target coordinates.

4.2 Software Cuts

4.2.1 Particle Identification

Pion Arm

The polarity of the OOPS dipole magnets select only positive charged particles, by bending their trajectories upward toward the detector package. In addition to the π^+ mesons that we wish to detect, OOPS will also record any other positive charged particles of the correct momentum. These are background signals, which must be removed from the analysis. In the energy range of this experiment, protons are the only significant candidate for backgrounds; positrons fall below the threshold of our phototubes, which were set for π^+ detection.

The pion and proton signals in the scintillators form distinct peaks. The left hand panel of figure 4-10 shows the particle energy loss in the first and second layer scintillators; the π^+ peak is sharp and rather cleanly separated from the broad proton distribution. Software cuts are applied about the π^+ peak; the approach used is to make the cuts rather loose so that pions at the extrema of the distribution are not inadvertently cut out; protons in the low energy tail which are left in at this stage will be removed later by the cuts on the Time-of-Flight spectrum (section4.2.2), as well as by cuts on the Missing Mass spectrum and by background subtraction (sec. 4.2.3).

Electron Arm

The OHIPS dipole magnet similarly selects only negative charged particles. In the energy range of this experiment, negative pions are the only source of this background. These can only be produced by the reaction $\gamma^* n \to \pi^- p$ on neutrons in the target cell wall, or other material hit by the beam, since the liquid hydrogen target contains virtually no neutrons. Therefore, the number of backgrounds seen in OHIPS is greatly reduced compared to those seen in the the pion arm spectrometers, and in actual practice the time of flight cuts and background subtraction procedures are sufficient to reduce pion backgrounds to insignificant levels; because of this no additional software cut for PID is used on the OHIPS side.
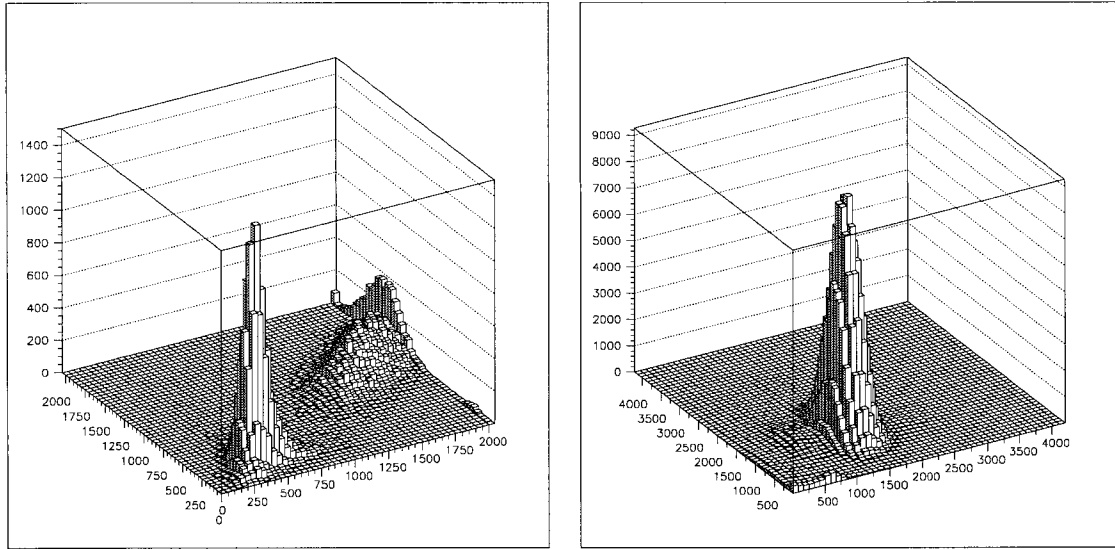
Figure 4-10: Particle Identification Left: Energy deposit in the OOPS first versus second layer scintillators is shown in arbitrary units. The sharp peak near the origin are π^+ events, while protons form the broader distribution at higher energy. The clear separation between the two features permits clean particle identification cuts. Right: The OHIPS Čerenkov vs. lead-glass spectrum shows a strong electron peak, with negligible contamination

4.2.2 Time of Flight

The coincidence Time of Flight (ToF) is defined by the time difference between the OOPS second layer scintillators and the OHIPS trigger. True coincidence events form a narrow peak in the time of flight spectrum, sitting on top of an approximately uniform background of random coincidence events which fill the entire coincidence gate. By cutting on the time of flight spectrum, these unwanted background events can be removed from the analysis.

Often the raw Time of Flight spectrum must be corrected to account for timing fluctuations due to variations in particle velocity of path length through the spectrometer. These timing fluctuations cause a broadening to the true coincidence peak and can significantly degrade the signal-to-noise ratio. This can be appreciable, particularly for proton detection where velocity variations due to the momentum distribution within the spectrometer acceptance can be large.

For pion detection however, the relatively small mass means there is little variation in velocity — on the order of 1–2% — across the 10% momentum bite of OOPS. Timing

66

fluctuations due to pathlength or velocity differences are kept to negligible levels, and the raw time of flight signals produce sufficiently sharp peaks, with good signal to noise ratios, in all OOPS coincidences such that corrections to the time of flight spectrum are unnecessary. A typical Time of flight spectrum is shown in figure 4-11. Typical Full Width at Half-Maximum (FWHM) values are $\sim 3.4 - 3.5$ ns.
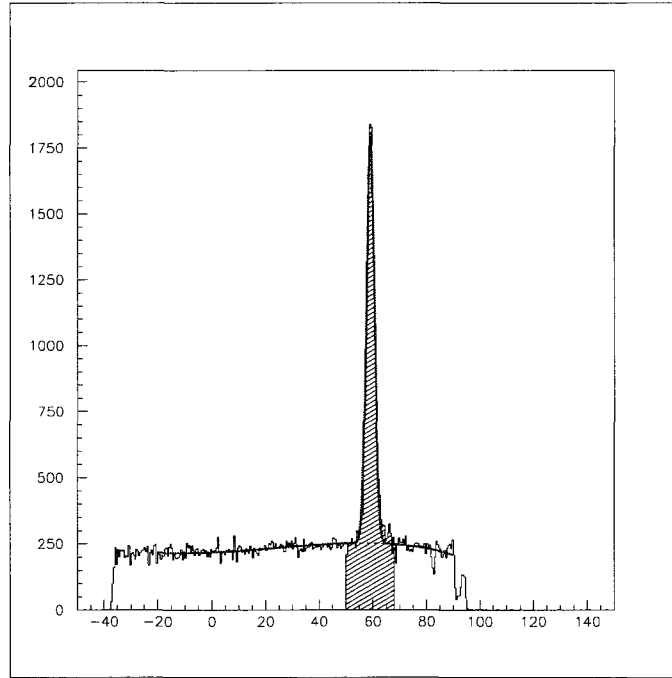
Figure 4-11: A typical OOPS time of flight spectrum shows a sharp coincidence peak on top of a background of accidental coincidences. The peak-region software cut is shown by the shaded region. A Gaussian function plus polynomial background has been fit to the spectrum in order to estimate backgrounds inside the cut (red curve).

The Time of Flight Cut

The coincidence peak and background are both fit with a Gaussian-plus-polynomial function within a broad region around the peak , as shown in figure 4-11. A software cut on the time of flight spectrum is used to eliminate the vast majority of the background events from the analysis.

The Time-of-Flight cut divides the spectrum into two regions. Within the cut (shaded area), the Peak Region contains a number N_p of events, equal to the number of true coin-

67

cidence events N_t in the peak itself plus some number N_{bg} of background events which also happen to fall within the cut:

$$N_p = N_t + N_{bg}.$$ (4.30)

Outside of the cut, the Accidental Region contains N_{ac} accidental coincidence events which randomly occupy the time of flight window.

The numbers N_p and N_{ac} are obtained directly by summing the ToF histogram over the respective regions. The number N_{bg} of backgrounds in the peak region is estimated by integrating the polynomial terms of the fit function, shown above, between the limits of the software cut values. The number of true coincidence events in the peak itself is then estimated as

$$N_t = N_p - N_{bg}.$$ (4.31)

The width of the peak region is at least $\pm 3\sigma$ ($\approx \pm 5.5$ ns) to avoid cutting out true coincidence events, but in some cases a wider cut is used. For example, if the ToF peak exhibits some tailing which is not well modeled by a Gaussian distribution, defining a wider peak region prevents cutting out good events. Because peak-region backgrounds are subtracted in all cases, the resulting value of N_t is insensitive to the precise placement of the cuts.

Table 4.1 lists numbers of counts in the ToF peak and accidental regions along with estimated background, and true coincidence counts for all spectrometers in both kinematic settings. Other than PID cuts on the scintillator ADC outputs, no cuts have been applied to the spectra.

4.2.3 Missing Mass Cut

Proper reconstruction of the "missing" mass of the undetected neutron, $m_n = 939.57$ MeV, provides the most stringent test of good coincidence events. The missing mass is recon-

OOPS:	Kinematics A			Kinematics B		
	A	B	C	A	B	C
N_{pk}	11,589	15,301	12,442	18,221	22,613	21,020
N_{ac}	19,694	74,135	42,532	34,140	56,058	50,635
N_{bg}	4,921.37	7,534.66	4,662.25	7,572.24	10,649.8	8,867.2
N_{t}	7,297.63	7,766.34	7,779.75	10,684.8	11,963.2	12,152.8

Table 4.1: Time-of-Flight peak data for three OOPS modules in two kinematic settings. The numbers of peak region, accidental, estimated background, and true coincidence counts are listed.

structed from the measured momenta of the detected particles,

$$m_{\mathrm{miss}} = \sqrt{W^2 + m_\pi^2 - 2W E_\pi^*}\,, \tag{4.32}$$

where E_π^* is the pion energy in the CM frame.
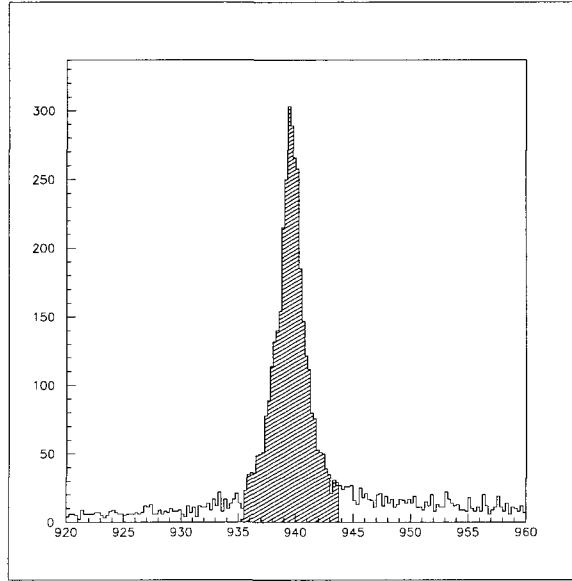
Figure 4-12: Typical OOPS missing mass distribution. The shaded region shows the 3σ missing mass cut about the peak. The peak centroid is at 939.52 MeV, in excellent agreement with the standard value of the neutron mass $m_n = 939.57$ MeV. A radiative tail extends the distribution, on the right, toward higher missing mass values. The events to the left of the peak are due to background contamination

A typical OOPS missing mass spectrum is shown in figure 4-12. Particle Identification cuts and Time-of-Flight cuts, as well as acceptance cuts on the reconstructed target vari-

69

ables (see section 4.3.2) have been applied. The shaded region shows the placement of the missing mass cut at $\pm 3\sigma$ (± 4.0 MeV) around the peak centroid to select good $p(e, e'\pi^+)n$ coincidence events. The tally of counts N within this peak region is the raw number of detected events, used in the calculation of cross sections in chapter 5.

However, this tally still contains a small number of random background events. These may include protons which survived the PID cuts as well as pions detected by OOPS in accidental coincidence with unrelated electrons in OHIPS. A Time-of-Flight background subtraction procedure allows the calculation of a background-reduction scale factor f_{bg}, described below, which accounts for this contamination in the final cross section calculation.

Good events in the radiative tail which are lost due to the missing mass cut are accounted for by the radiative correction factor η_{rad}, described in section 4.4.2.

Background Subtraction

The amount of background contamination in the missing mass histogram is estimated from the missing mass distribution of accidental coincidence events. We consider now the time-of flight distribution of only of the subset of events which have successful missing mass reconstruction; this is shown in figure 4-13. Note that the accidental background is significantly lower in this figure than in figure 4-11. This is primarily because accidentals have poorer reconstruction efficiency than true pions. The same procedure for determining peak, accidental, true and background events in the ToF spectrum as described above in section 4.2.2 is followed again. These are now labeled as N'_p, N'_{ac}, N'_{bg}, and N'_t, where the prime is used to distinguish that these counts are for only the missing-mass-reconstructed subset of events.

The distribution in missing mass of events from the different regions in the ToF spectrum now allow the estimation of the background in the missing mass peak. The missing mass peak itself, cut to show only events also from the peak region of the ToF spectrum, is shown in the upper left panel of figure 4-14; we denote the number of events in this histogram as M_p.

70
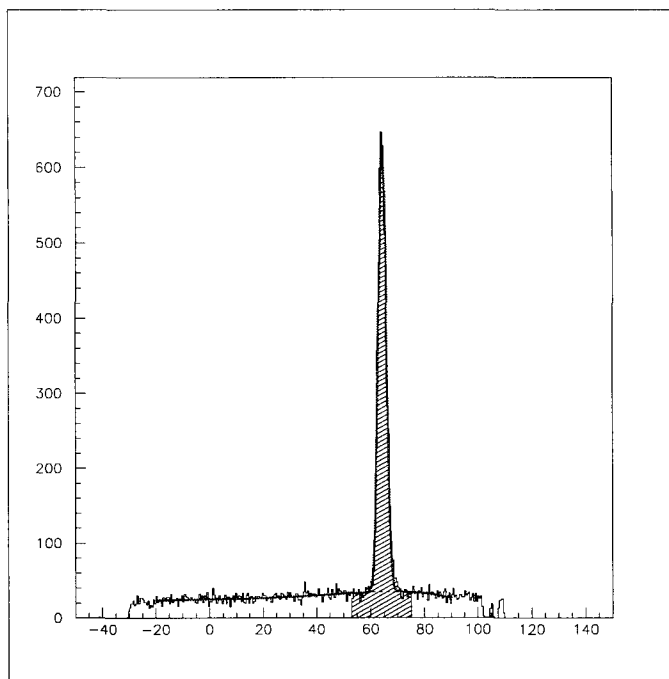
Figure 4-13: Time-of-Flight distribution of events with reconstructed missing mass. A Gaussian function plus polynomial background has been fit to the spectrum in order to estimate backgrounds inside the cut (red curve). The number of events has been greatly reduced by acceptance cuts and reconstruction inefficiency.

The distribution of accidental ToF events in the missing mass peak, obtained by inverting the ToF cuts, is shown in the upper right. This number we call M_{ac}.

To simulate the distribution of background events in the histogram of ToF-peak events, the histogram of accidental events is scaled channel-by-channel by the ratio of background to accidental events as calculated from time of flight distribution. The total number of backgrounds in the missing mass peak is then

$$M_{bg} = M_{ac} \times \frac{N'_{bg}}{N'_{ac}}. \tag{4.33}$$

This simulated background distribution is shown overlaying the ToF peak-region histogram in the lower left.

The bib-by-bin subtraction of the two histograms is plotted on the lower right; this is the background-subtracted missing mass peak; it contains a number M_{true} of events given

71
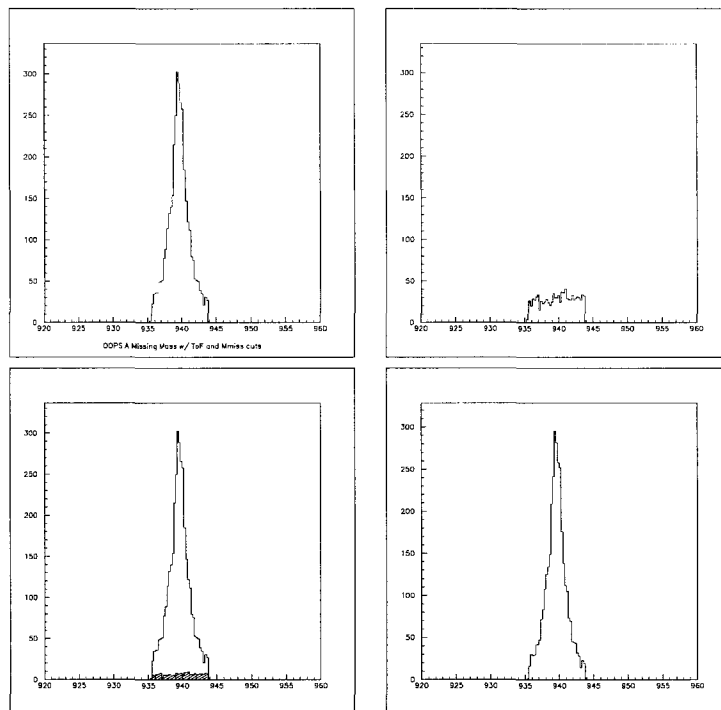
Figure 4-14: Missing mass peak background subtraction. Upper left: A typical OOPS missing mass peak, with cut for ToF peak region. Upper right: The OOPS missing mass peak for accidentals, outside the ToF peak region. Lower left: ToF peak-region missing mass peak with scaled background superimposed. Lower right: Missing mass peak with scaled backgrounds subtracted.

by

$$M_{\text{true}} = M_{\text{p}} - M_{\text{bg}}. \tag{4.34}$$

This background-subtracted number of events is not used directly in the calculation, however, because the number of counts still has to be corrected on an event-by-event basis for finite acceptance effects (see section ??), and the background subtraction procedure does not preserve the identity of individual events. Instead, we define a background-reduction scale factor $f_{\text{bg}} = \frac{M_{\text{true}}}{M_{\text{p}}}$ to correct the final cross section results for background contamination. The correction factors obtained for each spectrometer are listed in table 4.2.

72

	Background correction factor f_{bg}		
	OOPS A	OOPS B	OOPS C
Kin. A	0.949 ± 0.004	0.925 ± 0.005	0.929 ± 0.005
Kin. B	0.933 ± 0.004	0.914 ± 0.004	$.912 \pm 0.005$

Table 4.2: Time-of-Flight peak data for three OOPS modules in two kinematic settings. The numbers of peak region, accidental, estimated background, and true coincidence counts are listed.

4.3 Monte Carlo Simulation

4.3.1 AEEXB

The Monte Carlo program AEEXB [41] was used to model the experimental setup for the tasks of calculating coincidence phase-space acceptance volumes, as well as determining the placement of software acceptance cuts to minimize model errors introduced by the finite phase-space correction described in section 4.4.4.

AEEXB allows the user to accurately place highly detailed models of the OOPS and OHIPS spectrometers about the target in three dimensions, reproducing the geometrical layout of the physical experiment. An event generator simulates random coincidence events into user defined acceptance limits, constrained by the kinematics of the desired $A(e, e'x)B$ reaction. The event generation can be done uniformly over the phase-space, or weighted by any of a number of cross section models.

Following event generation, AEEXB propagates the particles through the target, applying multiple scattering and ionization energy loss effects to each event.

The ray-tracing program TURTLE[1] [42] is integrated into AEEXB to calculate particle trajectories through detailed spectrometer models. Particle kinematics are saved at a number of detector "cards" placed throughout the TURTLE models, and exported into HBOOK files for analysis using Physics Analysis Workstation (PAW) [39] or ROOT [40].

4.3.2 Acceptance Cuts

In general, the Monte Carlo simulation models the OOPS-OHIPS coincidence phase-space acceptance to high accuracy. Acceptance cuts are applied identically to the data and simulation, in order to eliminate minor disagreement which can occur between the two due to fringe magnetic field effects and minor variations of the physical spectrometers from the engineering specifications, which are difficult to model but can effect the shapes of the the phase space volumes at the acceptance edges. The cuts used in each spectrometer are listed

---

[1]Tracing Unlimited Rays Through Lumped Elements

74

in table 4.3.

	Acceptance Cuts			
	OOPS A	OOPS B	OOPS C	OHIPS
δ	$\pm 10\%$	$\pm 10\%$	$\pm 10\%$	$-7\%, +6\%$
θ	± 30 mr	± 30 mr	± 30 mr	± 50 mr
ϕ	± 10 mr	± 10 mr	± 10 mr	± 10 mr

Table 4.3: Target variable acceptance cuts.

Comparisons of the data with AEEXB Monte-Carlo simulation are shown in figures 4-15 — 4-21. In all the one-dimensional plots, a scaled TOF background spectrum has been subtracted as described in section 4.2.3 so that only true coincidence events are shown. The simulated events are weighted by the MAID 2003 cross section. Shaded areas indicate the regions of the phase space accepted by the software cuts. In the OHIPS δp spectrum (fig. 4-15, upper left), note that the simulated spectrum over-estimates the limits of the phase space acceptance on the high momentum (right hand) side. This is well understood to be due to a physical repositioning of the OHIPS second layer wire chamber, during a recent refitting of the instrument package, in order to allow plumbing lines to pass through the spectrometer. This change in the internal configuration of the spectrometer is not reflected in the TURTLE model, so a software cut is used to simply remove the affected portion of the phase space from the analysis.

In all of the OOPS spectrometers, we see that the target ϕ coordinate agrees less well with Monte Carlo than do the other spectra. This is a resolution effect in the data, due to the frequent necessity of running with only two working wire chamber layers in the non-dispersive coordinate. Since the non-dispersive coordinates (y and ϕ) contribute minimally to the momentum reconstruction, trading some resolution in these coordinates in exchange for maximizing run time was seen as advantageous by the collaboration.

4.3.3 Model Cross Section Comparison with Data

In section 4.4.4, model cross section calculations across the coincidence acceptance are used to estimate the effects of the finite acceptance on the measured cross sections. In order for this estimate to be valid, the models must accurately predict the relative shape of the cross section over the full range of phase space to be used. While the models cannot be assumed to correctly calculate the *magnitude* of the cross section, it is required that they reasonably predict the derivatives of the cross section in the kinematic variables W, Q^2, $\theta^*_{\pi q}$ and $\phi_{\pi q}$.

To demonstrate that this is indeed the case, within the acceptance cuts, MAID2003-weighted Monte-Carlo is compared with data after applying the cuts to both. After the standard TOF background subtraction is applied to the data, the Monte Carlo histograms are normalized to the data by total numbers of events and it is observed that the shapes of the histograms are in excellent agreement between the two, for all kinematic variables. These are shown in figures 4-22 — 4-26. The lower panel in each figure shows the bin-by-bin ratio of the data to Monte Carlo, which is seen to be consistent with unity across the acceptance in all cases.

4.3.4 Coincidence Phase Space Volume

The coincidence phase-space is five-fold differential in the electron and pion solid angles and the energy acceptance of the electron arm:

$$\Delta\Omega = \Delta\Omega_e \Delta\Omega_\pi \Delta E'$$ (4.35)

The volume is determined individually in AEEXB simulation for each OOPS module, by generating a number $N_{\text{tot.}}$ of white-spectrum (randomly distributed and un-weighted by any cross section) coincidence events.

Each event consists of an electron and positive pion. The electron is generated randomly into a 60 hr $\times$ 125 hr box about the OHIPS entrance collimator, within a momentum bite of ± 48.84 MeV (9% of the central momentum setting of 542.62 MeV) which slightly exceeds

76

that of the actual spectrometer. The pion is then generated into a 50 mr × 90 mr box about the OOPS opening collimator, with momentum determined by the requirement that an undetected neutron is also produced in the reaction. These kinematic windows define the event generation phase space volume

$$\delta\Omega_{\text{gen.}} = 125 \times 60 \times 50 \times 90 \times 92.25 \text{MeV} \cdot \text{Sr}^2 \tag{4.36}$$

$$= 3.297 \times 10^{-3} \text{MeV} \cdot \text{Sr}^2 . \tag{4.37}$$

The electrons and pions are tracked through the spectrometer the number of events in which both particles successfully reach the final scintillator layer at the back of the detector package is recorded as the number of detected events, $N_{\text{det.}}$.

The coincidence acceptance volume is defined as the ratio of the number of detected events to the number of generated events, times the generating volume:

$$\Delta\Omega = \frac{N_{\text{det}}}{N_{\text{gen}}} \delta\Omega_{\text{gen}} \tag{4.38}$$

The phase space volumes determined for each OOPS are listed in table 4.4. A systematic uncertainty of approximately 2.7% is assigned to each phase-space volume, which is also determined by Monte Carlo. Because the phase-space volumes are defined by the software acceptance cuts, the major contribution to errors in determining the phase space volume arises from the accuracy to which the acceptance cuts are placed. This is limited by the resolution of the spectrometer at the target, which is discussed in section 4.1.7.

Coincidence Phase-Space Volume $\Delta\Omega$		
OOPS	Kin. A	Kin. B
A	3.23	3.23
B	2.74	2.96
C	2.78	2.20

Table 4.4: Coincidence phase space volumes, determined in AEEXB Monte Carlo simulation for each OOPS in coincidence with OHIPS. Values listed are in units of 10^{-4}MeV Sr^2.

To determine the effect of the resolution uncertainty on the phase space volume, each cut is varied independently in turn by the amount of the uncertainty; the change resulting in the calculated phase space volume for each variation is noted. The effects of all variations are then added in quadrature, as the errors in all cuts should be independent quantities.
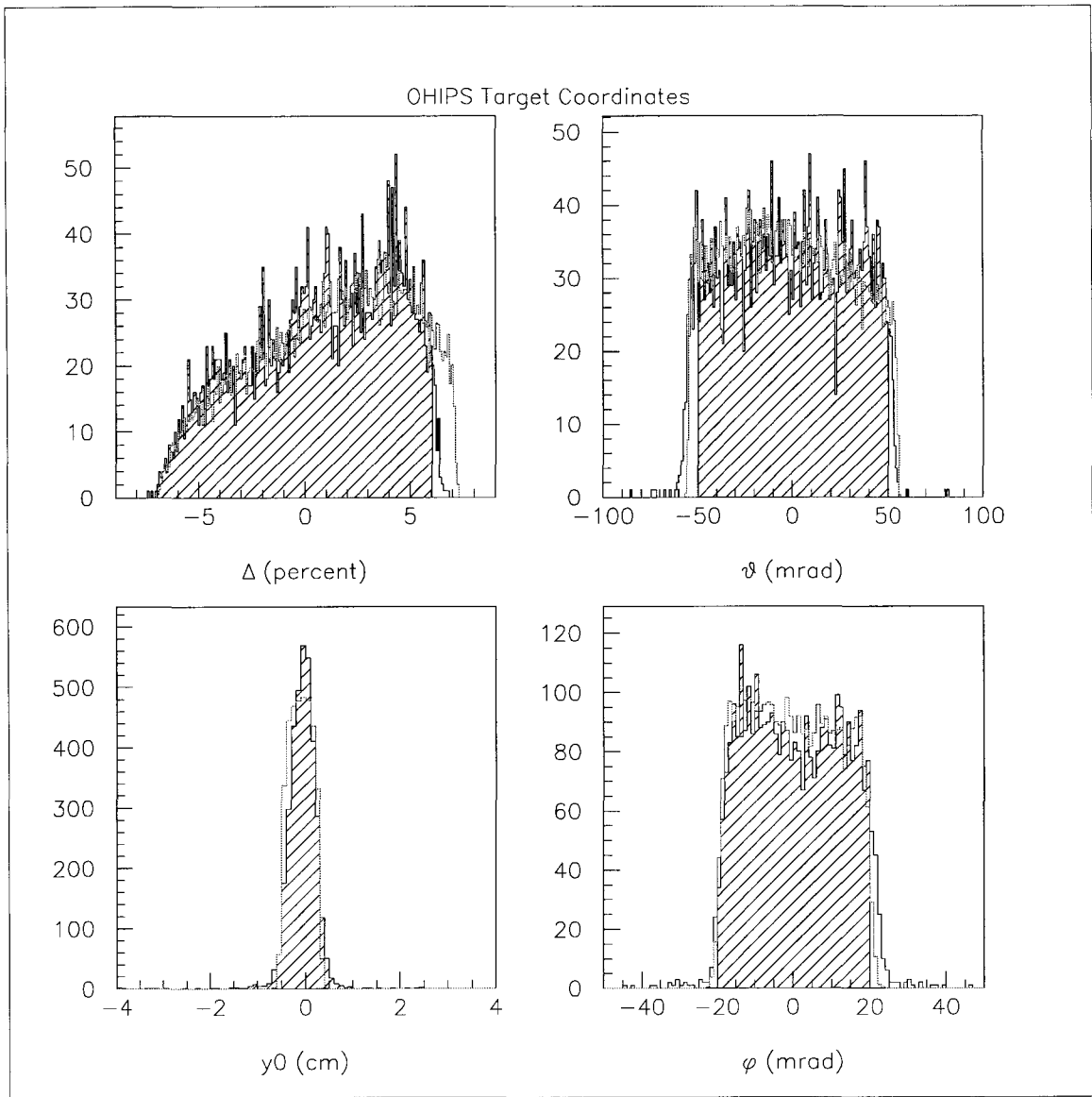
Figure 4-15: Comparison of data (black) and AEEXB Monte Carlo simulation (red) for OHIPS target coordinates.

79
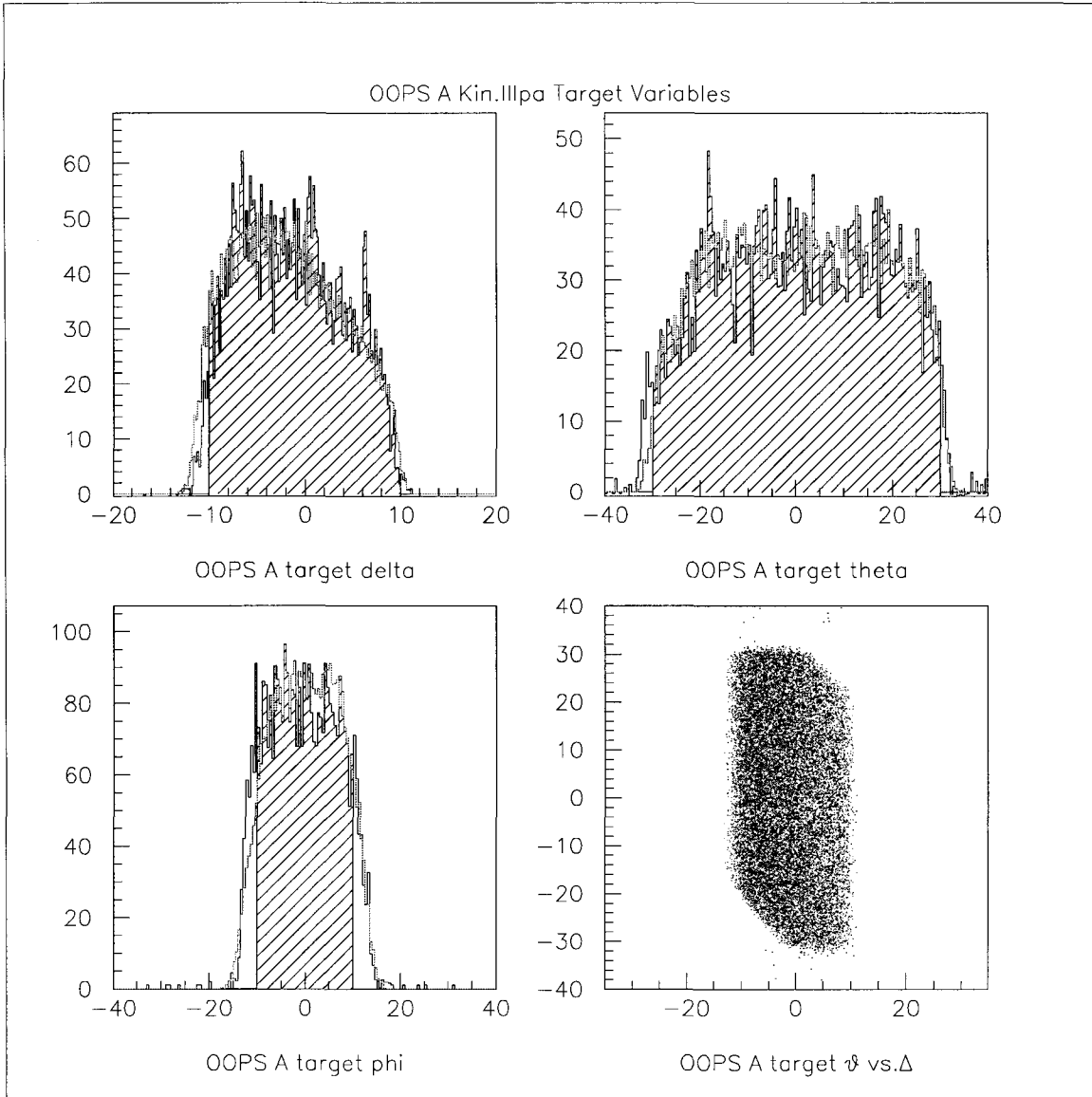
Figure 4-16: Comparison of data (black) and AEEXB Monte Carlo simulation (red) for OOPS A in Kinematics a ($\theta*_{\pi q} = 44.45°$, $\phi_{\pi q} = 180.0°$).

80
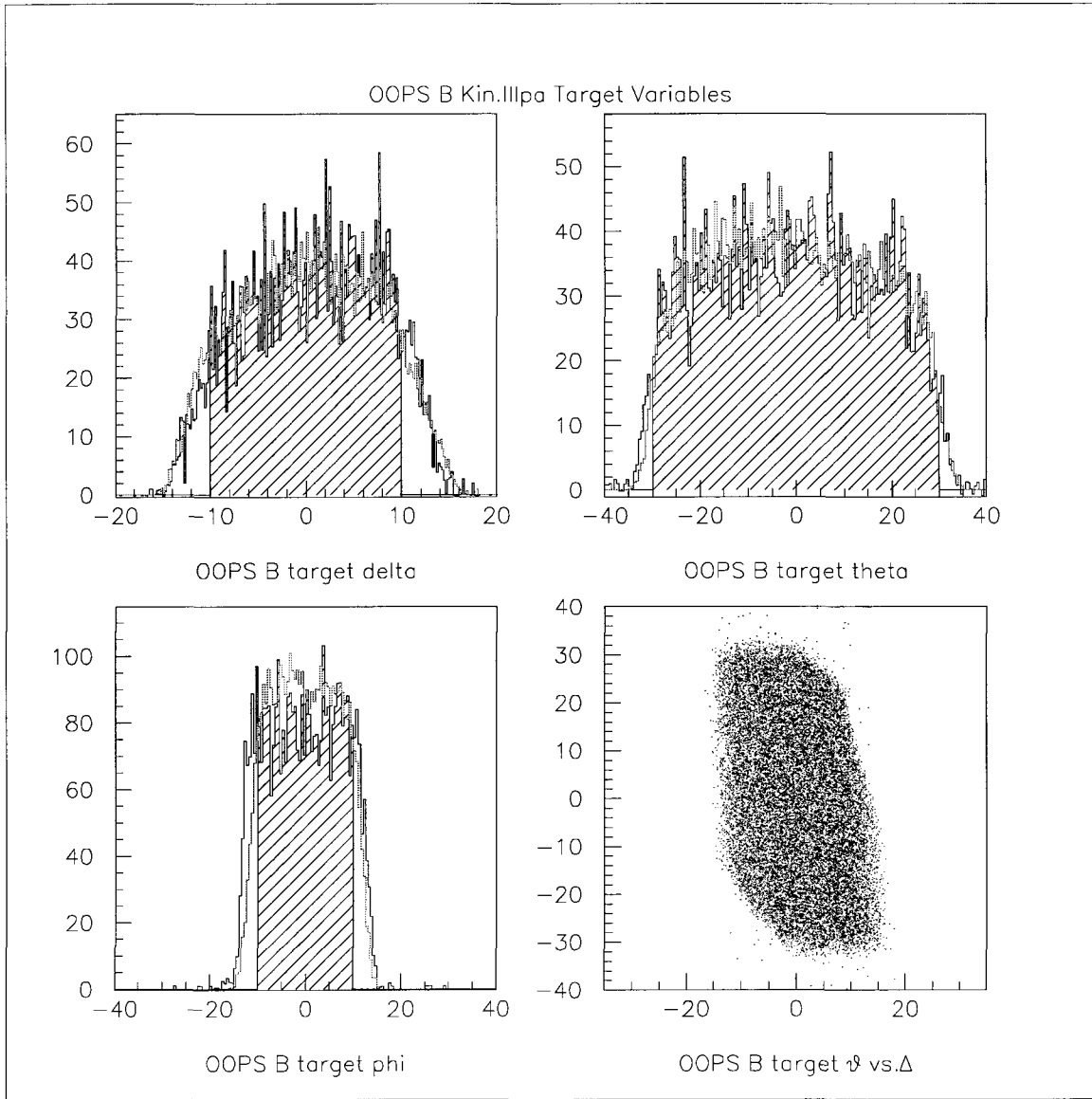
Figure 4-17: Comparison of data (black) and AEEXB Monte Carlo simulation (red) for OOPS B in Kinematics a ($\theta*_{\pi q} = 44.45°$, $\phi_{\pi q} = -60.0°$).

81
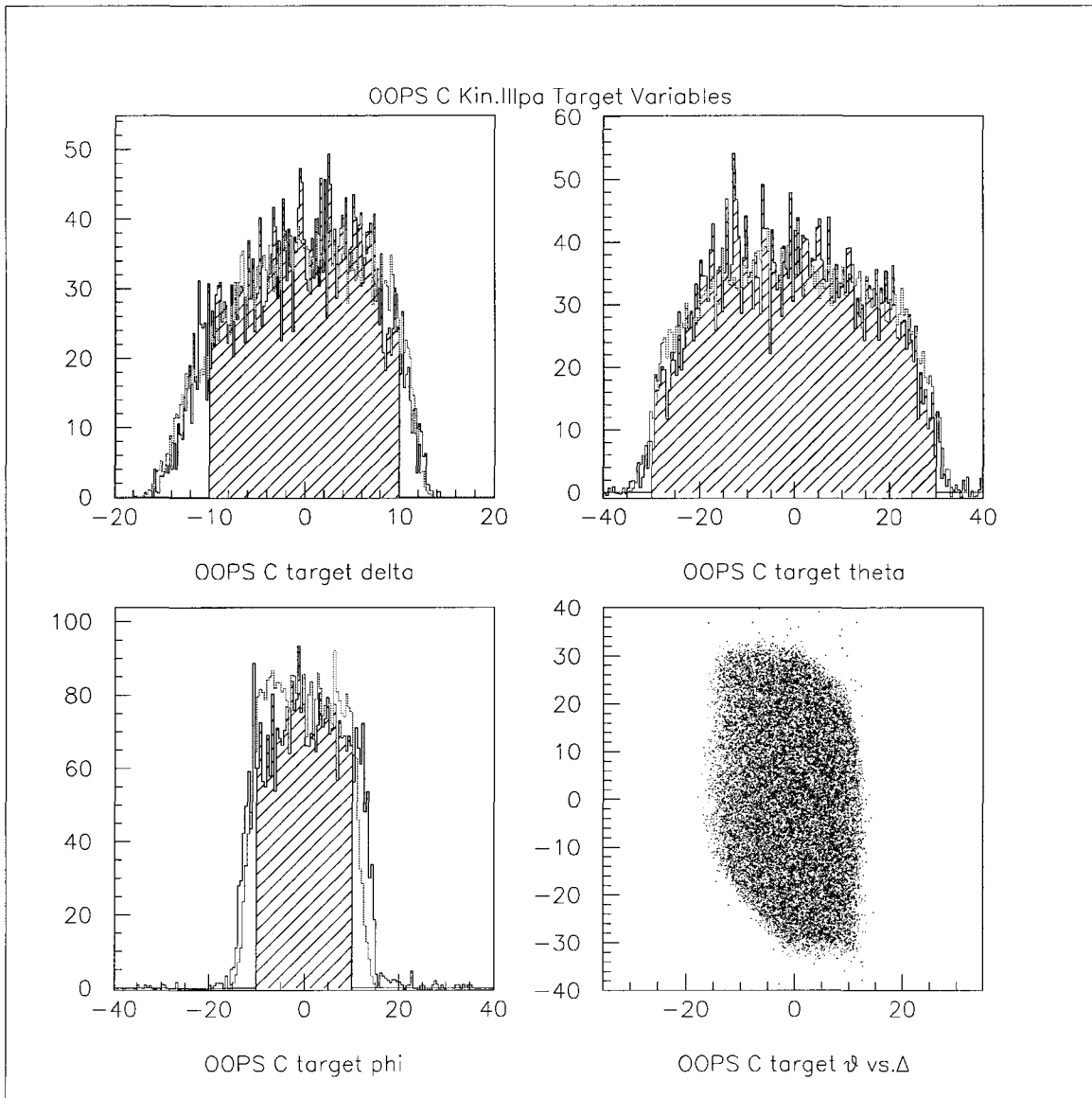
Figure 4-18: Comparison of data (black) and AEEXB Monte Carlo simulation (red) for OOPS C in Kinematics a ($\theta*_{\pi q} = 44.45°$, $\phi_{\pi q} = +60.0°$).

82
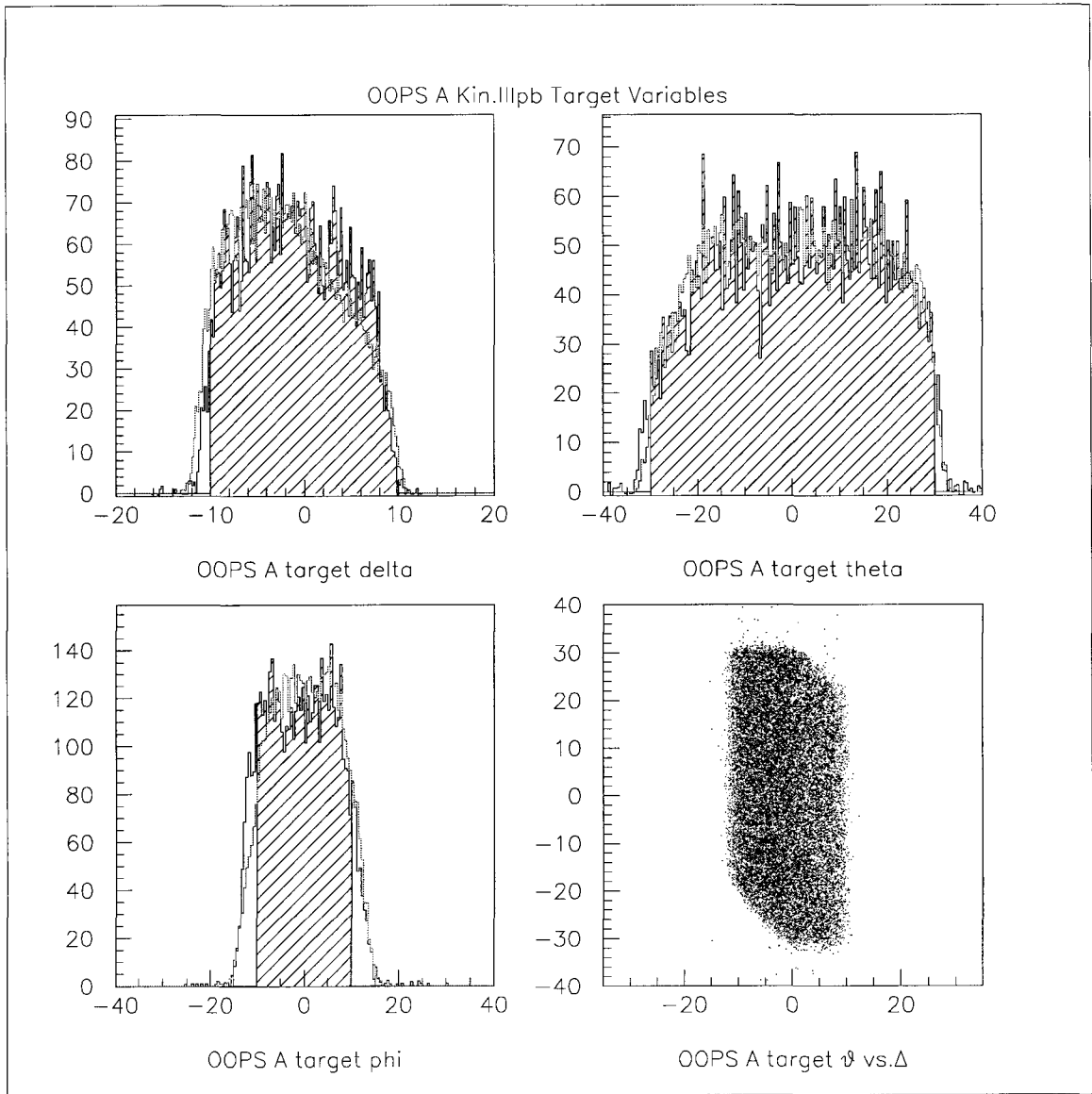
Figure 4-19: Comparison of data (black) and AEEXB Monte Carlo simulation (red) for OOPS A in Kinematics b ($\theta*_{\pi q} = 44.45°$, $\phi_{\pi q} = 180.0°$).

83
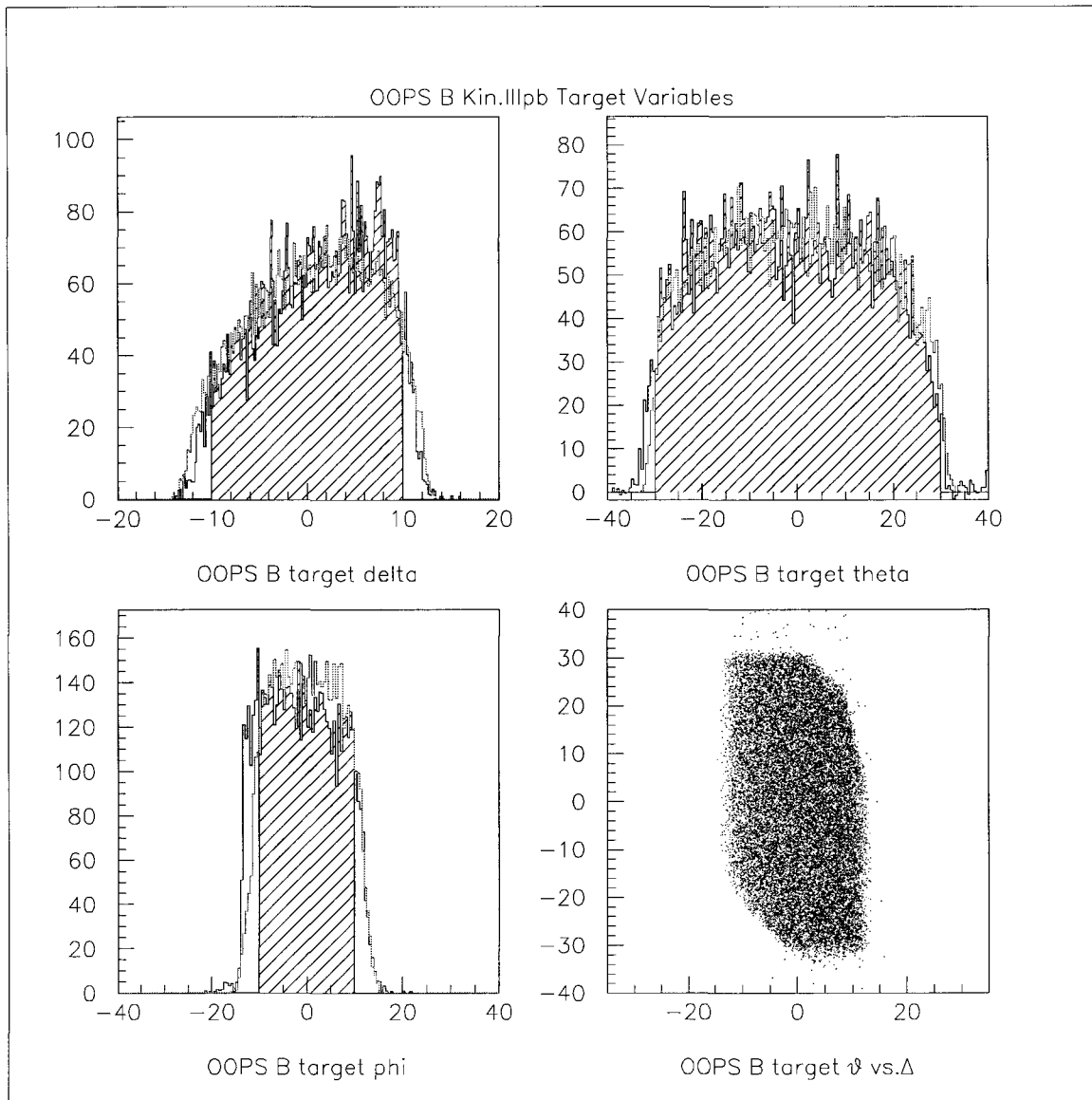
Figure 4-20: Comparison of data (black) and AEEXB Monte Carlo simulation (red) for OOPS B in Kinematics b ($\theta*_{\pi q} = 0°$).

84
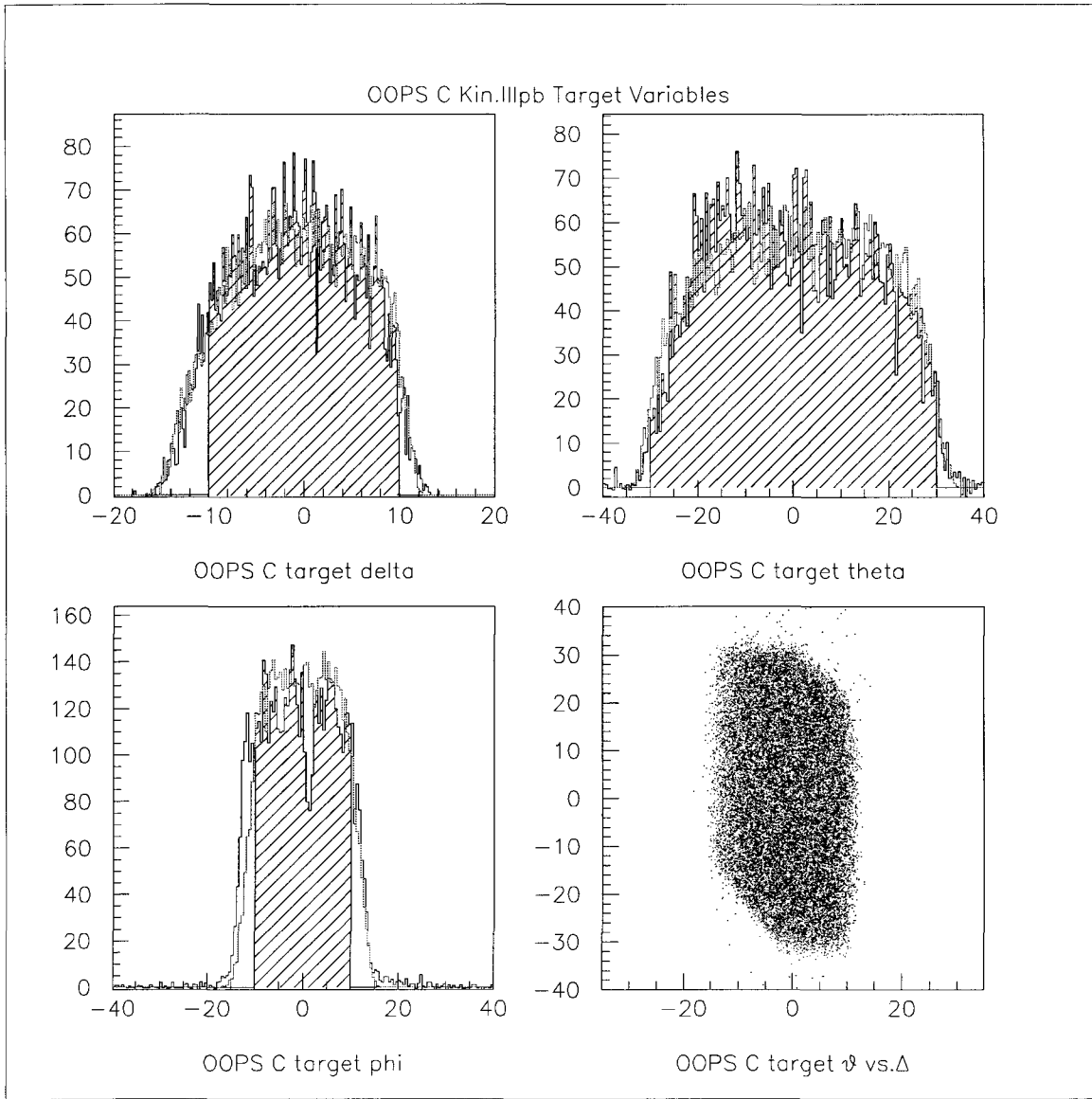
Figure 4-21: Comparison of data (black) and AEEXB Monte Carlo simulation (red) for OOPS C in Kinematics b ($\theta*_{\pi q} = 44.45°$, $\phi_{\pi q} = 90.0°$).

85
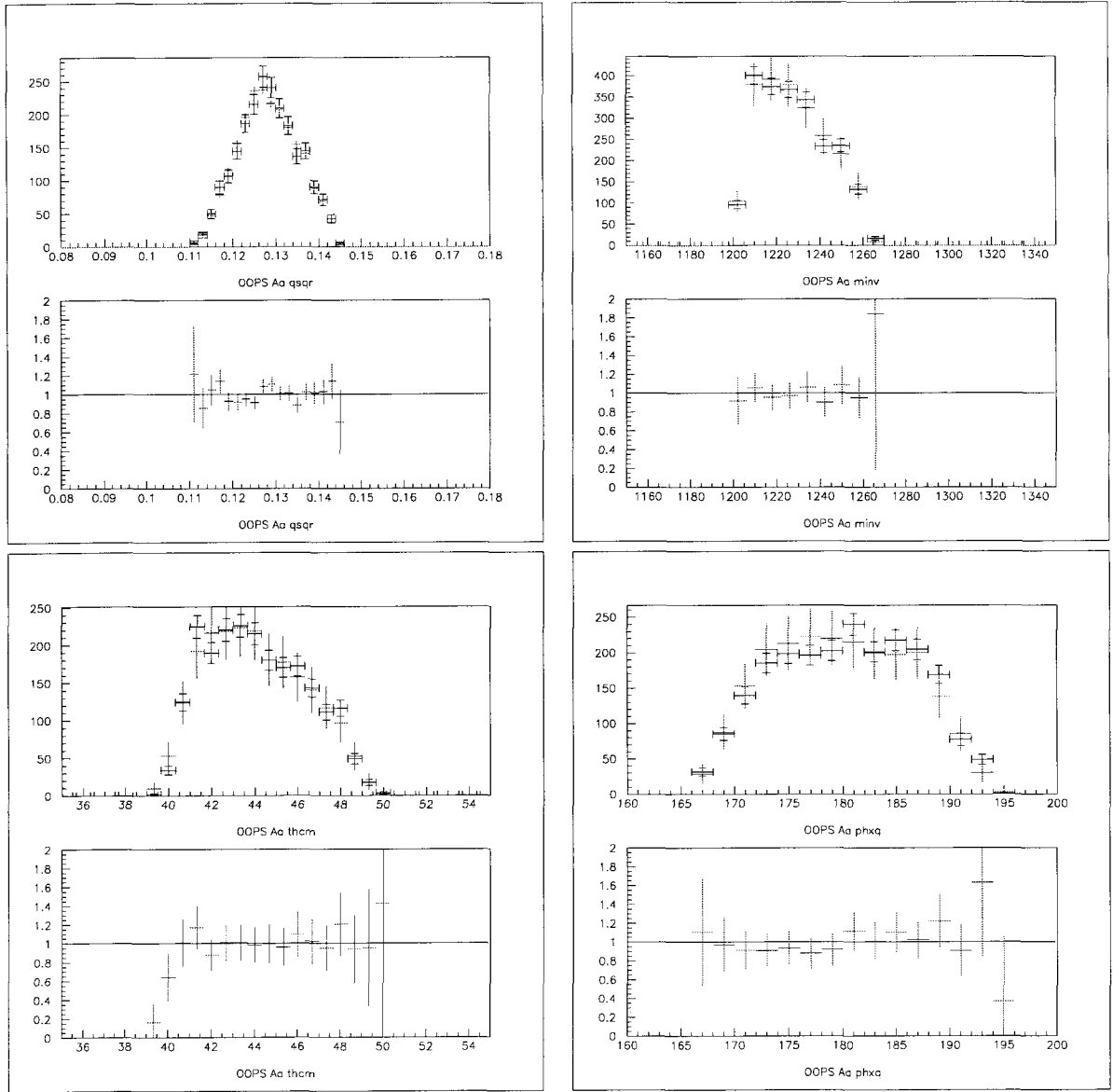
Figure 4-22: Comparison of MAID model cross section (red) in AEEXB simulation and data for OOPS A ($\theta^*_{\pi q} = 44.45°$, $\phi_{\pi q} = 180°$)

86
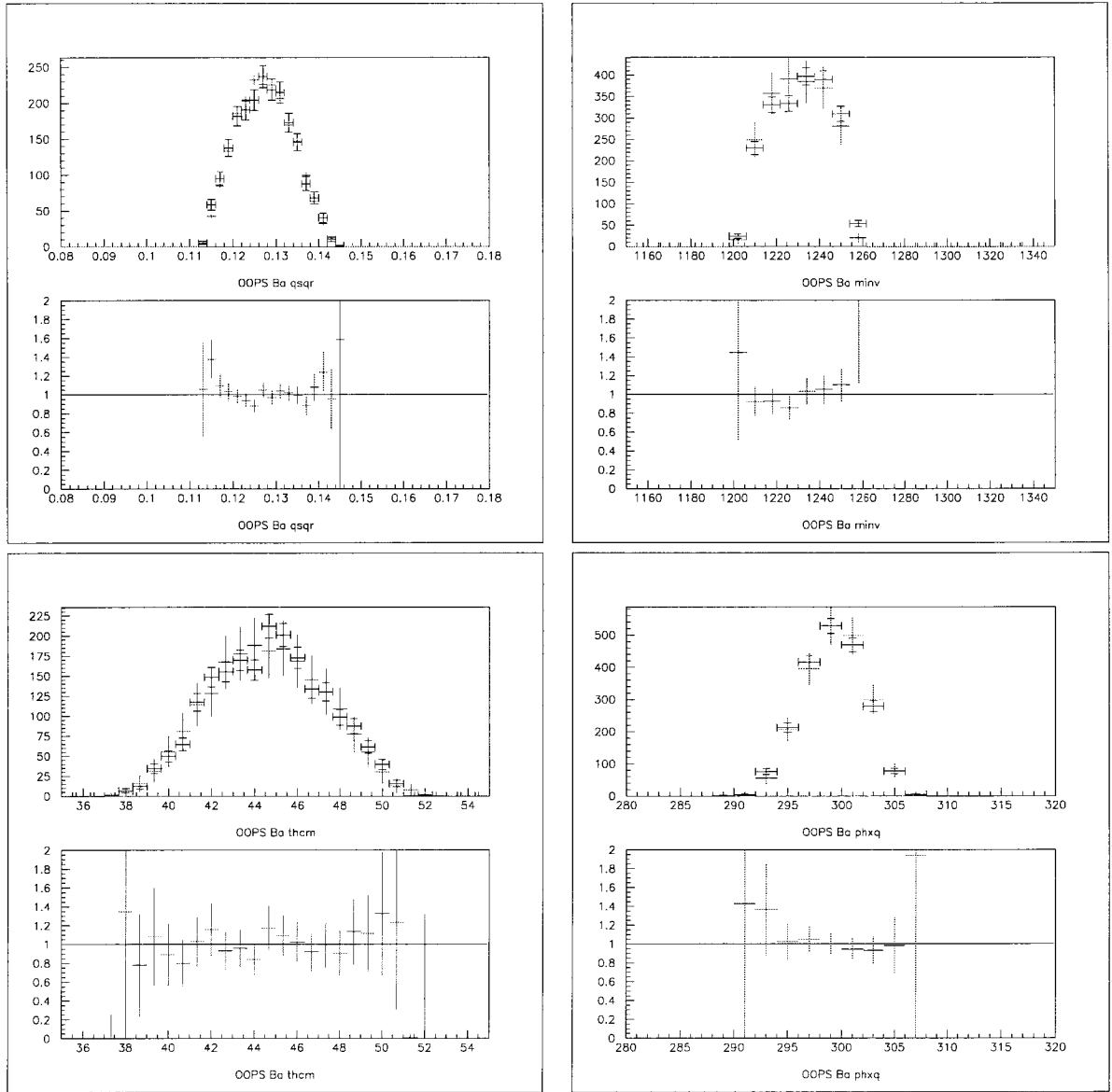
Figure 4-23: Comparison of MAID model cross section (red) in AEEXB simulation and data for OOPS B ($\theta^*_{\pi q} = 44.45°$, $\phi_{\pi q} = -60°$).

87
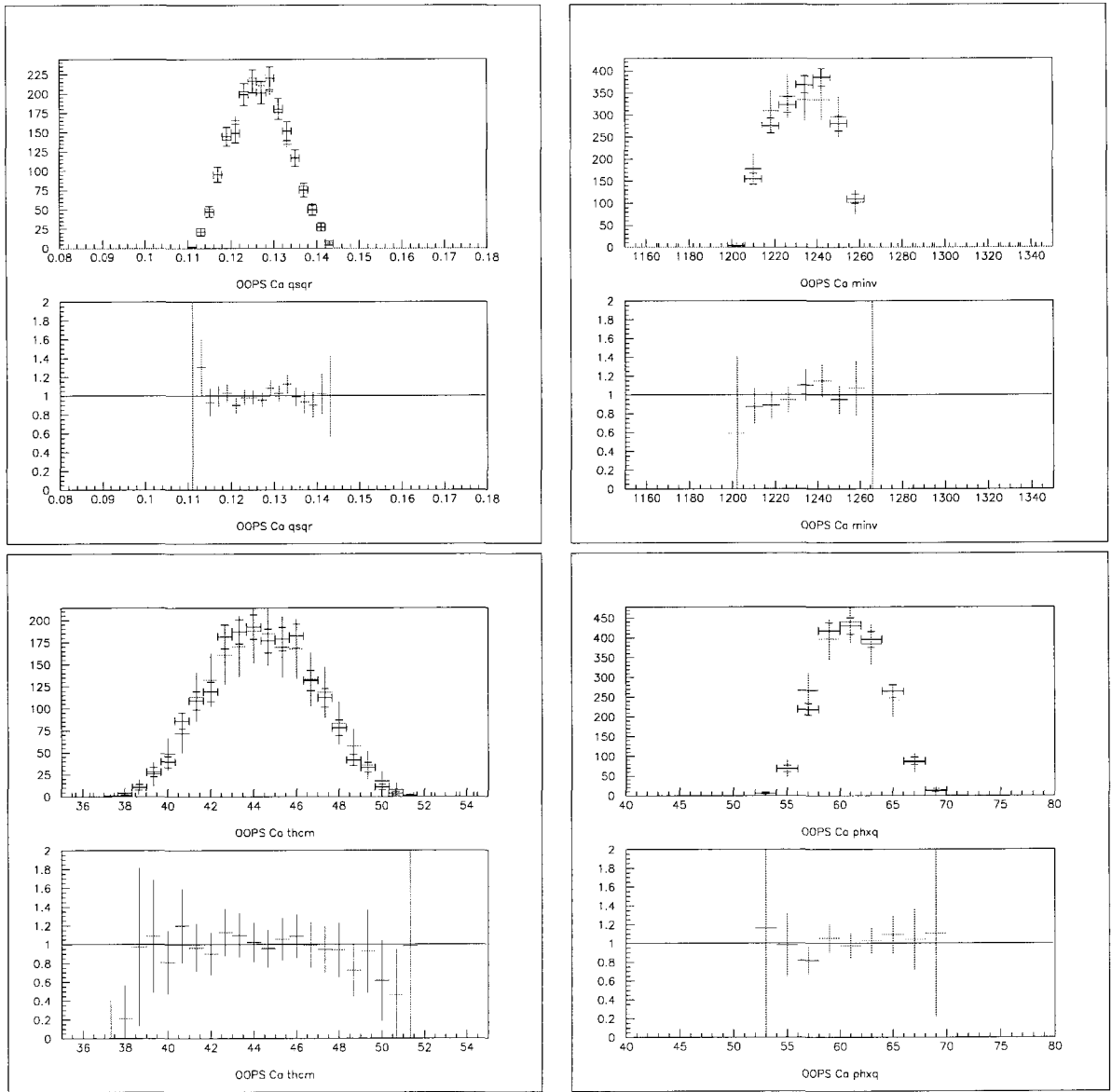
Figure 4-24: Comparison of MAID model cross section (red) in AEEXB simulation and data for OOPS C ($\theta^*_{\pi q} = 44.45°$, $\phi_{\pi q} = +60°$).

88
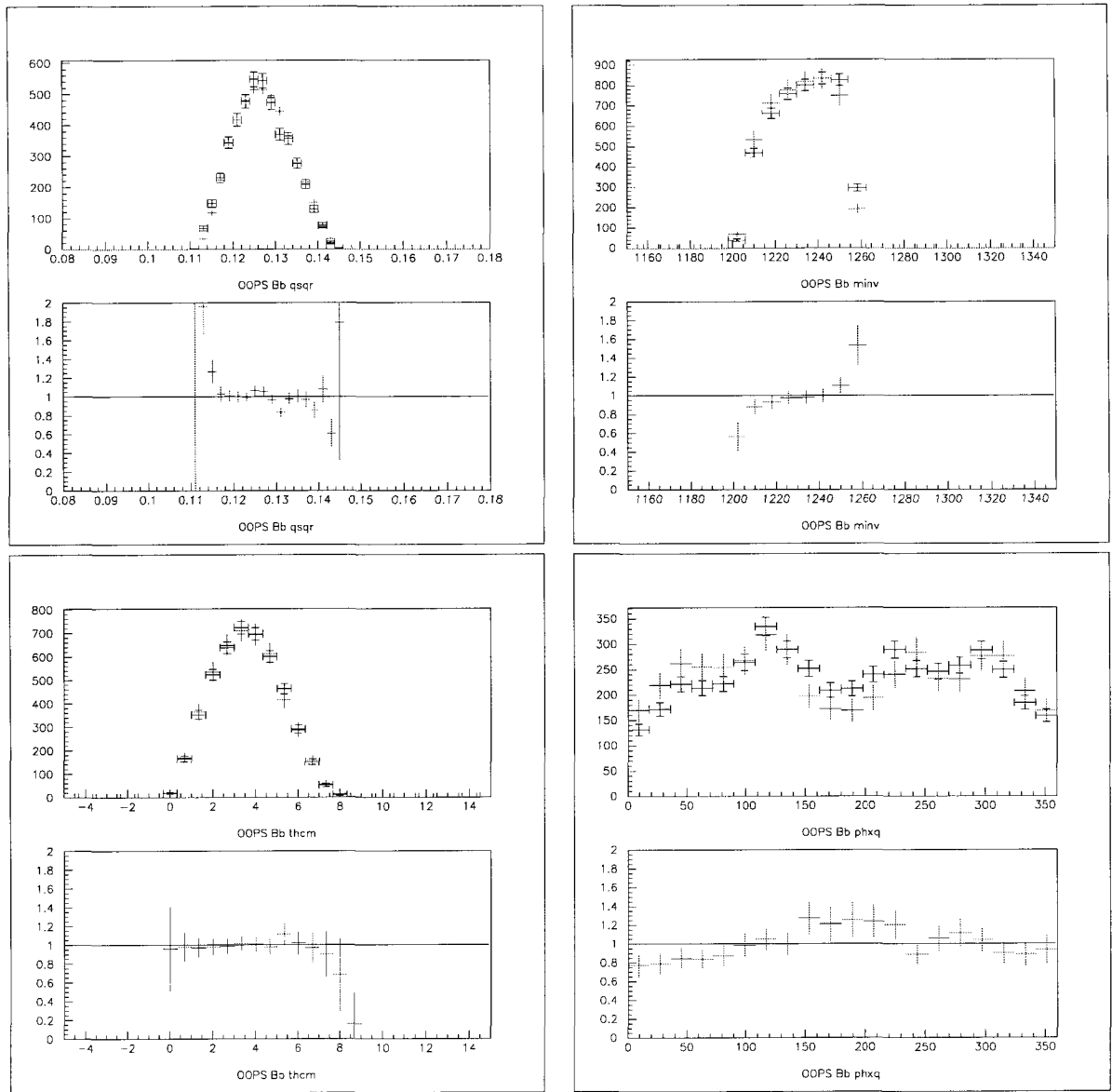
Figure 4-25: Comparison of MAID model cross section (red) in AEEXB simulation and data for OOPS B ($\theta^*_{\pi q} = 0°$).

89
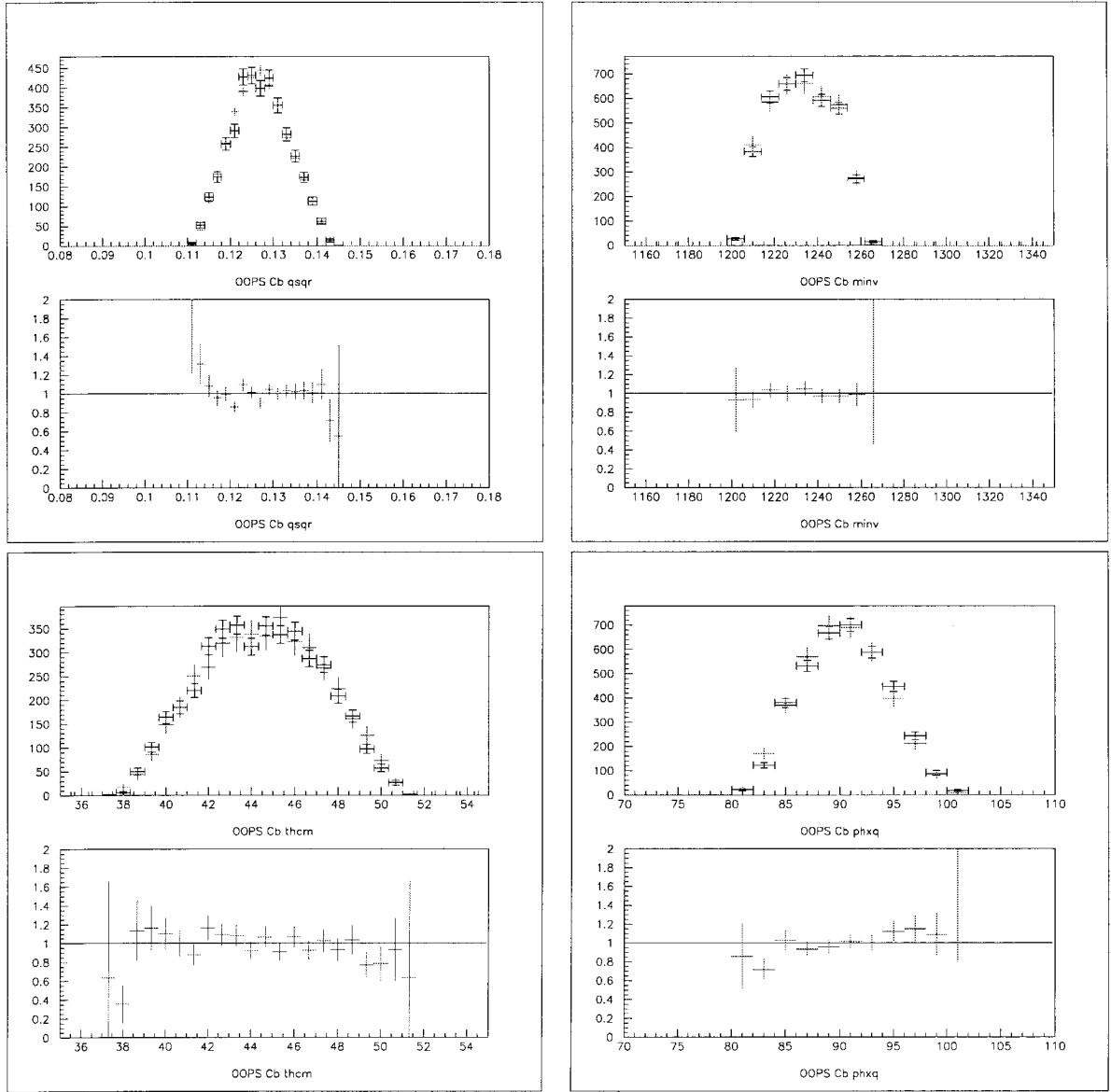
Figure 4-26: Comparison of MAID model cross section (red) in AEEXB simulation and data for OOPS C ($\theta^*_{\pi q} = 44.45°$, $\phi_{\pi q} = 90°$).

90

4.4 Correction Factors

4.4.1 Efficiency Corrections

OOPS and OHIPS Chamber Tracking Efficiencies

Not every particle that produces a trigger in the OOPS and OHIPS scintillators provides sufficient information at the wire chambers to allow successful track reconstruction. To produce a track in OOPS, a pion must trigger all three planes in the dispersive x-direction, and the resolution of the three hits must fall within the 3σ tracking resolution cut as described in section 4.1.5. In the non-dispersive y-direction, only two planes are required to fire, and so no y-resolution cut is used.

The chamber tracking efficiency is defined for OOPS as the ratio of the number of pions with good tracks to the total number of pion triggers at the scintillators,

$$\varepsilon_{\text{hdc}} = \frac{\text{Number of pions with good track}}{\text{Number of coincidence pion triggers}} \tag{4.39}$$

The number of pions with good tracks can be counted in any target or chamber histogram; The total number of pion triggers is counted in the time-of-flight spectrum. This allows one to cut on the pion timing peak and perform a background subtraction, as in section ??, to eliminate background events from the efficiency calculation in a way that is not dependent on any track reconstruction. Background events are contaminated with protons and do not have the same reconstruction efficiency as true coincidence pions.

The situation in the electron arm is analogous. The efficiency is

$$\varepsilon_{\text{vdc}} = \frac{\text{Number of electrons with good track}}{\text{Number of coincidence electron triggers}} \tag{4.40}$$

where again the number of good electron tracks is read from any OHIPS chamber or target histogram and the number of coincidence electrons is taken from the time of flight spectrum. On the electron side there is no significant difference in efficiency between true and background events, as virtually all triggers in OHIPS are due to electrons. The OHIPS

91

tracking efficiency is calculated separately for each kinematics.

The tracking efficiency correction factors are defined as

$$\eta_{\text{hdc}} = \frac{1}{\varepsilon_{\text{hdc}}} \tag{4.41}$$

$$\eta_{\text{vdc}} = \frac{1}{\varepsilon_{\text{vdc}}} \tag{4.42}$$

The tracking efficiencies obtained for OHIPS and each OOPS module are listed in table 4.5.

	OHIPS	OOPS A	OOPS B	OOPS C
Kin. A	1.19	1.12	1.14	1.19
Kin. B	1.16	1.10	1.08	1.16

Table 4.5: OOPS and OHIPS chamber tracking efficiency correction factors η_{hdc} and η_{vdc}.

Deadtime Correction

The data acquisition electronics veto circuits described in section 3.5.2 prevent the acquisition of new data while an event is already being processed. Good $N \rightarrow \Delta$ events that are missed due to this deadtime are accounted for with the deadtime correction factor η_{dt}.

The deadtime correction is calculated in terms of the OHIPS self-inhibit and the front-end computer-busy veto efficiencies. The OHIPS self inhibit efficiency is calculated as the number of raw OHIPS Pilot signals divided by the number of OHIPS triggers,

$$\varepsilon_{\text{s.i.}} = \frac{\text{Number of OHIPS pilot signals}}{\text{Total number of OHIPS triggers}} \tag{4.43}$$

and the coincidence computer busy efficiency is

$$\varepsilon_{\text{ccb}} = \frac{\text{Number of coincidences read out to the data stream}}{\text{Total number of coincidences from scalers}} \tag{4.44}$$

92

These are combined into an overall deadtime correction factor,

$$\eta_{\text{dt}} = \frac{1}{\varepsilon_{\text{s.i.}} \cdot \varepsilon_{\text{ccb}}} \tag{4.45}$$

The deadtime correction factors for each OOPS-OHIPS coincidence type are shown in table 4.6

	OOPS A	OOPS B	OOPS C
Kin. A	1.07	1.07	1.07
Kin. B	1.08	1.09	1.07

Table 4.6: Deadtime correction factors η_{dt} for each OOPS-OHIPS coincidence type.

93

4.4.2 Radiative Corrections

The experimental cross section is reduced by various radiative processes in which real or virtual photons are emitted by the electron. These include:

1. **Internal bremsstrahlung**, in which the electron interacts, via the exchange of one or more virtual photons, with the Coulomb field of the target nucleus either before or after the primary scattering interaction.

2. **External bremsstrahlung**, in which the electron interacts in a similar manner with nuclei other than the target nucleus itself.

3. **Landau straggling**, or ionization energy loss of the electron or pion passing through matter (e.g. the liquid target material and to a lesser extent the scattering chamber window or air)

Events undergoing such radiative processes have a larger missing energy than unradiated events, creating a tail in the missing energy and missing mass peaks.

Since these peaks already have a finite width due to the resolution limits of the spectrometers, the emission of low-energy photons by such processes only shifts the position of an event within the peak. The emission of higher energy photons can move an event outside of the missing mass cut which we use to identify true $H(e, e'\pi^+)n$ coincidence events. Figure 4-27 shows a typical OOPS missing energy spectrum, before and after the application of Missing Mass cuts.

The cross section must be corrected for the portion of otherwise good events which fall outside of the missing mass cuts due to radiation processes. For the simple case where we consider only the reduction of a single discreet peak this can be calculated very accurately, in principle.

Of the three radiative processes internal bremsstrahlung has by far the dominant effect, reducing the cross section by approximately 20%, and is the only process for which we calculate a correction. External bremsstrahlung is on the order of $< 1\%$ for the present
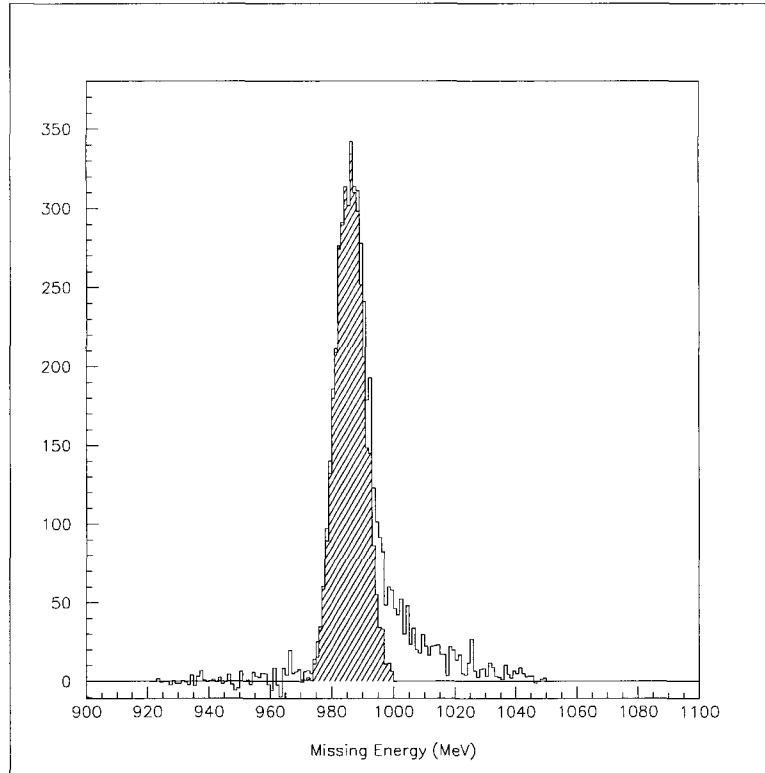
Figure 4-27: A typical OOPS missing energy spectrum. The shaded peak shows the portion of the spectrum that survives the Missing Mass cut. The un-cut spectrum exhibits a tail of radiated events with higher missing energy

experiment, and can be neglected. Landau straggling is dealt with by the inclusion of ionization effects in the COLA analyzer and AEEXB simulation software; no separate correction is necessary.

For the calculation of radiative corrections for internal bremsstrahlung, past analyses of pion electroproduction experiments have used the Schwinger correction, relying on the formulation of Mo and Tsai [43], and various extensions thereof (see for example Penner [44]).

This approach is actually inappropriate for coincidence electroproduction, however. The Schwinger correction is calculated expressedly for inclusive scattering, but exclusive scattering requires different handling in two important ways. First, in exclusive electroproduction the allowed phase space for the final radiated photon is reduced compared to the inclusive case. Second, only two of the four unpolarized response functions contribute to the inclu-

95

sive case; the Mo and Tsai formula neglects the azimuthal dependences found in exclusive scattering.

An additional objection which has been raised to the Mo and Tsai formulation in general, not just to its use in exclusive scattering, is that they use an un-physical parameter to artificially split the phase space of the radiated photon into soft and hard regions in order to cancel the infrared divergence.

Kin:	a			b		
OOPS	A	B	C	A	B	C
$\langle W \rangle$	1.2284	1.2314	1.2335	1.2295	1.2334	1.2325
$\langle Q^2 \rangle$	0.12838	0.12747	0.12691	0.12799	0.12674	0.12699
$\langle \theta^*_{\pi q} \rangle$	44.121°	44.716°	44.368°	44.298°	3.633°	44.421°
$\langle |\phi_{\pi q}| \rangle$	174.54°	60.774°	61.120°	174.57°	98.008°	90.539°
η_{rad}	1.241	1.202	1.220	1.241	1.247	1.212

Table 4.7: Radiative Correction data and results. The mean values of the kinematic variables in each spectrometer from data are shown, along with the calculated radiative correction. W is given in MeV, Q^2 in $(\text{GeV}/c)^2$, $\theta^*_{\pi q}$ and $\phi_{\pi q}$ in degrees.

In the present analysis we instead use A. Afanasev's Fortran code ExcluRad [45], which calculates the radiative corrections for the specific case of exclusive pion electroproduction from QED, utilizing realistic structure functions from model calculations in order to reproduce the correct azimuthal dependence. The structure functions are calculated using the MAID 2000 model [46]. Furthermore, ExcluRad takes a covariant approach to infrared divergence cancellation, which obviates the artificial cutoff parameter of the Mo and Tsai.

ExcluRad takes as input the kinematic variables W, Q^2, $\cos\theta^*_{\pi q}$ and $|\phi_{\pi q}|$, as well as an inelasticity cutoff parameter v_{cut}, defined as the difference between the square of the upper limit of the missing mass cut and the square of the neutron mass:

$$v_{\text{cut}} \equiv \max(M_{\text{miss}})^2 - M_n^2 \qquad (4.46)$$

For each of the kinematic variables we take the mean value in each OOPS spectrometer, after all cuts, from the data. These values are listed in table 4.7. The upper limit missing

96

mass cut is +4.0 MeV above the peak centroid, as described in section 4.2.3.

97

4.4.3 Pion Decay Correction

Pion Decay

A particular complication to coincidence pion production experiments in the π^+ channel is short mean lifetime of the pion, $\tau = 26.033 \pm 0.005$ ns. The pion decay length, the distance the pion will travel in the laboratory frame during one mean lifetime in its own rest frame, is given by

$$l_\pi = \frac{p_\pi \tau_\pi}{m_\pi} . \tag{4.47}$$

Using the pion mass $m_\pi = 139.6$ MeV/c^2, we calculate for our central momentum of $p_\pi = 332.9$ MeV/c a central decay length of

$$l_\pi(332.9) = 18.62 \text{m}. \tag{4.48}$$

The OOPS central flight path length is $L_{\text{cent}} = 4.67$ m, a substantial fraction of the decay length; we therefore expect to lose a significant number of pions between the target and the detector package, which will reduce the experimental cross section.

The magnitude of the reduction can be roughly predicted with a simple exponential decay law. Assuming central kinematics, the fraction of pions leaving the target which successfully reach the detector package will be given by

$$\frac{N_\pi^{\text{det}}}{N_\pi^{\text{tgt}}} = e^{-L_{\text{cent}}/l_\pi} \equiv \frac{1}{\eta_{\text{decay}}} \tag{4.49}$$

$$= 0.778 \, ,$$

where

$$\eta_{\text{decay}} = 1.29 \tag{4.50}$$

is the *pion decay correction factor*. This is only an estimate of course, and neglects some significant details which must be addressed in order to accurately correct for pion decay.

First of all, because both the flight path through the spectrometer and the pion decay

length depend on the individual pion kinematics, so η_{decay} will be a function of the phase space coordinates. The overall pion decay correction factor will therefore be a convolution of the individual pion decay probability with the OOPS-OHIPS coincidence acceptance phase space volume.

Second, the pion decays by the process $\pi^+ \rightarrow \mu^+ \nu_\mu$ with a branching ratio of 99.99%. The positive muon has a mass of $m_\mu = 105.66$ MeV/c^2, and is indistinguishable from a π^+ in the OOPS scintillators. Therefore some fraction of the muons produced by pion decay will enter the spectrometers and be counted as pions; this will tend to mitigate the observed reduction in the cross section.

However, because the muons originate not at the target but instead from points anywhere along the pion trajectory, they do not share the same correlations between momentum and trajectory through the detector package that the real pions have, and from which the spectrometer optical matrices are derived. Muons misidentified as pions are therefore not accurately reconstructed by the analysis software, leading to a broadening of the missing mass distribution for these events. Pions which would otherwise have fallen within the cut on the missing mass peak may decay into muons which are reconstructed outside of the cut, and vice versa.

GEANT Monte Carlo

The only way to deal with a problem of this complexity is to model it in Monte-Carlo simulation. We chose to rely on the CERN physics simulation tool GEANT [47] for this task rather than using AEEXB, with which we handled all of the other simulation needs of the experiment. GEANT is a much more sophisticated tool than AEEXB, and it has built-in routines for modeling particle decays which are accurate and well tested. AEEXB has no such native capacity; adding such routines would have required an enormous effort in coding and verification, whereas basic GEANT models of the OHIPS and OOPS spectrometers were pre-existing and needed only some modification to suit this purpose. Figure 4-28 shows a graphical representation of the GEANT simulation of particles tracking through the OOPS

spectrometer model.
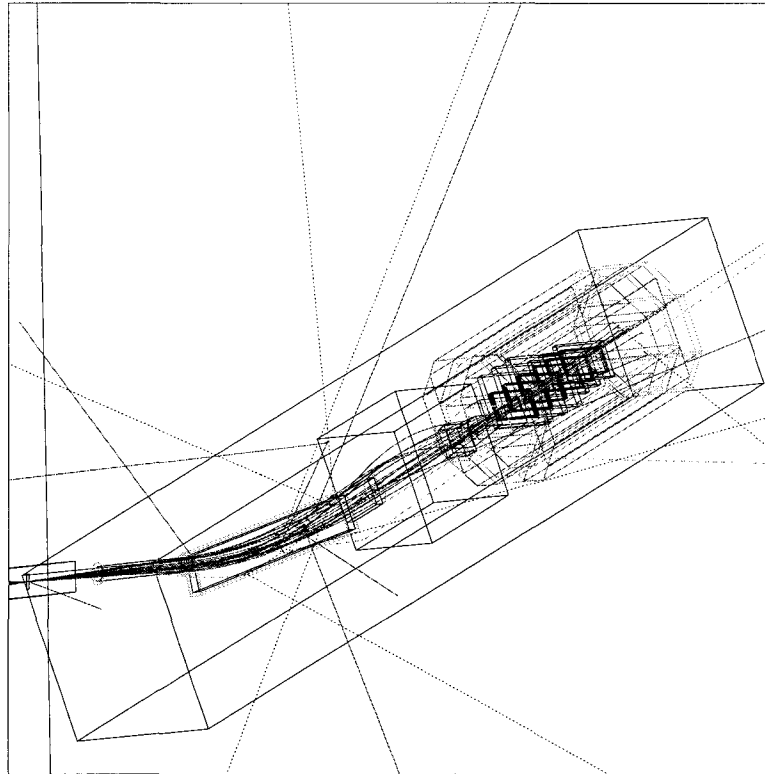
Figure 4-28: GEANT tracks particles through the OOPS spectrometer model, with particle decay enabled. The red tracks represent π^+, the green dashed lines are μ^+ particles.

Particle coordinate detection was added at each of the three HDC planes in the OOPS model, with randomized Gaussian errors added to recreate the actual tracking resolution of the spectrometers. GEANT then creates a reconstructed particle track by least-squares fit to these coordinates, and projects the transport coordinates (x, θ, y, ϕ) to the front of the first chamber plane.

An optical matrix was created to convert these reconstructed chamber coordinates to reconstructed target coordinates (δ, θ, ϕ). This was done by randomly generating white-spectrum events into the the OOPS acceptance, and reading out both the generated target and reconstructed chamber coordinates for each event, and performing a multiparameter polynomial fit as described in section 4.1.7. The reconstructed target coordinates are then used to calculate the missing mass. Figure 4-29 shows the reconstructed GEANT missing

100

mass spectrum in comparison with actual data, while figure 4-30 shows the GEANT missing mass peak separated into pion and muon contributions. The poor reconstruction of the muons is clearly visible.

(a) GEANT and data Missing Mass peaks

(b) GEANT Missing Mass peak region
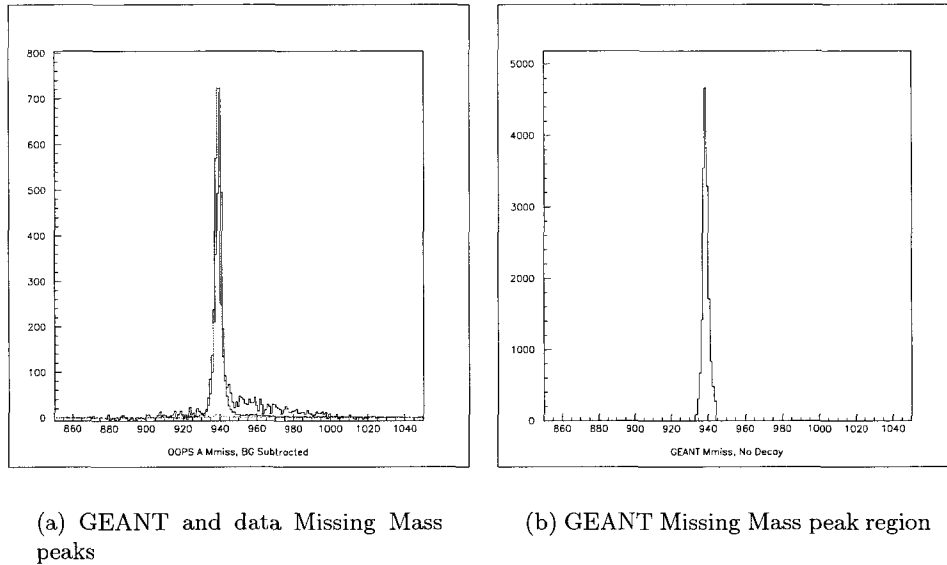
Figure 4-29: Missing mass peaks in data and GEANT simulation. (a) Data (black) are compared to GEANT Monte Carlo with pion decay. Pions (blue) and muons (green) are shown separately. The simulated spectra are normalized such that the sum of the pion and muon peaks are the same height as the data. (b) The GEANT missing mass peak inside of the 3σ cut region (pions only).

In order to calculate the pion decay correction, 100,000 $N \to \Delta$ events are generated in GEANT with the particle decay feature disabled. Some number $N^{\text{det}}_{\text{no decay}}$ of these events reach the detectors in both spectrometers and survive all cuts (acceptance and missing mass). The simulation is then repeated with the decay turned on. Muons produced by the pion decay are tracked through the chambers and reconstructed by the optics as though they were pions. All events are flagged with particle type at detection, however, so that we may separate them.

Since we cannot experimentally distinguish between muons and pions, our total number of detected particles is the number of pions plus the number of muons reaching the detectors and surviving all cuts,

$$N^{\text{det}}_{\text{decay}} = N^{\text{det}}_{\pi^+} + N^{\text{det}}_{\mu^+} \tag{4.51}$$

101

(a) π^+ (b) μ^+
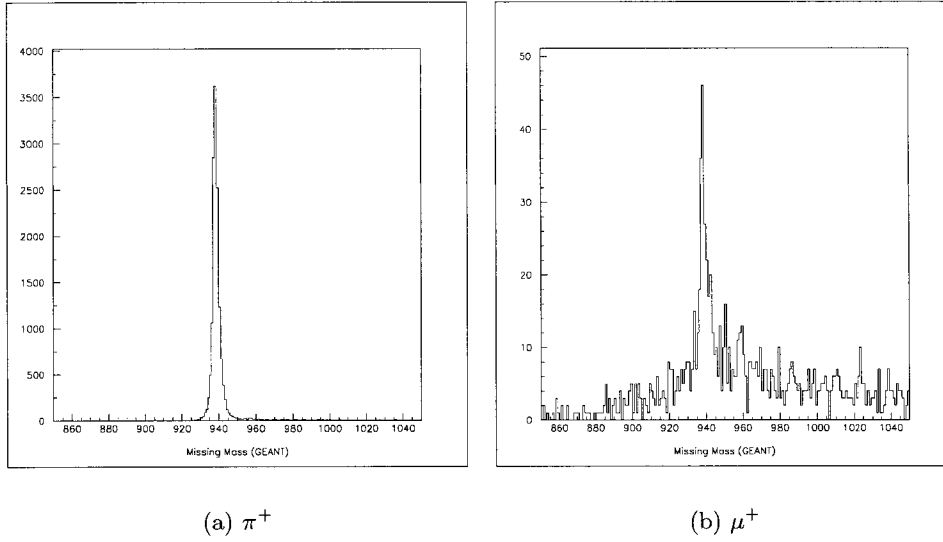
Figure 4-30: Reconstruction of π^+ and μ^+ in GEANT Missing mass spectrum. The poor reconstruction of muon tracks in the wire chamber is evident.

The pion decay correction is then calculated for each spectrometer as

$$\eta_{\text{decay}} = \frac{N^{\text{det}}_{\text{no decay}}}{N^{\text{det}}_{\text{decay}}} \qquad (4.52)$$

The numbers of detected particles with and without pion decay in simulation for each spectrometer, and the corresponding correction factors, are shown in table 4.8.

Kin:	a			b		
OOPS	A	B	C	A	B	C
$N^{\text{det}}_{\text{no decay}}$	20012	17041	17274	20012	14104	18584
$N^{\text{det}}_{\pi^+}$	15205	13165	13188	15205	11092	14317
$N^{\text{det}}_{\mu^+}$	516	496	589	516	362	526
η_{decay}	1.27	1.25	1.25	1.27	1.23	1.25

Table 4.8: Pion decay calculation data

102

4.4.4 Finite Solid Angle Correction

Because of their finite momentum and solid angle bites, the spectrometers sample the cross section over a small but finite volume of phase space, while the theoretical models with which we wish to compare the data calculate the cross section for a single kinematic point. In order to make a meaningful comparison between the two, a correction factor is applied to compensate for the effects of averaging over the spectrometer acceptance.

For each accepted event, the kinematic phase space coordinates $x_i = \{Q^2, W, \theta^*_{\pi q}, \phi_{\pi q}\}$ are saved to a file by the ColaMIT analyzer. The model cross section is calculated at that event's kinematics and compared to the model cross section at the central kinematics x_0 of the corresponding spectrometer. A weight factor w_i is calculated for that event as the ratio

$$w_i = \frac{\frac{d\sigma}{d\Omega}(x_0)}{\frac{d\sigma}{d\Omega}(x_i)}, \tag{4.53}$$

where $d\sigma/d\Omega$ indicates the 5-fold laboratory-frame cross section.

The finite-acceptance correction factor $\eta_{\mathrm{acc.}}$ is then calculated as the weighted sum of events divided by the raw number of events N,

$$\eta_{\mathrm{acc.}} \equiv \frac{\tilde{N}}{N} = \frac{1}{N} \sum_{i=1}^{N} w_i. \tag{4.54}$$

While this introduces some model dependence into the analysis, it is ameliorated by the fact that the collapse factor does not depend on the absolute magnitude of the model cross section, but on its derivative. Over the small volume of phase space in the coincidence acceptance, the variation is very similar from model to model. The model error is estimated by calculating the collapse factor using two models: the MAID 2003 parameterization [7], and the dynamical DMT model. This error is found to be on the order of 0.5%.The collapse factors calculated for each spectrometer are listed in tables 4.9 and 4.10.

$\phi_{\pi q}$	N_{Data}	$\eta_{\text{acc.}}$(MAID2003)	$\eta_{\text{acc.}}$(DMT)	$\eta_{\text{acc.}}$(Average)	$\delta\eta_{\text{acc.}}/\eta_{\text{acc.}}$
180°(a)	2878	1.00703	1.01634	1.01168	0.65%
180°(b)	4464	1.02857	1.02860	1.02858	0.02%
60°	2920	1.03587	1.036	1.03601	0.02%
−60°	2757	1.02742	1.02970	1.02856	0.16%
90°	4210	1.04015	1.03988	1.04002	0.02%

Table 4.9: Weighted event sums and collapse factors for the fivefold differential, coincidence cross-section measurements at $\theta^*_{\pi q} = 44.45°$ using the MAID2003 and DMT models.

N_{Data}	$\eta_{\text{acc.}}$(MAID2003)	$\eta_{\text{acc.}}$(DMT)	$\eta_{\text{acc.}}$(Average)	$\delta\eta_{\text{acc.}}/\eta_{\text{acc.}}$
5023	1.05156	1.04742	1.04950	0.28%

Table 4.10: Weighted event sums and collapse factors for the fivefold differential, coincidence cross-section measurement at $\theta^*_{\pi q} = 0°$ using the MAID2003 and DMT models.

104

4.5 Hydrogen Elastic Normalization

Measurement of the elastic scattering reaction $H(e, e'p)$ provides a standard method for testing and calibrating spectrometer systems. Because the scattering cross-section is well known (See, for example, Friedrich and Walcher [48]), such measurements serve as benchmark tests to study the overall consistency and absolute efficiencies of the coincidence detection setup, and allow the estimation of uncertainties in experimental quantities such as the target density and phase-space volume calculations, which are not easily determined by other means.

For this experiment, a series of such elastic calibration runs were performed, prior to taking the $H(e, e'\pi^+)n$ data, using OHIPS and the in-plane OOPS module (OOPS A) at a beam energy of 950 MeV. OHIPS was positioned for an electron scattering angle of $\theta_e = 35.51°$, giving a proton recoil momentum of $P_p = 552.42$ MeV and a four-momentum transfer $Q^2 = 0.283$ GeV^2.

By varying the OOPS magnetic field setting from +9 % to -9% of the nominal value, the elastic scattering peak is scanned across the OOPS focal plane; the position is indexed by the parameter δp, defined as the percent difference of momentum of the detected particle from the momentum of the central ray for the field strength setting:

$$\delta p = \frac{(p_{\text{det.}} - p_{\text{cent.}})}{p_{\text{cent.}}} \times 100 \tag{4.55}$$

The measured coincidence cross section is calculated as

$$\frac{d\sigma}{d\Omega_e} = \frac{N_{\text{coinc}}}{\mathcal{L}\Delta\Omega_e} \times \eta \tag{4.56}$$

Here N_{coinc} is the number of coincidence events detected after all cuts, $\mathcal{L}$ is the luminosity, $\Delta\Omega_e$ is the coincidence electron phase-space acceptance volume, and η is the product of the Computer-Busy, chamber tracking, and radiative correction factors:

$$\eta = \eta_{\text{CB}} \times \eta_{\text{track}} \times \eta_{\text{rad}}. \tag{4.57}$$

105

All factors in the cross section were calculated independently for each run by the methods already described in this thesis in the appropriate sections.

4.5.1 Theory

The hydrogen elastic cross section is given by the Rosenbluth formula for electron scattering on nucleons (see, for example reference [49]):

$$\left(\frac{d\sigma}{d\Omega}\right) = \left(\frac{d\sigma}{d\Omega}\right)^*_{Mott} \cdot \frac{E'}{E} \cdot \left[\frac{G_E^2(Q^2) + \tau G_M^2(Q^2)}{1 + \tau} + 2\tau G_M^2(Q^2) \tan^2\frac{\theta}{2}\right] . \tag{4.58}$$

where $\tau = \frac{Q^2}{4M_p}$. Three factors comprise the Rosenbluth cross-section. The first is the Mott cross-section, which approximates the calculation in the low energy limit that the recoil, magnetic moment, and finite spatial extent of the proton can all be neglected. In the extreme low energy regime, this reduces to the non-relativistic Rutheford cross section. The Mott factor is given by

$$\left(\frac{d\sigma}{d\Omega}\right)^*_{Mott} = \frac{Z^2\alpha^2}{4\vec{p}^2\beta^2\sin^4\frac{\theta}{2}} \cdot \left(1 - \beta^2\sin^2\frac{\theta}{2}\right) \tag{4.59}$$

The next factor, $\frac{E'}{E}$, accounts for the recoil of the target.

The third factor, in the square brackets, contains the electric and magnetic form factors and accounts for both the magnetic moment and the dispersed structure of the proton. Here $G_E^2(Q^2)$ and $G_M^2(Q^2)$ are the electric and magnetic form factors, which represent the Fourier transforms of the charge and current density spatial distributions, $\rho(\vec{r})$ and $j(\vec{r})$, respectively.

The form factors are nominally described by the *dipole approximation* (see for example [?]):

$$G_E^P(Q^2) = \left(1 + \frac{Q^2}{0.71(\text{GeV}/\text{c})^2}\right) \tag{4.60}$$

and

$$G_M^P(Q^2) = 2.79 \times G_E^P(Q^2) . \tag{4.61}$$

106

which correspond to a spatial density distribution

$$\rho(\vec{r}) \sim \rho_0 e^{-a \cdot r},\tag{4.62}$$

with $a = 4.27\ \text{fm}^{-1}$. At the present kinematics, the dipole approximation yields a cross section of

$$\frac{d\sigma}{d\Omega_e} = 0.217\,\mu\text{b/sr}\tag{4.63}$$

The world data on nucleon form factors, however, shows a clear deviation from the dipole approximation in the vicinity of $Q^2 = 0.2$ GeV. Friedrich and Walcher [48] have documented this deviation, describing it to high precision with a phenomenological fit, and posit a pion cloud model to account for the effect. Their empirical fit is used here for comparison to the present data, . Hammer and Meißner have also successfully described this with a dispersion-theoretical analysis [50].

4.5.2 Cross Section Results

The results of the hydrogen elastic cross section studies are shown in figure 4-31, for each run in the δ-scan series. The error bars shown include statistical errors as well as uncertainties in the determination of the relevant correction factors. Combining the individual measurements yields an overall elastic cross section of 0.205 ± 0.003 $\mu\text{b/sr}$, in excellent agreement with the Friedrich and Walcher fit value of 0.206 $\mu\text{b/sr}$.

107
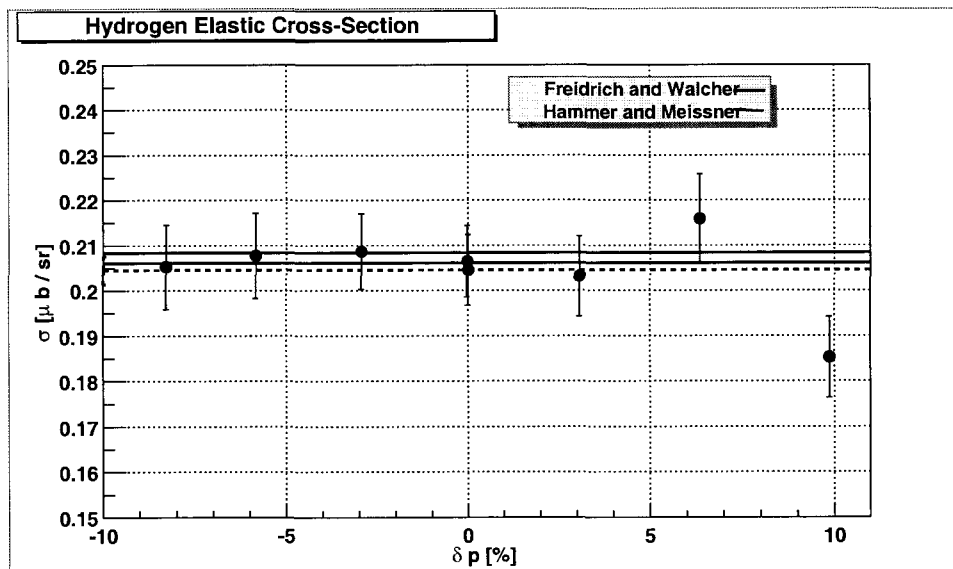
Figure 4-31: Experimental results for the elastic scattering differential cross section from all eight delta settings, in microbarns per steradian. The dashed line shows the phenomenological fit by Friedrich and Walcher to the world database at the kinematics of the present measurement, the solid line shows the average of the measurements and the dashed-dotted line is the dipole fit, which deviates from the world data at this Q^2

108

CHAPTER 5

Results

5.1 Spectrometer Cross Sections

The two-fold differential hadronic cross section in the CM frame is

$$\frac{\mathrm{d}\sigma}{\mathrm{d}\Omega_{\pi q}^*} = \frac{1}{\Gamma}\frac{1}{J}\frac{\mathrm{d}^5\sigma}{\mathrm{d}\Omega_e\,\mathrm{d}\Omega_{\pi q}\,\mathrm{d}E'}, \tag{5.1}$$

where Γ is the virtual photon flux factor, determined by electron arm kinematics,

$$\Gamma = \frac{\alpha}{2\pi^2}\frac{E_f}{E_i}\frac{k_\gamma}{Q^2}\frac{1}{1-\varepsilon} \tag{5.2}$$

$$= 2.430 \times 10^{-06}\{\mathrm{MeV}\cdot\mathrm{sr}\}^{-1}, \tag{5.3}$$

and J is the Jacobian determinant, which supplies the conversion factor between the solid angle in the center of mass and laboratory coordinates. This is given by

$$J = \frac{1}{\gamma}\left(\frac{p_\pi}{p_\pi^*}\right)^3\frac{1}{1+\beta\frac{E_\pi^*}{p_\pi^*}\cos\theta_{\pi q}^*}. \tag{5.4}$$

109

Since the Jacobian is independent of $\phi_{\pi q}$, we need only calculate the value twice: Once for the central kinematics at $\theta_{\pi q}^* = 44.45°$ and once at $\theta_{\pi q}^* = 0°$. We find

$$J = \begin{cases} 2.1885 & \text{for } \theta_{\pi q}^* = 44.45° \\ 2.5876 & \text{for } \theta_{\pi q}^* = 0° \end{cases} \tag{5.5}$$

The remainder of equation 5.1 is the five-fold experimental scattering cross section, in the laboratory frame, which is calculated from the experimental data:

$$\frac{\mathrm{d}^5\sigma}{\mathrm{d}\Omega_e \mathrm{d}\Omega_\pi \mathrm{d}E'} = \frac{N}{\mathcal{L}\,\Delta\Omega} \times \eta\,. \tag{5.6}$$

On the right hand side of the equation:

- N is the number of coincidence events in the missing mass peak after all cuts are applied

- $\mathcal{L}$ is the luminosity, defined by

$$\mathcal{L} = N_e \cdot N_p\,. \tag{5.7}$$

In this expression N_e is the number of incident electrons, found by dividing the total beam charge Q by 1.602×10^{-19} C. N_p gives the target proton density per unit area,

$$N_p = \rho \cdot N_\mathrm{A} \cdot \ell\,, \tag{5.8}$$

for target density ρ and target length ℓ. N_A is Avogadro's number, 6.022×10^{23} mol$^-$1.

- $\Delta\Omega$ is the coincidence acceptance phase space volume determined by Monte-Carlo

- η is the combined product of all correction factors,

$$\eta = \eta_\mathrm{dt} \cdot \eta_\mathrm{hdc} \cdot \eta_\mathrm{vdc} \cdot \eta_\mathrm{rad} \cdot \eta_\mathrm{bg} \cdot \eta_\mathrm{decay} \cdot \eta_\mathrm{f.a.}\,. \tag{5.9}$$

The hadronic cross sections calculated for each spectrometer are listed in table 5.1. Note

110

that the duplicate measurements made by OOPS A at $\phi_{\pi q} = 180°$ in both kinematic settings agree with one another well within the statistical errors, confirming the normalization between the two sets of measurements. Similarly, the duplicate measurements at $|\phi_{\pi q}| = 60°$ by OOPS B and C in kinematics a are in excellent agreement.

Kin.	OOPS	$(\theta^*_{\pi q}, \phi_{\pi q})$	$d^2\sigma_{exp}$	MAID	DMT	Sato-Lee
	A	$(44.45, 180)$	18.39 ± 0.64	21.35	20.67	15.53
a	B	$(44.45, 60)$	20.84 ± 0.64	20.96	19.73	17.27
	C	$(44.45, -60)$	20.65 ± 0.67	20.96	19.73	17.27
	A	$(44.45, 180)$	18.24 ± 0.57	21.35	20.67	15.53
b	B	$(0, —)$	22.85 ± 0.58	25.37	23.31	16.15
	C	$(44.45, 90)$	26.49 ± 0.69	26.69	25.33	21.39

Table 5.1: The two-fold hadronic point cross sections in the CM frame, and model predictions

The two pairs of duplicate cross sections are combined, and the results listed in table 5.2. The final $\theta^*_{\pi q} = 44.45°$ cross sections are then plotted in figure 5-1, along with several model calculations for comparison. Shown are the MAID2003, DMT and Sato-Lee model cross sections, as well as the chiral perturbation theory (ChPT) calculation of Pascalutsa and Vanderhaegen [51]. The cross section is plotted as a function of the azimuthal pion emission angle $\phi_{\pi q}$. Since the $\theta^*_{\pi q} = 0°$ cross section measured by OOPS B in kinematics configuration "b" measures the linear combination σ_0 directly, that data point is plotted with the partial cross section results in section 5.2.

$(\theta^*_{\pi q}, |\phi_{\pi q}|)$	$d^2\sigma_{exp}$
$(44.45, 180)$	$18.34 \pm 0.35 \pm 0.68$
$(44.45, 60)$	$20.74 \pm 0.42 \pm 0.64$
$(44.45, 90)$	$26.49 \pm 0.69 \pm 1.01$
$(0, —)$	$22.85 \pm 0.58 \pm 0.87$

Table 5.2: The combined two-fold hadronic point cross sections in the CM frame. Statistical and systematic errors are shown.

Already we note in figure 5-1 that the Sato-Lee model underestimates the cross section significantly at this low Q^2. This is initially somewhat surprising, as at higher four-momentum transfers recent data taken at CLAS show a preference for this model; however

111

more recent CLAS data in the π^+ channel appear to confirm this failure of the Sato-Lee model as Q^2 decreases toward 0.2 GeV^2 [22].

At the other extreme, the ChPT result is seen to *over*estimate the cross section at all azimuthal angles.

Both the MAID and DMT models predict the data well for $\phi_{\pi q} = 60°$ and $90°$, but both significantly diverge from the observed cross section at $\phi_{\pi q} = 180°$. The agreement between model and experiment may be explored in greater detail by extracting the partial cross sections.
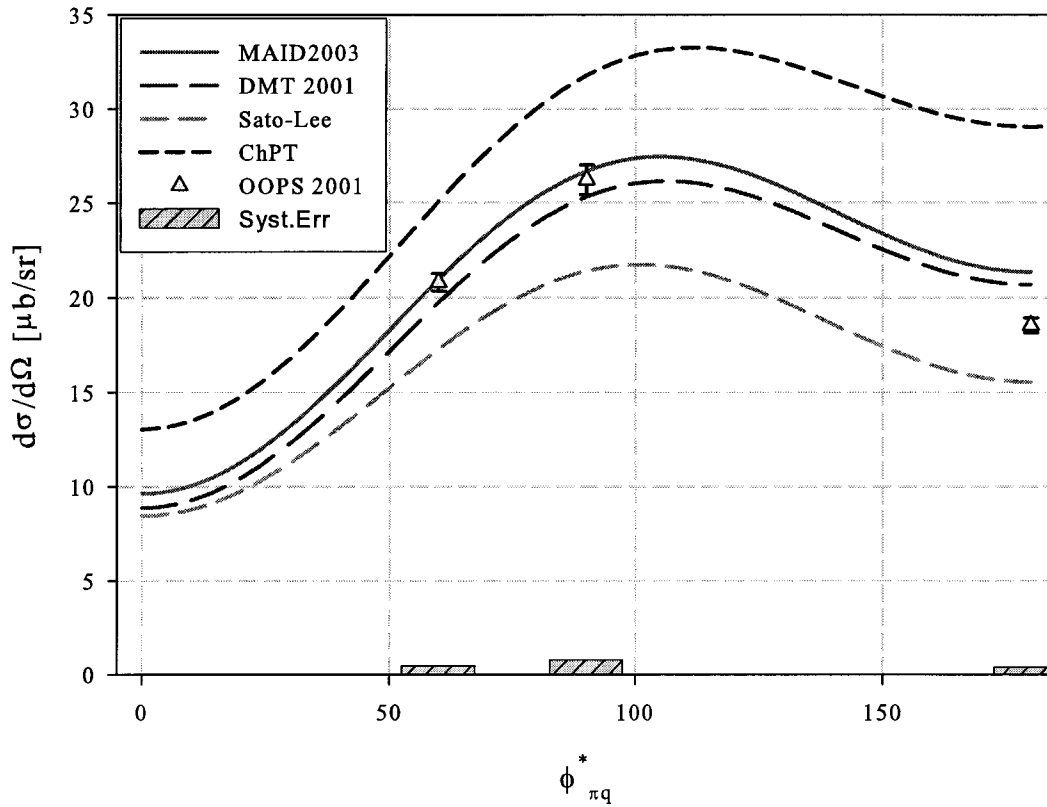
Figure 5-1: Spectrometer Cross Sections collapsed to point kinematics at $\theta^*_{\pi q} = 44.45°$, $Q^2 = 0.127$ GeV^2/c^2, $W = 1232$ MeV

5.2 The Partial Cross Sections

The partial cross sections are extracted algebraically according to equations 3.1 — 3.3, reprinted here for convenience:

$$\sigma_0 = \frac{\sigma(180°) + 2\sigma(60°)}{3} \tag{3.1}$$

$$\sigma_{TT} = \frac{\sigma(180°) + 2\sigma(60°) - 3\sigma(90°)}{3\varepsilon} \tag{3.2}$$

$$\sigma_{LT} = \frac{4\sigma(60°) - 3\sigma(90°) - \sigma(180°)}{3\sqrt{\varepsilon(1+\varepsilon)}} \tag{3.3}$$

The results are displayed along with the model calculations of MAID, DMT and Sato-Lee in table 5.3. The extracted partial cross sections are shown in figures 5-2 — 5-3, along with

$\theta_{\pi q}^* = 44.45°$				
σ	Data	MAID 2003	DMT	Sato-Lee
σ_0	$20.09 \pm 0.30 \pm 0.52$	21.09	20.05	16.69
σ_{TT}	$-7.99 \pm 1.100 \pm 1.33$	-7.30	-6.88	-6.132
σ_{LT}	$-2.72 \pm 0.59 \pm 0.67$	-3.56	-3.59	-2.152
$\theta_{\pi q}^* = 0°$				
σ	Data	MAID 2003	DMT	Sato-Lee
σ_0	$22.85 \pm 0.58 \pm 0.87$	25.37	23.31	16.15

Table 5.3: Extracted partial cross sections, with statistical and systematic errors. Model predictions are listed for comparison

MAID2003, DMT and Sato-Lee model predictions for comparison, as a function of $\theta_{\pi q}^*$.

113
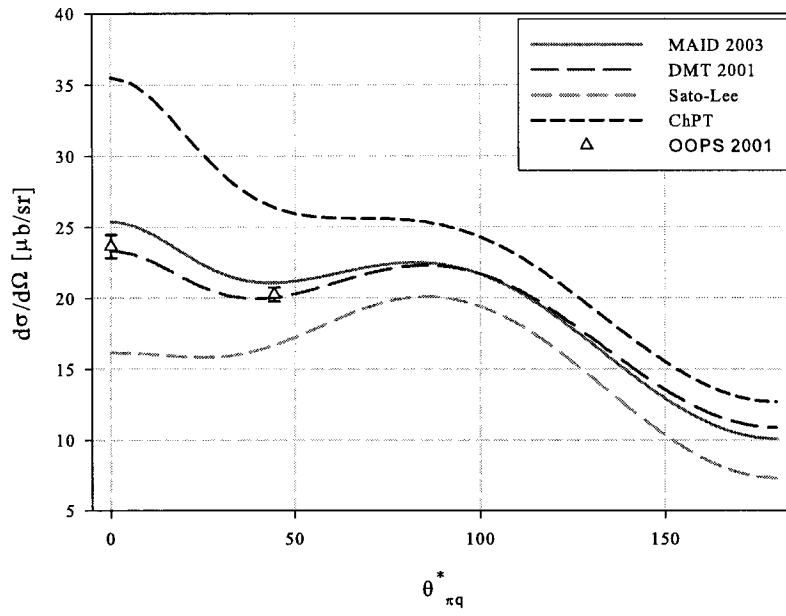
Figure 5-2: The partial cross section σ_0 at $Q^2 = 0.127$ GeV^2/c^2, $W = 1232$ MeV

114
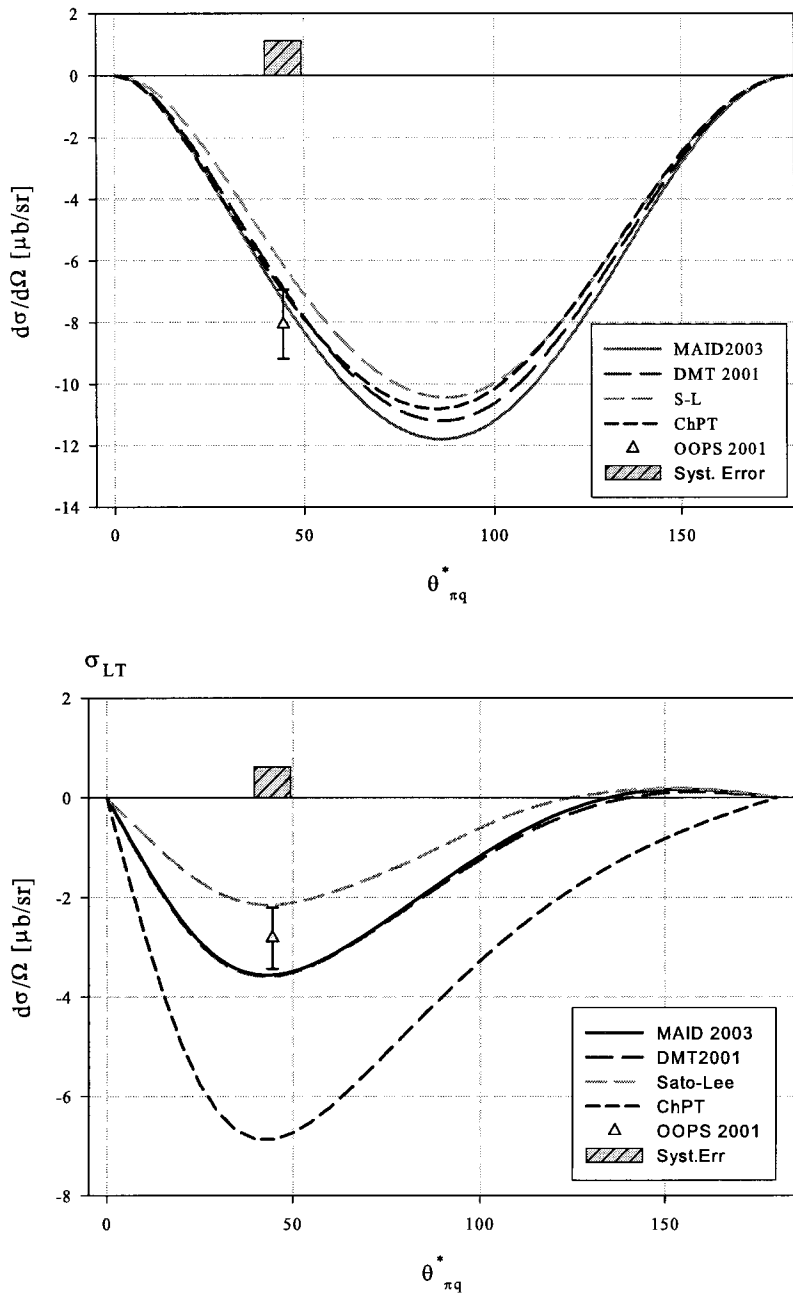
Figure 5-3: The partial cross sections σ_{TT} and σ_{LT} at $Q^2 = 0.127$ GeV^2/c^2, $W = 1232$ MeV.

In figure 5-2, showing the linear combination of partial cross sections $\sigma_0 = \sigma_T + \varepsilon\sigma_L$, it is clear that the DMT model most successfully predicts the data. MAID 2003 does very well at the larger angle, but begins to slightly overestimate the partial cross section as $\theta_{\pi q}^*$ goes

115

to zero. The Sato-Lee model, on the other hand, underestimates the cross section rather dramatically; in particular the model is seen to flatten out below about $\theta_{\pi q}^* = 30°$, failing to capture a distinct rise in the cross section toward zero which both other models anticipate. ChPT overestimates σ_0 considerably at both data points.

The top of figure 5-3 shows the same comparison with models for the partial cross section σ_{TT}. Here both MAID, DMT, and ChPT agree with the data and each other within the statistical errorbars, Sato-Lee is not far outside of that.

The interference cross section σ_{LT}, in the bottom of figure 5-3, splits the difference between the model predictions of Sato-Lee on the one hand, and MAID and DMT, which are in close agreement here, on the other. With this data point we begin to run up against the constraints of the limited statistics of this experiment. Because of the small size of the extracted cross section, the statistical error on the order of 0.7 μb is a substantial fraction of the measured value, and similarly for the systematic error. It is therefore difficult to make a definitive statement about these three models based on this point alone. Only the ChPT calculation is in clear disagreement with the data.

5.3 Systematic Errors

In addition to the statistical uncertainties (counting error) inherent in the process of data collection itself, and the small model error introduced by the finite acceptance correction, the other major category of experimental uncertainties is due to systematic uncertainties in the experimental setup. The primary sources for such systematic errors are the uncertainties in:

- **Beam energy**: 0.1%

- **Spectrometer alignment**, based on the listed uncertainties in the survey data during the experiment set-up:

  - OHIPS angle θ_e: 0.1°

  - OOPS in-plane angle α: 0.05°

116

– OOPS out-of-plane angle β: 0.05°

- **Luminosity**: 1.5 %

- **Phase space volume $\Delta\Omega$**: $\leq 2.7\%$

- **Radiative corrections**: 1%

- **Pion decay corrections**: 1.5%

The errors in the final cross section results results due to such experimental uncertainties are estimated in Monte-Carlo simulation using AEEXB. Each of the sources of error listed above is varied independently in the simulation, and all spectrometer and partial cross section results are re-calculated using the pseudo data so generated.

Care must be taken to properly model correlations between the effects of systematic errors in the various spectrometers.

For example, the errors on the beam energy in kinematics a and kinematics b are independent from one another. However, a decrease in beam energy in kinematics a will effect all three spectrometers in kinematics a in a fixed way: it may increase the observed cross section in OOPS A, while decreasing the measurements in OOPS B and C. The effects on the individual spectrometers are not independent, and do not add in quadrature when propagating them to the partial cross section results. Instead, the kinematics a beam energy is decreased to its -1σ value, while the kinematics b beam energy is left at its nominal value. All spectrometer and partial cross sections are then recalculated. This is repeated with the kinematics a beam energy increased to its $+1\sigma$ value. The variation observed in each cross section result is the uncertainty due to the kinematics a beam energy. The whole procedure is repeated again for the kinematics b beam energy. For each cross section result, the variations in kinematics a and b can then be added in quadrature to give a total error due to beam energy uncertainty, since the variations in kinematics a and b are independent of one another.

The alignment error for OHIPS is constant between kinematics settings, as the spectrometer was not moved, so the effect on the cross sections is calculated by changing it in

117

the same direction in both kinematics at once. The OOPS A alignment errors are similarly constant between settings, for the same reason, and their effects add directly to the combined 180° cross section measurements.

The situation is the opposite for the combined $|\phi| = 60°$ measurement; because it is averaged over measurements in two separate spectrometers, OOPS B and C, the alignment errors of the two are independent and add in quadrature to the final result.

The phase space volume errors are independent of one another for each spectrometer in each kinematics, with the exception, as above, of OOPS A which is never moved. Similarly, the radiative and pion decay corrections are determined independently for each spectrometer in each setting, and the errors are treated as independent for all measurements except the two by OOPS A. The error in luminosity is taken as fixed between the two kinematics, as it represents a calibration error in current and target density measurements, and not a fluctuation.

Kin.	Spec	E	θ_e	α, β	$\Delta\Omega$	$\mathcal{L}$	η_{rad}	η_{decay}	total
	$d\sigma/d\Omega(\phi = 180°)$	0.7%	0.8%	0.3 %	2.7%	1.5%	1.0 %	1.5%	3.7%
a	$d\sigma/d\Omega(\phi = 60°)$	1.1%	0.5%	0.5%	2.7%	1.5%	1.0 %	1.5%	3.8%
	$d\sigma/d\Omega(\phi = 300°)$	1.1%	0.5%	0.5%	2.7%	1.5%	1.0 %	1.5%	3.8%
	$d\sigma/d\Omega(\phi = 180°)$	0.7%	0.8%	0.3%	2.7%	1.5%	1.0 %	1.5%	3.7%
b	$d\sigma/d\Omega(\phi = 90°)$	1.3%	0.8%	0.5%	2.7%	1.5%	1.0 %	1.5%	3.9%
	$d\sigma/d\Omega(\theta = 0°)$	1.0%	0.8%	0.6%	2.7%	1.5%	1.0 %	1.5%	3.8%

Table 5.4: Systematic errors for individual spectrometer cross sections due to kinematic quantities.

σ	E	θ_e	α, β	$\Delta\Omega$	$\mathcal{L}$	η_{rad}	η_{decay}	total
$d\sigma/d\Omega(\phi = 180°)$	0.5%	0.8%	0.3%	2.7%	1.5%	1%	1.5%	3.7%
$d\sigma/d\Omega(\phi = 60°)$	1.1%	0.5%	0.35%	1.96%	1.5%	0.73%	1.09%	3.1%
$d\sigma/d\Omega(\phi = 90°)$	1.0%	0.8%	0.5%	2.7%	1.5%	1.0%	1.5%	3.8%
$d\sigma/d\Omega(\theta = 0°)$	0.7%	0.8%	0.6%	2.7%	1.5%	1.0%	1.5%	3.8%

Table 5.5: Systematic errors for combined cross section results.

The resulting systematic errors in the individual spectrometer cross sections are listed, by source, in table 5.4. These are added in quadrature to give th total systematic errors

118

σ	E_e	θ_e	α/β	$\Delta\Omega$	$\mathcal{L}$	η_{rad}	η_{decay}	total
σ_0	.68%	0.1%	0.93%	1.6%	1.5%	0.659%	0.59%	2.6%
σ_{TT}	4.92 %	0.5%	2.18%	12%	1.5%	4.44%	6.67%	16.7%
σ_{LT}	8.75%	2.93%	3.38%	18.71%	1.5%	6.93%	10.39%	24.6%
$\sigma_0(\theta = 0)$	0.7%	0.8%	0.6%	2.7%	1.5%	1.0 %	1.5%	3.8%

Table 5.6: Systematic errors for extracted partial cross sections.

in the right hand column. The propagation of these errors into the combined point cross sections is shown, again by source, in table 5.5. Finally, the errors in the extracted partial cross sections are given in table 5.6.

119

5.4 Discussion
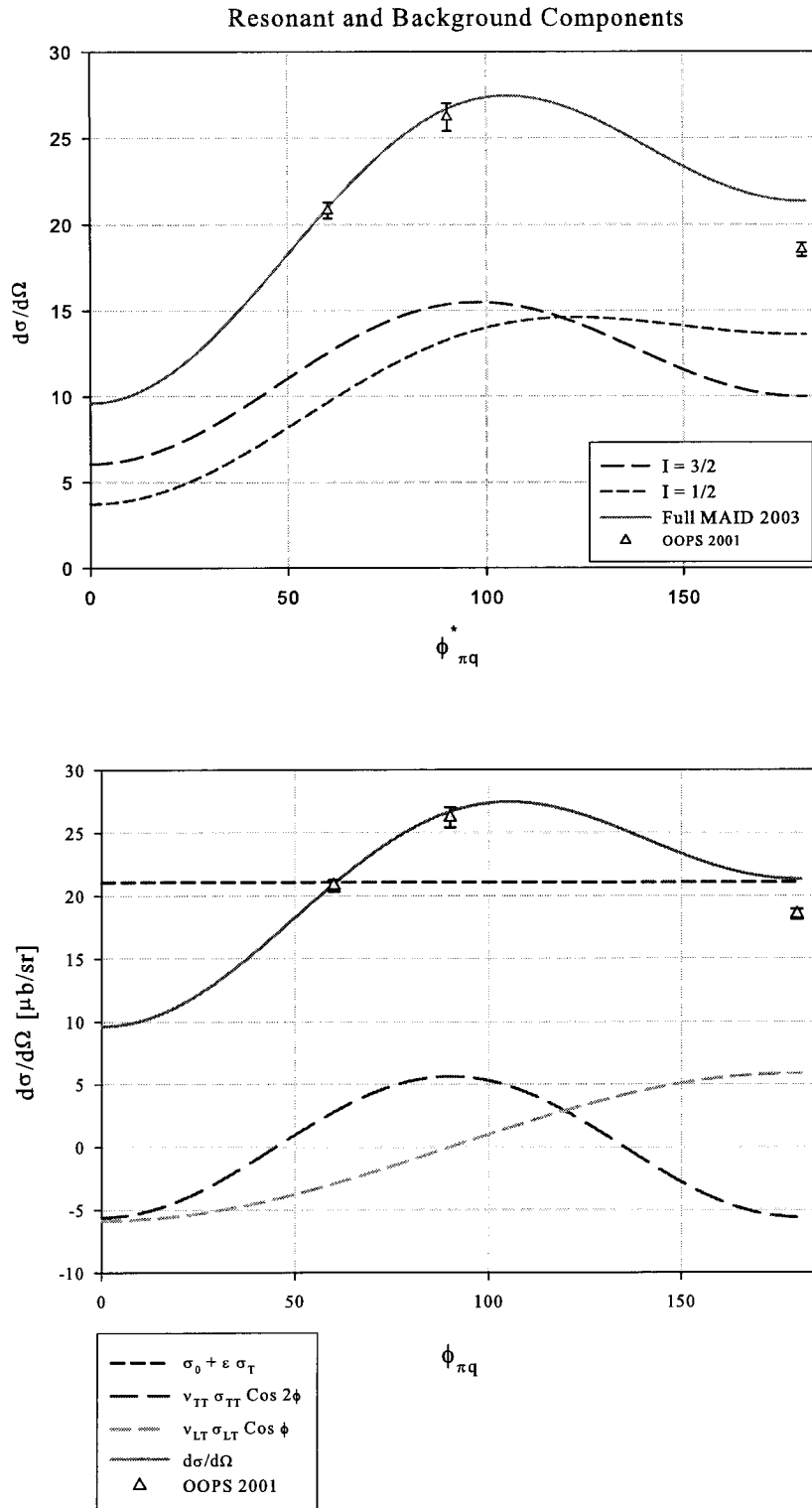
Figure 5-4: The spectrometer cross sections at $\theta^*_{\pi q} = 44.45°$, $Q^2 = 0.127$ GeV^2/c^2 and $W = 1232$ MeV are compared to MAID 2003, showing decomposition into resonant and background (top), and partial cross section contributions (bottom).

120

The single pion electroproduction database for the $p(e, e'\pi^0)p$ reaction channel is by now rather extensive. Because those measurements are twice as sensitive to the resonant $I = 3/2$ multipoles as the present π^+ measurements, we may to first order regard the resonant multipoles as well determined. Indeed, the primary motivation for measuring the $p(e, e'\pi^+)n$ cross sections is to measure the background, and not the resonant multipoles. It is instructive then to consider the spectrometer cross sections in light of the predicted contributions from the resonance and background parts.

The upper panel of figure 5-4 shows the 2-fold differential cross sections at $\theta^*_{\pi q} = 44.45°$ plotted with the MAID2003 model, and the resonant and background parts thereof, as a function of $\phi_{\pi q}$. What can clearly be seen here is that by far the greatest non-resonant contribution to the cross section occurs at $\phi_{\pi q} = 180°$, where it is in fact predicted by the model to be larger than the resonant part. That this is the only azimuthal angle for which the models fail to predict the data suggests that none of them properly calculates the background terms.

The lower panel of 5-4 shows the contributions of each of the separable partial cross sections to the measured spectrometer cross sections at $\theta^*_{\pi q} = 44.45°$. Again, these are calculated using the MAID2003 model. Here it is seen that the longitudinal-transverse interference cross section σ_{LT}, which in section 5.2 was observed to be calculated well by none of the models, contributes most significantly to the overall cross section at the poorly predicted $\phi_{\pi q} = 180°$ data point.

The similar theoretical decomposition of the partial cross section σ_0 into its resonant and background parts is shown in figure 5-5 (top). Again, this is strongly suggestive that the increasing divergence of theory and the present experimental results toward $\theta^*_{\pi q} = 0°$ is due to a failure of the models to properly account for the background contributions, which dominate the cross section below $40°$.

121
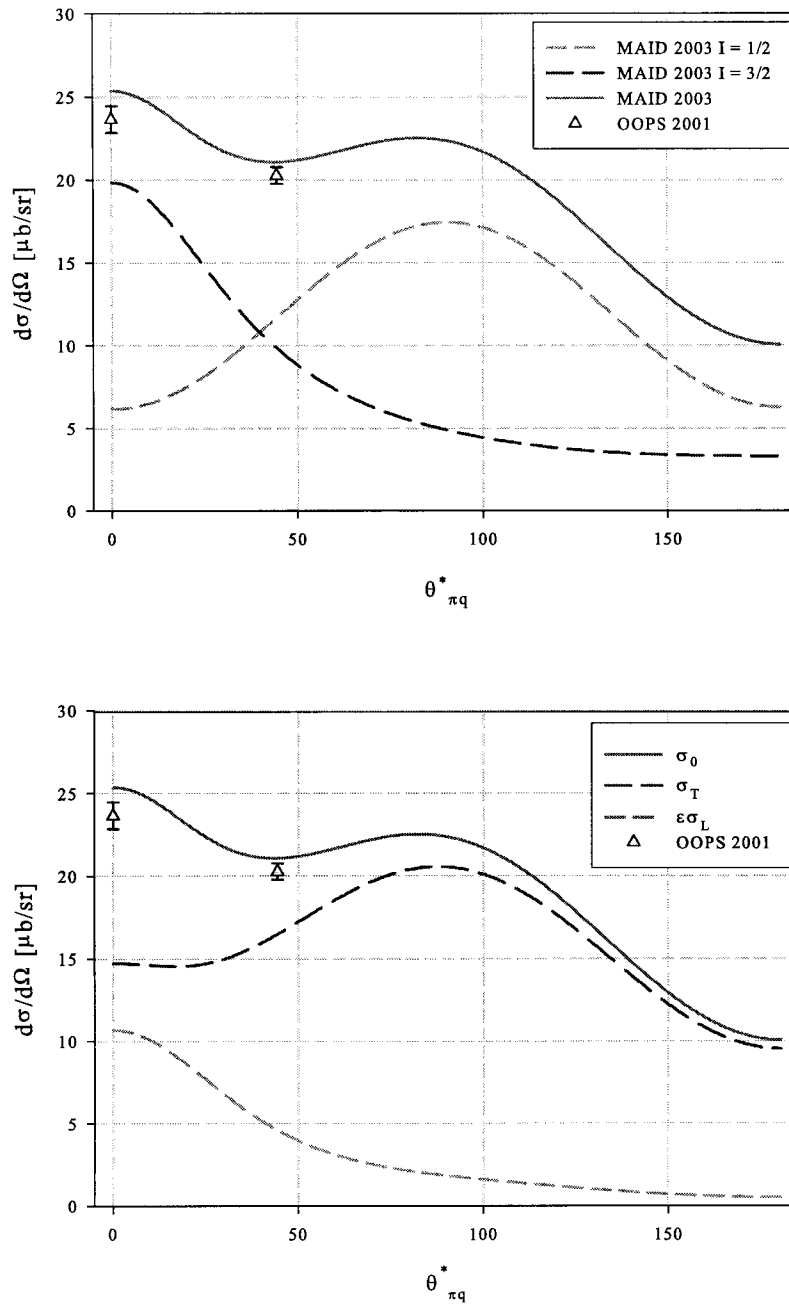
Figure 5-5: The partial cross section σ_0 at $Q^2 = 0.127$ GeV^2/c^2 and $W = 1232$ MeV compared to MAID 2003, showing decomposition into resonant and background (top), and longitudinal and transverse contributions (bottom).

In the lower part of the figure, it is shown that in the same low θ region the longitudinal

122

cross section contributes maximally to σ_0. It is worth noting that one of the differences between the MAID 2003 model and the DMT model, which *does* accurately predict σ_0 at both data points, is that the default parameter values of MAID include contributions from the S_{0+} multipole, while in standard DMT parameters it is set to zero.

5.5 Conclusion

We have shown that the none of the current pion electroproduction models accurately predict the $p(e, e'\pi^+)n$ cross section at the $\Delta(1232)$ peak consistently for all azimuthal angles at low Q^2. While all models do a reasonably good job of predicting the σ_{TT} term, MAID2003 and Sato-Lee both fail to predict σ_0, and the situation for all models with respect to σ_{LT} is at best ambiguous.

The discrepancies between the models and data occur precisely where background contributions, particularly those of the longitudinal multipoles, are expected to be most important. Combining with this observation is the fact that fairly extensive data already exist in the π^0 channel, with much lower background sensitivity, which serve to fix the resonant multipoles with some degree of confidence.

It seems therefore reasonable to conclude that the failure of all the models to predict the experimental π^+ cross sections, both at $\phi_{\pi q} = 180°$ and at $\theta^*_{\pi q} = 0°$, is due to a general misunderstanding of the longitudinal background multipoles.

While at present there is still not enough data to perform a full, model independent isospin decomposition, it is possible to close in on multipoles by fitting model parameters to the existing database. Such an effort is currently underway by members of the OOPS collaboration [52] using the of the MAID2003 model, and the $p(e, e'\pi^+)n$ data presented in this thesis will provide a significant contribution to that undertaking by constraining the background multipoles.

123

LIST OF REFERENCES

[1] S. Glashow. *Physica*, **96A**:27–30, 1979.

[2] J. Bienkowski, Z. Dziembowski, and H.J. Weber. *Phys.Rev.Lett.*, 59:624, 1987.

[3] N. Kroll and M. Ruderman. *Phys.Rev.*, **93**(1):233, 1954.

[4] J. D. Walecka. *Theoretical Nuclear and Subnuclear Physics*. Oxford University Press, New York, 1995.

[5] G. Blanpied. *Phys.Rev.Lett.*, 79:4337, 1997.

[6] R. Beck. *Physical Review*, c61:35204, 2000.

[7] D. Dreschel et al. *J.Phys.G*, **18**:449, 1992.

[8] T. Sato and T.S.H Lee. *Phys.Rev.*, **C 54** :2660, 1996.

[9] R.M Davidson and N.C Mukhopadhyay. *Phys.Lett.*, B353:131, 1995.

[10] S.M. Dolfini et al. *Phys.Rev.C*, **60**:064622–1, 2001.

[11] C. Mertz et al. *Phys. Rev. Lett.*, **86**:2963, 2001.

[12] N. Sparveris et al. *Phys.Rev.C*, **67**:058201, 2003.

[13] C. Kunz et al. *Phys.Lett.B*, **564**:21, 2003.

[14] N. Sparveris et al. *Phys.Rev.Lett.*, **94**:022003, 2005.

[15] Th. Pospischil et al. *Phys.Rev.Lett.*, **86 14** (14):2959, 2001.

[16] D. Bartsch et al. *Phys.Rev.Lett.*, **88**(14):142001, 2002.

[17] V.V. Frolov et al. *Phys.Rev.Lett.*, **82**:45, 1999.

[18] K. Joo et al. *Phys.Rev.Lett.*, **88**:122001, 2002.

[19] K. Joo et al. *Phys.Rev.C*, **68**:032201, 2003.

[20] K. Joo et al. *Phys.Rev.C*, **70**:042201, 2004.

[21] B. Mecking et al. *Nucl.Instr.Meth.*, **A503**:513, 2003.

[22] H. Egiyan et al. *Phys.Rev.C*, **73**:025204, 2006.

[23] H. Breuker et al. *Z.Phys.*, **C13**:113, 1982.

[24] H. Breuker et al. *Nucl.Phys.*, **B146**:285, 1978.

[25] E. Evangelides et al. *Nucl.Phys.*, **B71**:381, 1974.

[26] K.M. Watson. *Phys.Rev*, **85** :852, 1952.

[27] S. Eidelman et al. *Phys.Lett.*, **B 592** :1, 2004.

[28] A.S. Raskin and T.W. Donnelly. *Ann.Phys.*, **191** :78, 1989.

[29] Nikos Sparveris. *Study of the Conjecture of a deformed nucleon through the $\gamma^* N \to \Delta(1232)$ Reaction.* PhD thesis, National and Capodstrial University of Athens, 2002.

[30] Paul Bourgeois. PhD thesis, University of Massachusetts, 2005.

[31] Yoshi Sato. PhD thesis, In progress.

[32] J.C.F Mertz. *The Response Functions R_{LT} and $R_T + \varepsilon R_L$ for the $H(e,e'p)\pi^0$ Reaction at the $\Delta(1232)$ Resonance.* PhD thesis, Arizona State University, 1998.

[33] Lemmon, E.W and McLinden, M.O. and Friend,D.G. Thermophysical Properties of Fluid Systems. In E.J. Linstrom and W.G. Mallard, editors, *NIST Chemistry WebBook, NIST Standard Reference Database Number 69.* National Institute of Standards and Technology, Gaithersburg MD, 20899, June 2005. (http://webbook.nist.gov).

125

[34] C. Kunz. *Simultaneous Measurement of the R_{TL}, $R_{TL'}$ and $R_T + \varepsilon R_L$ Responses of the $H(\vec{e}, e'p)\pi^0$ Reaction in the $\Delta(1232)$ Region*. PhD thesis, Massachusetts Institute of Technology, 2000.

[35] X. Jiang. *Measurement of Interference Structure Functions in Quasielastic Proton Knock Out from ^{12}C*. PhD thesis, University of Massachusetts, 1998.

[36] S.M. Dolfini. *Measurement of the Fifth Structure Function in Deuterium* . PhD thesis, University of Illinois, 1994.

[37] J.B. Mandeville. *Measurement of the Fifth Structure Function in Quasi-Elastic Proton Knock-Out From Carbon*. PhD thesis, University of Illinois at Urbana-Champaign, 1993.

[38] Zi-Lu Zhou et al. *Nucl.Instr.Meth.*, **A 487** :365, 2002.

[39] R. Brun et al. Paw-physics analysis workstation. *CERN Program Library*, Q121.

[40] R. Brun and F. Rademakers. *Nucl.Inst.Meth.*, **A 389**:81, 1997.

[41] Costas Vellidis. AEEXB, A program for Monte Carlo simulations of coincidence electron scattering experiments. Technical report, MIT/Bates Laboratory, 1998.

[42] Costas Vellidis. The program TURTLE_JBM. Technical report, MIT/Bates Laboratory, 1996.

[43] L.W. Mo and Y-S. Tsai. *Rev.Mod.Phys.*, 41:205, 1969.

[44] S. Penner. Nuclear structure physics. In *Proceedings of the 18th Scottish University Summer School in Physics*, page 69, 1977.

[45] A. Afanasev et al. *Phys.Rev.D*, **66**:074004, 2002.

[46] D. Dreschel and L. Tiator. *Nucl.Phys*, **A645**:145, 1999.

[47] S. Agostinelli et al. *Nucl. Instrum. Meth.*, **A 506**:250, 2003.

[48] J. Friedrich and Th. Walcher. *Eur.Phys.J.*, A **17**:607, 2003.

[49] B. Povh, K. Rith, C. Scholz, and F. Zetsche. *Particles and Nuclei.* Springer-Verlag, Berlin, 2nd edition, 1999. ISBN 3-540-66115-8.

[50] H.-W. Hammer and Ulf-G. Meißner. *Eur.Phys.J. A*, **20**:469, 2004.

[51] A.M. Bernstein. private communication, 2005.

[52] S. Stave and A.M. Bernstein. Private communication, September 2005.

Appendices

APPENDIX A

Measurement of Pedestal Currents in the BIC Current Integrators

Each of the BIC current integrators used in the beam charge measurement described in section 3.2.1 introduces it's own pedestal current into the data stream. A reasonable measurement of these pedestal currents is necessary to provide accurate knowledge of the true beam charge. While these pedestal currents are adjustable, they were largely untouched during the data taking. The BIC 3 pedestal was never changed during production, so it's value is regarded as a constant for the entire data set of this experiment. The BIC 1 pedestal, on the other hand, was changed exactly once: at the beginning of Kinematics b, it was set to a small negative value in an attempt to compensate for the galvanic current. It remained at this setting for the duration of Kinematics b, and into Kinematics a. About two-thirds of the way through Kinematics a, it was suspected that the galvanic current may not be constant, but increasing with time. The BIC 1 pedestal was reset to a small positive value to simplify measurement of the galvanic current. Within each of these two periods period, $I_{\rm BIC1}$ may be considered as a constant. Determining the BIC pedestal currents requires two different methods depending on whether BIC 1 is positive or negative; the two cases are addressed separately below.

A.1 Pedestal Runs

At regular intervals during the data taking, runs were performed with no beam present for the expressed purposes of tracking pedestal currents. For these pedestal runs, the 600 Hz Mod Sync signal replaced 580 Hz beam spill pulse as the gate trigger. While the addition of 20 Hz veto charge measurement described above provided a better and more direct avenue for measuring the galvanic current, these runs were essential for isolating the BIC pedestal currents.

During a pedestal run, the charge measured by the FCG scaler is given by the sum of the galvanic current in each mod sync gate, minus the portion of the galvanic current that falls within the 500 μs veto gate width in 20 out of 600 mod sync gates and is diverted to the 20 Hz veto scaler channel (see figure A-1), plus the BIC 1 pedestal current times the total time $T_{\rm ped}$ of the pedestal run:

$$Q_{\rm FCG}^{\rm ped} = I_{\rm gv} \times (\#{\rm BG} \times \Delta T - {\rm DF}_{\rm veto} \times T_{\rm ped}) + I_{\rm BIC1} \times T_{\rm ped}\,. \qquad (A.1)$$

129

The charge collected by the 20 Hz veto scaler during a pedestal run, on the other hand, is

$$Q_{\text{veto}}^{\text{ped}} = (I_{\text{gv}} \times \text{DF}_{\text{veto}} + I_{\text{BIC3}}) \times T_{\text{ped}}.$$ (A.2)
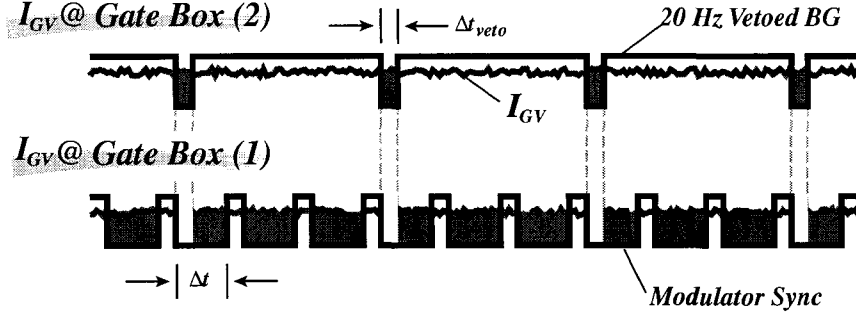
Figure A-1: During pedestal runs, a portion of the galvanic current is diverted from the FCG scaler by the 20 Hz veto.

A.2 $I_{\text{BIC1}} > 0$

The determination of the pedestal currents is simpler in the latter runs, when the BIC 1 pedestal was set to a positive value. The pedestal current is assumed to be a constant during this time period. Fluctuations are small compared to the pedestal current value, and are incorporated into the uncertainty estimate.

During this the period BIC 1 pedestal current is measured directly in the FCG scaler channel whenever a beam trip occurs in a production run. During a beam trip, the beam current drops to 0. Since there is no beam pulse coming into the gate box, no current is seen from the FC at all in the FCG scaler channel. The FCG scaler channel then records only the BIC 1 pedestal current:

$$Q_{\text{FCG}}^{\text{trip}} = I_{\text{BIC1}} \times T_{\text{trip}},$$ (A.3)

where T_{trip} is the duration of the beam trip. The BIC 1 pedestal current so measured in each available beam trip is plotted in figure A-2. A constant value is fitted to the data, yielding a value of

$$I_{\text{BIC1}} = 0.155 \pm 0.0039 \mu\text{A}.$$ (A.4)

The uncertainty is taken from the spread of the data about the fit.

130
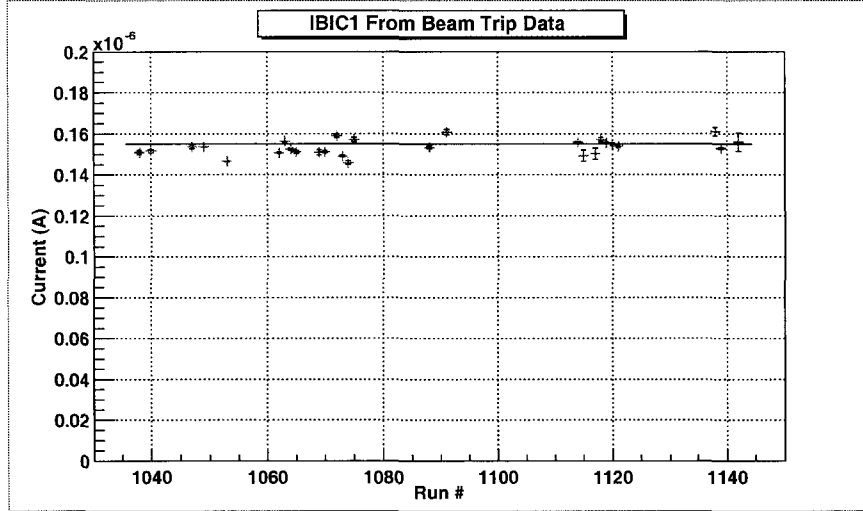
Figure A-2: Fit of I_{BIC1} to high precision beam-trip measurements.

With I_{BIC1} determined for this portion of the data, the pedestal runs can now be used to determine the BIC 3 pedestal current. First, we use the known value of of I_{BIC1} to extract the galvanic current during each pedestal run by solving equation A.1 for I_{gv}:

$$I_{gv} = \frac{Q_{FCG}^{ped} - I_{BIC1} \times T_{ped}}{\#BG \times \Delta T - DF_{veto} \times T_{ped}} .$$ (A.5)

For each pedestal run, the BIC 3 pedestal can now also be obtained from the 20 Hz Veto channel by rearranging equation A.2:

$$I_{BIC3} = \frac{Q_{veto}^{ped}}{T_{ped}} - I_{gv} \times DF_{veto} .$$ (A.6)

These are plotted in figure A-3. The weighted average of these measurements is roughly 1.6 nA, with an RMS spread of 0.09 nA. This is just a preliminary value, as more data points will be added in the next section.

131
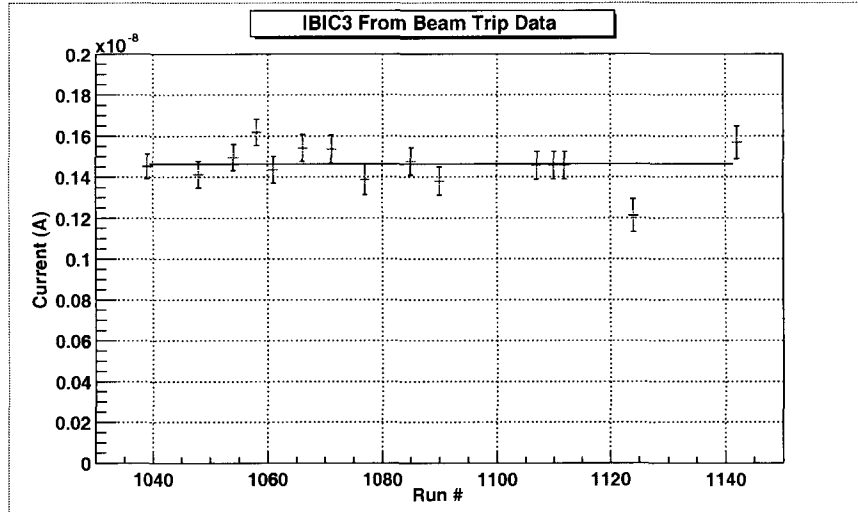
Figure A-3: Fit of I_{BIC3} to values calculated using beam-trip data in the later production runs.

A.3 $I_{\mathrm{BIC1}} < 0$

In the earlier data runs, the BIC 1 current is set below zero and cannot be measured directly during beam trips, as the scalers used to record the current do not register a negative value. Instead, the Hewlett-Packard (HP) current monitor is used to determine the galvanic current during each pedestal run in this part of the data set.

The visual scaler readout of the HP current monitor displayed the total current output of the Faraday cup. This also allowed the galvanic current to be observed directly, albeit at low precision ($\sim 5\%$), and only immediately after the beam is turned off. This was possible because I_{gv} decayed with at comparatively long RC time constant. While the HP monitor was not particularly helpful in determining I_{gv} during production runs, it did prove useful for evaluating the BIC pedestals. The visual readout of the HP monitor was recorded in the logbook for most pedestal runs after it was installed, near the end of Kinematics b.

Because the use of the HP monitor overlapped with a portion of the runs for which the BIC 1 current was positive, it was possible to calibrate the HP monitor against a subset of the high-precision I_{gv} measurements described in section A.2. A plot of those I_{gv} measurements versus the HP current monitor readings is shown in figure A-4. A linear calibration function of

$$I_{\mathrm{gv}} = 0.9877 \times I_{\mathrm{HP}} - 1.51 \times 10^{-8} \tag{A.7}$$

The error in the galvanic current measured by the calibrated HP monitor is taken to be $\pm 0.045 \ \mu\mathrm{A}$, based on the spread of the data.
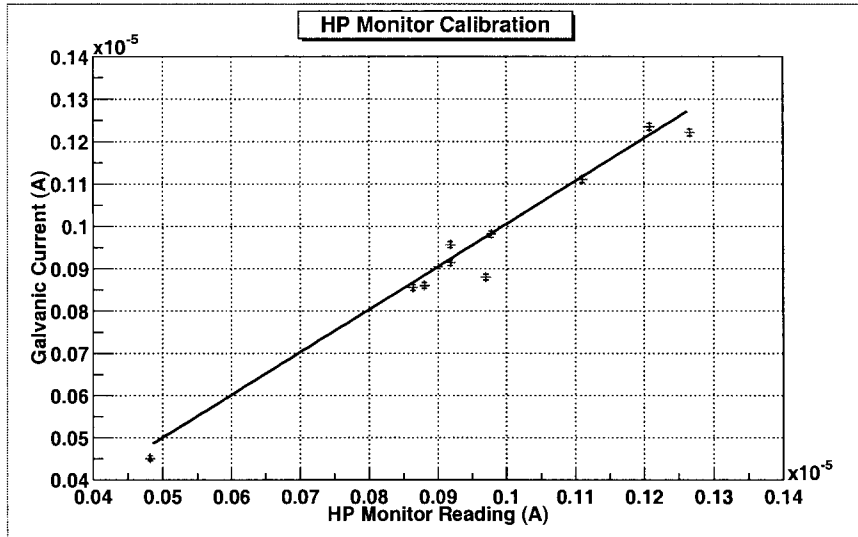
Figure A-4: Calibration of the HP monitor measurements from pedestal run data.

The values of I_{gv} obtained with the HP monitor at each pedestal run in this portion of the data are then used to calculate the BIC 3 pedestals during each pedestal run using equation A.6. These are shown in figure A-5, along with I_{BIC3} data points determined in section A.2.
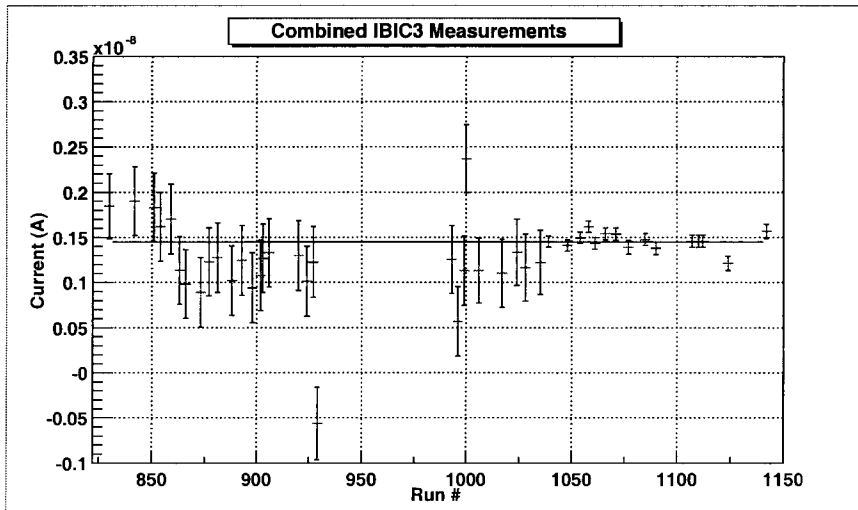
Figure A-5: Fit to I_{BIC3} global data set, including measurements calculated using HP-monitor as well as beam trip data.

Note the uncertainty in the data points determined in this section is much larger; nevertheless, the data show consistency with the constant value determined by the other method. A fit to the entire I_{BIC3} data set yields

$$I_{BIC3} = 1.45 \pm 0.040 \, \text{nA} , \tag{A.8}$$

133

in excellent agreement with the preliminary fit.

Using this now as a global value for I_{BIC3}, and using the HP monitor measurements of the galvanic current, the BIC 1 pedestal values for this portion of the data set can be calculated in each pedestal run from the FCG scaler channel. Rearranging equation A.1 for I_{BIC1}:

$$I_{BIC1} = \frac{Q_{FCG}^{ped} - I_{gv} \times (\#BG \times \Delta T - DF_{veto} \times T_{ped})}{T_{ped}}. \tag{A.9}$$

The values so calculated for I_{BIC1} are plotted in figure A-6. Again, the accuracies are considerably worse than by the method in section ??.
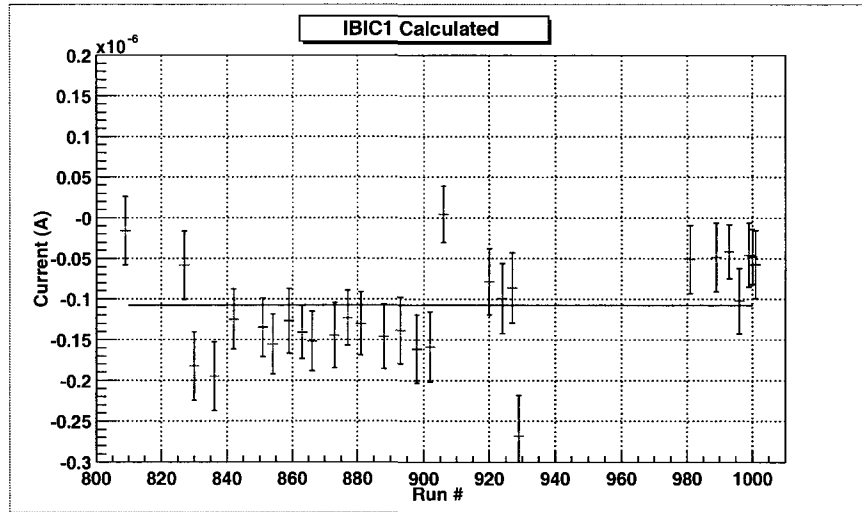
Figure A-6: Fit of I_{BIC1} to values calculated using the HP-monitor readings in the earlier production runs.

The BIC 1 pedestal is considered to be a constant over this portion of the data; a fit yields

$$I_{BIC1} = -83 \pm 42\,nA, \tag{A.10}$$

The 50% relative uncertainty here is not problematic, since the BIC 1 pedestal is small compared to the galvanic current ($\sim 8\%$), and even smaller compared to the beam current ($\sim 0.9\%$), so this only contributes roughly 0.5 % to the final cross section uncertainties, and only for those runs in this portion of the data.

134

APPENDIX B

TURTLE Models for AEEXB Monte-Carlo

B.1 The OHIPS TURTLE Model

```
(This is a TURTLE deck for Joe Mandeville's version of the program.)
(DESIGN-MOMENTUM 0.2691)

(This is an OHIPS module deck which is presumably used as one spectrometer)
(in a coincident simulation.)
(It is in the HIGH RESOLUTION or NORMAL MODE, which is defined by -Q +Q)
(The LOW RESOLUTION or HIGH THETA ACCEPTANCE mode is defined by +Q -Q)

(This file is derived from the following sources:)
( 1: Thesis of Robert Steven Turley Feb 1984      )
( 2: A drawing file of Dave Costa depicting the design OHIPS detection system)
( 3: Dan Tiegers 1.77M OHIPS Turtle file           )

(Use second order optics and enforce apertures in the magnets.)
 SECOND     ON
 APERTURES ON

 SHIFT 0. 0. -0.1 0. 0. 0.   (Target Shifts for VCS and N->D)

(Write the target coordinates to the output file.)
(This is detector card 01, at the VERTEX)
 DETECTOR

(Shift any target positions here.  E.g., shift y for an offset beam spot.)
(SHIFT 0. 0. 0. 0. 0. 0.)

(Drift to the LH2 target cell wall)
 DRIFT 0.008

(multiple scattering in LH2: 0.8 cm of LH2 / L_r = 866 cm)
```

135

(MULTIPLE-SCATTER   1.0   0.511   0.000925)
(ENERGY-LOSS-TARGET 1.0   0.511   1.0   1.008   0.05664 0.05664)

(multiple scattering on Havar foil: L/L_r = 10.16 um / 1.76 cm)
 MULTIPLE-SCATTER   1.0   0.511   0.00029
 ENERGY-LOSS-TARGET 1.0   0.511   30.73   68.9245   0.0037   0.0037

(multiple scattering in N2 frost: L//L_r = 0.5 cm / 37.0273)
(MULTIPLE-SCATTER   1.0   0.511   0.0135)
(ENERGY-LOSS-TARGET 1.0   0.511   7.0   14.00 1.026 0.513 0.513)

(Drift to the target chamber window)
 DRIFT 0.246
(scattering chamber window = 0.0127 cm kapton + 0.0305 cm kevlar)
(Mylar (very similar to kapton/kevlar) L_r = 30.5536 cm)
 MULTIPLE-SCATTER   1.0   0.511   0.0014
 ENERGY-LOSS-TARGET 1.0   0.511   6.0   12.0   0.06   0.06

(this is just for a necessary TURTLE propagation)
 DRIFT 0.001

(--------OHIPS Sieve Slit Apertures---------)
 DRIFT 1.25154   (drift distance to OHIPS sieve slit)

(Drift through Sieve Slit, 2.54 cm thick)
 DRIFT 0.0254
(Write out Sieve Slit histograms)
(DETECTOR)

(drift dist. between scattering chamber window and OHIPS window: 127.794cm)
(multiple scattering in Air: 127.794 cm Air / L_r = 30423 cm)
 MULTIPLE-SCATTER   1.0   0.511   0.004201
(Energy loss due to O2)
(O2 is 21% of volume of Air)
(ENERGY-LOSS-TARGET 1.0   0.511   8.0 16.0   0.00024 0.03062   0.03062)
(Energy loss due to N2)
(O2 is 79% of volume of Air)
(ENERGY-LOSS-TARGET 1.0   0.511   7.0 14.0   0.00064 0.08179   0.08179)

(spectrometer entrance window)
(0.0127 cm kapton / 30.5536 cm L_r)
 MULTIPLE-SCATTER   1.0   0.511   0.000415
 ENERGY-LOSS-TARGET 1.0   0.511   6.0   12.0   0.018   0.018

(vacuum to quads collimator --- Tieger collimator)
(DRIFT 1.311)

136

(vacuum to quads collimator --- Vellidis collimator)
(DRIFT 1.152)
(vacuum to quads collimator --- Short N-Delta Drift)
(DRIFT 0.9153)
(vacuum to quads collimator --- Long N-Delta Drift)
(DRIFT 1.3153)
(drift dist. between Sieve Slit and Collimator)
 DRIFT 0.0384

(--- Front collimator window ---)
(info from Jeff Shaw - 16 Jul 1998)
(The half-vertical acceptance is 3.4033 in. = 8.6444 cm)
 RECTANGULAR-SLIT 1 8.6444

(The half-horizontal acceptance with   inserts is 1.081 in. = 2.7457 cm)
(The half-horizontal acceptance without inserts is 3.75 cm)
 RECTANGULAR-SLIT 3 3.75
(RECTANGULAR-SLIT 3 2.7457)

(--- 19.255 cm thickness ---)
 DRIFT   0.19255

(--- Rear collimator window ---)
(info from Jeff Shaw - 16 Jul 1998)
(The half-vertical acceptance is 3.8411 in. = 9.7563 cm)
 RECTANGULAR-SLIT 1 9.7563

(The half-horizontal acceptance with   inserts is 1.3043 in. = 3.3128 cm)
(The half-horizontal acceptance without inserts is 4.3 cm)
 RECTANGULAR-SLIT 3 4.3
(RECTANGULAR-SLIT 3 3.3128)
(This is Detector Card 02, at the QUAD entrance)
 DETECTOR

(--- O H I P S   F I R S T   Q U A D R U P O L E   ---)
(drift to the entrance of the first quad)
 DRIFT 0.2406
(vacuum pipe)
 ELLIPTICAL-SLIT 1.   13.97   3.   13.97
(negative field for "high resolution" mode)
(---- NEG field for "normal"   mode)
(QUADRUPOLE 0.708 -1.65012 15.24)
(---- POS field for "reverse" mode)
(QUADRUPOLE 0.708 1.86913   15.24)   (Original value)
 QUADRUPOLE 0.708 1.8400   15.24

(--- O H I P S   S E C O N D   Q U A D R U P O L E   ---)
(drift to the entrance of the second quad)

137

```
DRIFT 0.1307
(vacuum pipe)
 ELLIPTICAL-SLIT  1.   13.97   3.   13.97
(positive field for "high resolution"  mode)
( ---- POS field for "normal"  mode)
(QUADRUPOLE 0.708  0.63626 15.24)
( ---- NEG field for "reverse"  mode)
(QUADRUPOLE 0.708  -1.80225   15.24)   (Original value)
QUADRUPOLE 0.708  -1.705  15.24 (JMK N-Delta tune BEST)


(vacuuum pipe)
 ELLIPTICAL-SLIT  1.   13.97   3.   13.97
 DRIFT 0.262175
(transition piece)
 RECTANGULAR-SLIT 1 20.32
 RECTANGULAR-SLIT 3 9.525


( ---  O H I P S  D I P O L E  --- )
(drift to the entrance of the dipole)
 DRIFT 0.2508
(vacuum pipe)
 RECTANGULAR-SLIT 1 21.2725
 RECTANGULAR-SLIT 3 9.6043
(Give the dipole vertical and horizontal width/2.)
(The subsequent slits are more restrictive, so these are effectively ignored.)
 DIPOLE-APERTURE 20.32,9.6043
(See the TURTLE manual for fringe fields; this is unclamped Rogowski.)
 POLE-FACE-ROTATION 0.0
 FRINGE-FIELD 0.7,4.4
(dipole field)
(DIPOLE    3.     3.5339  0.0)   (Old Tune)
DIPOLE    3.     3.458  0.0


(vacuum pipe)
 RECTANGULAR-SLIT 1 20.32
 RECTANGULAR-SLIT 3 9.6043
(clamped Rogowski)
 POLE-FACE-ROTATION  0.0
 FRINGE-FIELD 0.4,4.4
(DIPOLE     0.9898 3.5339  0.0)   (Old Tune)
 DIPOLE     0.9898 3.4580  0.0


 POLE-FACE-ROTATION  0.0
(vacuum pipe)
 RECTANGULAR-SLIT 1 20.32
 RECTANGULAR-SLIT 3 9.6043


(Drift 1.626 m to the center of the focal plane)
```

138

```
(DRIFT 1.626)
 DRIFT 0.534
(vacuum pipe)
 RECTANGULAR-SLIT  1 38.1
 RECTANGULAR-SLIT  3 8.6
 DRIFT 0.457

 ARBITRARY-MATRIX /home/johnk/AEEXB/tur/arbitrary_matrix.mat

(vacuum pipe)
 RECTANGULAR-SLIT  1 38.1
 RECTANGULAR-SLIT  3 15.3

( ---  O H I P S   D E T E C T O R   S Y S T E M  --- )

(vdcx)
( Wire chamber --VDC 1-- Bottom Window, Low momentum side )
(DRIFT 0.32518)
 DRIFT 0.2758
 OFFSET-RECTANGULAR-SLIT 1    -32.3289   1000
 RECTANGULAR-SLIT 3 12.7

(drift dist. from VDC1 bottom window to VDC2 bottom window Low mom. side )
 DRIFT 0.211141
 OFFSET-RECTANGULAR-SLIT 1    -31.8198   1000
 RECTANGULAR-SLIT 3 15.0

(drift dist. from VDC2 bottom window low mom side to vacuum box window)
 DRIFT 0.035818

(multiple scattering on vacuum box exit window)
(0.0127 cm kapton / 30.5536 cm L_r)
 MULTIPLE-SCATTER   1.0  0.511  0.000415
 ENERGY-LOSS-TARGET 1.0  0.511  6.0  12.0 0.018  0.018

(drift dist. from vacuum box window to VDC1 entrance window: 8.531 cm)
 DRIFT 0.08531

(multiple scattering in Air: 8.531 cm Air / L_r = 30423 cm)
 MULTIPLE-SCATTER   1.0  0.511  0.000280
(Energy loss due to O2)
(O2 is 21% of volume of Air)
 ENERGY-LOSS-TARGET 1.0  0.511  8.0 16.0  0.00205  0.00205
(Energy loss due to N2)
(N2 is 79% of volume of Air)
 ENERGY-LOSS-TARGET 1.0  0.511  7.0 14.0  0.00546  0.00546

(multiple scattering on VDC1 entrance window)
```

```
(0.0707 cm mylar / 28.7 cm L_r)
 MULTIPLE-SCATTER    1.0   0.511   0.00246
 ENERGY-LOSS-TARGET 1.0   0.511   6.0 12.0 0.09827 0.09827


(drift dist. from VDC1 entrance window to U1 bottom volt. plane: 1.796 cm)
 DRIFT 0.01796


(multiple scattering on U1 bottom voltage mylar plane)
(0.00072 cm mylar / 28.7 cm L_r)
 MULTIPLE-SCATTER    1.0   0.511   0.000025
 ENERGY-LOSS-TARGET 1.0   0.511   6.0 12.0 0.001 0.001


(multiple scattering on Ar gas)
(1.796 cm Argon / (14004 cm L_r * 2))
(Argon occupies 50% the volume of VDC1)
 MULTIPLE-SCATTER    1.0   0.511 0.000064
 ENERGY-LOSS-TARGET 1.0   0.511 18.0 39.9 0.001254 0.001254


(multiple scattering on IsoButane gas)
(1.796 cm IsoButane / (16930 cm L_r * 2))
(IsoB occupies 50% the volume of VDC1)
 MULTIPLE-SCATTER    1.0   0.511 0.000053
 ENERGY-LOSS-TARGET 1.0   0.511 6.0 12.0 0.002398 0.002398


(drift dist. from U1 bottom volt. plane to U1 wire plane: 1.796 cm)
(The U1 plane is defined as the OHIPS Chamber Coordinate Plane)
 DRIFT 0.01796


(multiple scattering on Ar gas)
(1.796 cm Argon / (14004 cm L_r *2))
(Argon occupies 50% the volume of VDC1)
 MULTIPLE-SCATTER    1.0   0.511 0.000064
 ENERGY-LOSS-TARGET 1.0   0.511 18.0 39.9 0.001254 0.001254


(multiple scattering on IsoButane gas)
(1.796 cm IsoButane / (16930 cm L_r * 2))
(IsoB occupies 50% the volume of VDC1)
 MULTIPLE-SCATTER    1.0   0.511 0.000053
 ENERGY-LOSS-TARGET 1.0   0.511 6.0 12.0 0.002398 0.002398


( Decector Card 03 --- The U1 Chamber Coordinate Plane --- )
 DETECTOR 45.0 0.02 3.0 0.02 3.0


(drift dist. from U1 wire plane to U1 top volt. plane: 1.796 cm)
 DRIFT 0.01796


(multiple scattering on U1 top voltage mylar plane)
(0.00072 cm mylar / 28.7 cm L_r)
```

```
MULTIPLE-SCATTER    1.0   0.511   0.000025
ENERGY-LOSS-TARGET 1.0   0.511   6.0  12.0   0.001 0.001


(multiple scattering on Ar gas)
(1.796 cm Argon / (14004 cm L_r * 2))
(Argon occupies 50% the volume of VDC1)
 MULTIPLE-SCATTER    1.0   0.511 0.000064
 ENERGY-LOSS-TARGET 1.0   0.511 18.0 39.9 0.001254 0.001254


(multiple scattering on IsoButane gas)
(1.796 cm IsoButane / (16930 cm L_r * 2))
(IsoB occupies 50% the volume of VDC1)
 MULTIPLE-SCATTER    1.0   0.511 0.000053
 ENERGY-LOSS-TARGET 1.0   0.511 6.0  12.0 0.002398 0.002398


(drift dist. from U1 top volt. plane to V1 bottom volt. plane: 1.796 cm)
 DRIFT 0.01796


(multiple scattering on V1 bottom voltage mylar plane)
(0.00072 cm mylar / 28.7 cm L_r)
 MULTIPLE-SCATTER    1.0   0.511   0.000025
 ENERGY-LOSS-TARGET 1.0   0.511   6.0  12.0 0.001 0.001


(multiple scattering on Ar gas)
(1.796 cm Argon / (14004 cm L_r * 2))
(Argon occupies 50% the volume of VDC1)
 MULTIPLE-SCATTER    1.0   0.511 0.000064
 ENERGY-LOSS-TARGET 1.0   0.511 18.0 39.9 0.001254 0.001254


(multiple scattering on IsoButane gas)
(1.796 cm IsoButane / (16930 cm L_r * 2))
(IsoB occupies 50% the volume of VDC1)
 MULTIPLE-SCATTER    1.0   0.511 0.000053
 ENERGY-LOSS-TARGET 1.0   0.511 6.0  12.0 0.002398 0.002398


(drift dist. from V1 bottom volt. plane to V1 top volt. plane: 3.592 cm)
 DRIFT 0.03592


(multiple scattering on V1 top voltage mylar plane)
(0.00072 cm mylar / 28.7 cm L_r)
 MULTIPLE-SCATTER    1.0   0.511   0.000025
 ENERGY-LOSS-TARGET 1.0   0.511   6.0  12.0 0.001 0.001


(multiple scattering on Ar gas)
(3.592 cm Argon / (14004 cm L_r * 2))
(Argon occupies 50% the volume of VDC1)
 MULTIPLE-SCATTER    1.0   0.511 0.000064
 ENERGY-LOSS-TARGET 1.0   0.511 18.0 39.9 0.002507 0.002507
```

(multiple scattering on IsoButane gas)
(3.592 cm IsoButane / (16930 cm L_r * 2))
(IsoB occupies 50% the volume of VDC1)
 MULTIPLE-SCATTER   1.0   0.511 0.000053
 ENERGY-LOSS-TARGET 1.0   0.511 6.0 12.0 0.004795 0.004795

(drift dist. from V1 top volt. plane to VDC1 exit window: 1.796 cm)
 DRIFT 0.01796

(multiple scattering on Ar gas)
(1.796 cm Argon / (14004 cm L_r * 2))
(Argon occupies 50% the volume of VDC1)
 MULTIPLE-SCATTER   1.0   0.511 0.000064
 ENERGY-LOSS-TARGET 1.0   0.511 18.0 39.9 0.001254 0.001254

(multiple scattering on IsoButane gas)
(1.796 cm IsoButane / (16930 cm L_r * 2))
(IsoB occupies 50% the volume of VDC1)
 MULTIPLE-SCATTER   1.0   0.511 0.000053
 ENERGY-LOSS-TARGET 1.0   0.511 6.0 12.0 0.002398 0.002398

(multiple scattering on VDC1 exit window)
(0.0707 cm mylar / 28.7 cm L_r)
 MULTIPLE-SCATTER   1.0   0.511 0.00246
 ENERGY-LOSS-TARGET 1.0   0.511 6.0 12.0 0.09827 0.09827

(multiple scattering on Air between VDC1 and VDC2)
(7.633 cm air / 30420 L_r)
 MULTIPLE-SCATTER 1.0 0.511 0.00025

(drift dist. VDC1 exit window to VDC2 entrance window: 7.633 cm)
 DRIFT 0.07633

(multiple scattering on VDC2 entrance window)
(0.0707 cm mylar / 28.7 cm L_r)
 MULTIPLE-SCATTER   1.0   0.511 0.00246
 ENERGY-LOSS-TARGET 1.0   0.511 6.0 12.0 0.09827 0.09827

(drift dist. from VDC2 entrance window to U2 bottom volt. plane: 2.3723 cm)
 DRIFT 0.023723

(multiple scattering on U2 bottom volt. plane)
(0.0707 cm mylar / 28.7 cm L_r)
 MULTIPLE-SCATTER   1.0   0.511 0.00246
 ENERGY-LOSS-TARGET 1.0   0.511 6.0 12.0 0.172 0.172

(multiple scattering on Ar gas)

142

(2.3723 cm Argon / (14004 cm L_r *2))
(Argon occupies 50% the volume of VDC2)
 MULTIPLE-SCATTER   1.0   0.511 0.000085
 ENERGY-LOSS-TARGET 1.0   0.511 18.0 39.9 0.001656 0.001656

(multiple scattering on IsoButane gas)
(2.3723 cm IsoButane / (16930 cm L_r * 2))
(IsoB occupies 50% the volume of VDC1)
 MULTIPLE-SCATTER   1.0   0.511 0.000070
 ENERGY-LOSS-TARGET 1.0   0.511 6.0 12.0 0.003167 0.003167

(drift dist. from U2 bottom volt. plane to U2 wire plane: 1.6688 cm)
 DRIFT 0.016688

(multiple scattering on Ar gas)
(1.6688 cm Argon / (14004 cm L_r * 2))
(Argon occupies 50% the volume of VDC2)
 MULTIPLE-SCATTER   1.0   0.511 0.000060
 ENERGY-LOSS-TARGET 1.0   0.511 18.0 39.9 0.001165 0.001165

(multiple scattering on IsoButane gas)
(1.6688 cm IsoButane / (16930 cm L_r *2))
(IsoB occupies 50% the volume of VDC1)
 MULTIPLE-SCATTER   1.0   0.511 0.000049
 ENERGY-LOSS-TARGET 1.0   0.511 6.0 12.0 0.002228 0.002228

(Detector Caard 04 --- The U2 Chamber Coordinate Plane ---)
 DETECTOR 45. 0.02 0.0 0.02 0.0

(drift dist. from U2 plane to VDC2 exit window)
 DRIFT 0.114198

(drift dist. from VDC2 exit window to VDC1 exit window high momentum side)
 DRIFT 0.225839
 OFFSET-RECTANGULAR-SLIT 1   -1000 32.3289

(drift dist. from VDC1 exit window to VDC2 exit window High moment side)
 DRIFT 0.06217
 OFFSET-RECTANGULAR-SLIT 1   -1000 32.778

(Scintillator --S2--)
 DRIFT 0.079475
 RECTANGULAR-SLIT 1 34.29
 RECTANGULAR-SLIT 3 11.43

(The Cerenkov detector)
 DRIFT 0.047625
 RECTANGULAR-SLIT 1 61.27750

143

```
RECTANGULAR-SLIT 3 23.8125
DRIFT 0.71999
RECTANGULAR-SLIT 1 61.27750
RECTANGULAR-SLIT 3 23.8125
DRIFT 0.08573
RECTANGULAR-SLIT 1 61.27750
RECTANGULAR-SLIT 3 23.8125


( Scintillator --S3-- )
 DRIFT 0.0308925
 RECTANGULAR-SLIT 1 45.72
 RECTANGULAR-SLIT 3 12.7

(Put a detector card here to see if particles make it this far.)
(Detector Card 05 Call this the trigger.)
 DETECTOR

( PbG )
( DRIFT 0.1539875)
( RECTANGULAR-SLIT 1 48.10252)
( RECTANGULAR-SLIT 3 12.5)
( DRIFT 0.20955)
( RECTANGULAR-SLIT 1 48.10252)
( RECTANGULAR-SLIT 3 12.5)
```

B.2 The OOPS TURTLE Model

```
(This is a TURTLE deck for Joe Mandeville's version of the program.)
(DESIGN-MOMENTUM 0.625)


(This is an OOPS module deck which is presumably used as one spectrometer)
(in a coincident simulation.)


(Use second order optics and enforce apertures in the magnets.)
SECOND ON
APERTURES ON
(Give the dipole vertical and horizontal width/2.)
(Following slits are more restrictive, so these are effectively ignored.)
DIPOLE-APERTURE 15.24,4.1275
(See the TURTLE manual for fringe fields; this is unclamped Rogowski.)
FRINGE-FIELD .7,4.4


(Write the target coordinates to the output file.)
 DETECTOR
(Shift any target positions here.  E.g., shift y for an offset beam spot.)
(SHIFT 0. 0. 0. 0. 0. 0.)


(Drift to the LH2 target cell wall)
DRIFT 0.008
(multiple scattering in LH2: 0.8 cm of LH2 / L_r = 866 cm)
 (MULTIPLE-SCATTER   1.0   139.57   0.000925)
 (ENERGY-LOSS-TARGET 1.0   139.57   1.0   1.008   0.05664 0.05664)


(multiple scattering on Havar foil: L/L_r = 10.16 um / 1.76 cm)
 MULTIPLE-SCATTER   1.0   139.57   0.00029
 ENERGY-LOSS-TARGET 1.0   139.57   30.73   68.9245   0.0037   0.0037


(Drift to the target chamber window)
DRIFT 0.254


(scattering chamber window = 0.0127 cm kapton + 0.0305 cm kevlar)
(       ---   charge, mass [MeV], L/L_r)
( Kapton dens = 1.42 )
( CH2    dens = 0.92 -- 0.95 g/cm^3  L_r = 44.8 g/cm^2  )
( air                             L_r = 30420 cm     )
( Mylar (very similar to kapton/kevlar) L_r = 30.5536 cm)
MULTIPLE-SCATTER   1.0   139.57   0.0014
ENERGY-LOSS-TARGET 1.0   139.57   6.0   12.0   0.06   0.06


(this is just for a necessary TURTLE propagation)
DRIFT 0.001


( spectrometer entrance window )
```

145

```
(0.0127 cm kapton / 30.5536 cm L_r)
MULTIPLE-SCATTER    1.0   139.57   0.000415
ENERGY-LOSS-TARGET 1.0   139.57   6.0   12.0   0.018   0.018

(Drift through vacuum)
DRIFT 1.0423

(air--multiple scattering)
(MULTIPLE-SCATTER    1.0   139.57   0.0034)
(ENERGY-LOSS-TARGET 1.0   139.57   7.0   14.0   0.126   0.126)

(The vertical acceptance of the front collimator during the Feb. 1991)
(test run is used below.  This corresponds to an aperture of +-31mr)
(in theta_target.)
(RECTANGULAR-SLIT 1   4.1778)
 RECTANGULAR-SLIT 1   4.1656
(With the collimator insert used for the data cycle later in the spring)
(of 1991, the acceptance in theta_target was reduced to +-25 mr.)
(RECTANGULAR-SLIT 1   3.24075)
(The horizontal acceptance is +-12 mr.)
 RECTANGULAR-SLIT 3   1.5634
 DETECTOR

(Drift to the effective field boundary of the dipole somewhere inside)
(the front collimator.)
 DRIFT .058958

(O O P S   D I P O L E)
(Model the OOPS dipole.  The total distance is 1.317366 m, and the field)
(is 6 kG.  We have partioned the dipole into many parts to include the)
(baffles as slits.)
(beginning of dipole field inside front collimator)
OFFSET-RECTANGULAR-SLIT 1      -4.22              4.17
POLE-FACE-ROTATION             12.8616
Dipole                         0.059959      6.0        0.00000
(end of top of front collimator)
OFFSET-RECTANGULAR-SLIT 1      -4.36              +4.40
OFFSET-RECTANGULAR-SLIT 3      -1.72              +1.72
Dipole                         0.018385      6.0        0.00000
(end of bottom of front collimator)
OFFSET-RECTANGULAR-SLIT 1      -7.30              +4.50
Dipole                         0.284477      6.0        0.00000
(1st top baffle)
OFFSET-RECTANGULAR-SLIT 1      -6.10              +11.23
Dipole                         0.068472      6.0        0.00000
(2nd top baffle)
OFFSET-RECTANGULAR-SLIT 1      -6.33              +10.45
Dipole                         0.081898      6.0        0.00000
```

```
(1st bottom baffle, 3rd top baffle)
OFFSET-RECTANGULAR-SLIT 1    -6.61        +6.46
Dipole                       0.070855     6.0        0.00000
(2nd bottom baffle)
OFFSET-RECTANGULAR-SLIT 1    -11.39       +6.67
Dipole                       0.038675     6.0        0.00000
(4th top baffle)
OFFSET-RECTANGULAR-SLIT 1    -6.90        +8.11
Dipole                       0.020247     6.0        0.00000
(3rd bottom baffle)
OFFSET-RECTANGULAR-SLIT 1    -8.18        +6.89
Dipole                       0.050833     6.0        0.00000
(4th bottom baffle)
OFFSET-RECTANGULAR-SLIT 1    -11.28       +7.03
Dipole                       0.044326     6.0        0.00000
(5th top baffle, 5th bottom baffle)
OFFSET-RECTANGULAR-SLIT 1    -7.31        +7.17
Dipole                       0.040070     6.0        0.00000
(6th bottom baffle)
OFFSET-RECTANGULAR-SLIT 1    -9.11        +7.28
Dipole                       0.037596     6.0        0.00000
(7th bottom baffle)
OFFSET-RECTANGULAR-SLIT 1    -11.07       +7.40
Dipole                       0.036304     6.0        0.00000
(8th bottom baffle)
OFFSET-RECTANGULAR-SLIT 1    -12.90       +7.51
Dipole                       0.022248     6.0        0.00000
(6th top baffle)
OFFSET-RECTANGULAR-SLIT 1    -7.66        +8.34
Dipole                       0.013061     6.0        0.00000
(9th bottom baffle)
OFFSET-RECTANGULAR-SLIT 1    -8.27        +7.63
Dipole                       0.035989     6.0        0.00000
(10th bottom baffle)
OFFSET-RECTANGULAR-SLIT 1    -9.94        +7.73
Dipole                       0.037747     6.0        0.00000
(11th bottom baffle)
OFFSET-RECTANGULAR-SLIT 1    -11.62       +7.83
Dipole                       0.041258     6.0        0.00000
(7th top baffle, 12th bottom baffle)
OFFSET-RECTANGULAR-SLIT 1    -8.07        +7.96
Dipole                       0.046455     6.0        0.00000
(13th bottom baffle)
OFFSET-RECTANGULAR-SLIT 1    -10.05       +8.08
Dipole                       0.055635     6.0        0.00000
(14th bottom baffle)
OFFSET-RECTANGULAR-SLIT 1    -12.31       +8.27
Dipole                       0.070104     6.0        0.00000
```

147

(15th bottom baffle)
OFFSET-RECTANGULAR-SLIT 1   -12.05   +8.45
Dipole   0.142960   6.0   0.00000
POLE-FACE-ROTATION   8.8616
(end of dipole field -- still inside vaccum box)
OFFSET-RECTANGULAR-SLIT 1   -10.15   +12.98

(The end of the rear flange of the dipole vacuum box)
DRIFT .089060
(ELLIPTICAL-SLIT 1   8.62   3   8.62)
ELLIPTICAL-SLIT 1   12.192   3   12.192
(RECTANGULAR-SLIT 3   3.33248)
RECTANGULAR-SLIT 3   3.33375

DRIFT .012692
(A circular lead collimator between the dipole and quad kills)
(bad rays before they enter the quad.)
(The front of the ring collimator)
(ELLIPTICAL-SLIT 1   8.62   3   8.62)
ELLIPTICAL-SLIT 1   8.89   3   8.89

DRIFT .063492
(The end of the ring collimator)
(ELLIPTICAL-SLIT 1   8.62   3   8.62)
ELLIPTICAL-SLIT 1   8.89   3   8.89

(The dipole-quad distance for the North Hall OOPS is slightly shorter)
(than the design value. This is presumably taken up here in the bellows.)
(DRIFT .049446)
(DRIFT .039446   --This is the value for the North Hall OOPS)
DRIFT .039446
(The beginning of the quad pipe. This is the end of the <7" diameter)
(region; the pipe inner diameter is <8".)
(ELLIPTICAL-SLIT 1   8.62   3   8.62)
ELLIPTICAL-SLIT 1   9.9949   3   9.9949

DRIFT .048804

(O O P S   Q U A D R U P O L E)
(Model the OOPS quadrupole. The total length is .6925 m.)
(The dipole/quad field ratio for the Feb. 1991 test run is 1.185027.)
(The dipole/quad field ratio for the OOPS design is 1.185972. Note that)
(this slightly changes the design field -- 5.063176 -- to 5.05914.)
(QUADRUPOLE .115417 4.75 9.995)
(QUADRUPOLE .115417 4.85 9.995)
(QUADRUPOLE .115417 4.85 9.995)
(QUADRUPOLE .115417 4.85 9.995)
(QUADRUPOLE .115417 4.85 9.995)

(QUADRUPOLE .115417 4.85 9.995)
(QUADRUPOLE .115417 4.85 9.995)

QUADRUPOLE .115417 5.05914 9.995
QUADRUPOLE .115417 5.05914 9.995
QUADRUPOLE .115417 5.05914 9.995
QUADRUPOLE .115417 5.05914 9.995
QUADRUPOLE .115417 5.05914 9.995
QUADRUPOLE .115417 5.05914 9.995
DRIFT .123635
(The end of the quad vacuum pipe)
ELLIPTICAL-SLIT 1 9.995 3 9.995

DRIFT .076215
(The front edge of the OOPS rear vacuum collimator)

(The lead plate number 6)
RECTANGULAR-SLIT 1 6.8707
RECTANGULAR-SLIT 3 11.430
DRIFT 0.04445

(The lead plate number 5)
RECTANGULAR-SLIT 1 6.4389
RECTANGULAR-SLIT 3 11.9253
DRIFT 0.04445

(The lead plate number 4)
RECTANGULAR-SLIT 1 6.0007
RECTANGULAR-SLIT 3 12.433
DRIFT 0.04445

(The lead plate number 3)
RECTANGULAR-SLIT 1 5.5753
RECTANGULAR-SLIT 3 12.9413
DRIFT 0.04445

(The lead plate number 2)
RECTANGULAR-SLIT 1 5.1943
RECTANGULAR-SLIT 3 13.4493
DRIFT 0.04445

(The lead plate number 1)
RECTANGULAR-SLIT 1 3.7503
RECTANGULAR-SLIT 3 12.9286
DRIFT 0.0381

(The back side of plate number 1)
RECTANGULAR-SLIT 1 3.7503

RECTANGULAR-SLIT 3 12.9286

(The rear window flange of the quad vacuum box extension)
DRIFT .052507
RECTANGULAR-SLIT 1 5.08
RECTANGULAR-SLIT 3 17.78

(multiple scattering on exit window)
(0.0127 cm kapton / 30.5536 cm L_r)
MULTIPLE-SCATTER   1.0 139.57 0.000415
ENERGY-LOSS-TARGET 1.0 139.57 6.0 12.0 0.018 0.018

(O O P S   D E T E C T O R   S Y S T E M)
(Note that the HDCs for the North Hall are off center. Future OOPS)
(modules will not be this way.)

DRIFT .050033
(The 1st HDC intersects the center of the focal plane)
RECTANGULAR-SLIT 1 6.5
RECTANGULAR-SLIT 3 14.0
(When we are reconstructing data or wish for some other reason to save)
(the standard focal plane variables, we must include a DETECTOR card here)
(since this is normal position in z for the focal plane variables.)
DETECTOR 0.03 3.0 0.03 3.0 (measurement errors: dx,dy = .03 cm ; dth,dph = 3 mr)

DRIFT .127
(The 2nd HDC)
RECTANGULAR-SLIT 1 7.0
RECTANGULAR-SLIT 3 15.5

DRIFT .127
(The 3rd HDC)
RECTANGULAR-SLIT 1 8.0
RECTANGULAR-SLIT 3 17.0

DRIFT .0753
(The 1st scintillator)
RECTANGULAR-SLIT 1 8.890
RECTANGULAR-SLIT 3 19.05

DRIFT .0508
(The 2nd scintillator)
RECTANGULAR-SLIT 1 8.890
RECTANGULAR-SLIT 3 19.05

DRIFT .0762
(The 3rd scintillator)

150

(The trigger requires that all three scintillators were hit.)
(Generally, we just check to see that the last scintillator was hit.)
RECTANGULAR-SLIT 1 8.890
RECTANGULAR-SLIT 3 19.05

(Put a detector card here to see if particles make it this far.)
(Call this the trigger.)
DETECTOR

APPENDIX C

Spectrometer Optical Matrix Files

C.1   OHIPS Matrix

```
52 3 2 3 3
0 0 0 0    0.000000e+00   0.000000e+00   0.000000e+00   1.938535e-01   0.0
0 0 0 1   -1.267869e-03   0.000000e+00   1.325505e-02  -8.322180e-01   0.0
0 0 0 2    6.239816e-04   0.000000e+00   0.000000e+00   0.000000e+00   0.0
0 0 0 3    0.000000e+00   0.000000e+00   0.000000e+00   1.231379e-04   0.0
0 0 1 0    0.000000e+00   0.000000e+00   6.710547e-01  -6.297513e-01   0.0
0 0 1 1   -2.992039e-03   0.000000e+00   1.579050e-03  -2.853596e-02   0.0
0 0 1 3    0.000000e+00   0.000000e+00   0.000000e+00   7.914541e-05   0.0
0 0 2 0    4.541789e-02  -1.118073e+00  -2.180714e-02   0.000000e+00   0.0
0 0 2 1    0.000000e+00  -3.504955e-02   1.746370e-03   0.000000e+00   0.0
0 0 2 2    0.000000e+00   0.000000e+00   0.000000e+00  -5.028442e-04   0.0
0 0 3 0    0.000000e+00   0.000000e+00  -2.434579e-02   0.000000e+00   0.0
0 1 0 0    5.152379e-03  -1.133238e+00   1.296169e-03   0.000000e+00   0.0
0 1 0 1    0.000000e+00   0.000000e+00   9.571353e-04  -2.223559e-03   0.0
0 1 0 2   -5.316158e-06  -8.734014e-05   3.501238e-06   0.000000e+00   0.0
0 1 1 0    0.000000e+00   0.000000e+00  -4.382927e-03   1.549087e-02   0.0
0 1 1 1    1.199851e-04  -2.450551e-03   0.000000e+00  -3.818136e-04   0.0
0 1 1 2    0.000000e+00   0.000000e+00   1.430925e-05  -2.218673e-05   0.0
0 1 2 0    0.000000e+00   1.522099e-02  -4.966423e-04   0.000000e+00   0.0
0 1 2 1    0.000000e+00   0.000000e+00  -8.747803e-05   0.000000e+00   0.0
0 1 3 0    0.000000e+00  -1.168400e-02   0.000000e+00   0.000000e+00   0.0
0 2 0 0    1.184838e-04   2.556376e-04   0.000000e+00   0.000000e+00   0.0
0 2 0 1    0.000000e+00   0.000000e+00  -2.042461e-05   4.969223e-05   0.0
0 2 0 2   -1.627104e-07  -2.648763e-06  -9.956304e-08   0.000000e+00   0.0
0 2 1 1    0.000000e+00   5.389251e-05   0.000000e+00   0.000000e+00   0.0
1 0 0 0    1.636224e-01   0.000000e+00   8.327217e-04   3.288646e-02   0.0
1 0 0 1    0.000000e+00   0.000000e+00   1.095388e-03  -2.941342e-03   0.0
1 0 0 2    0.000000e+00   5.665705e-05   2.928963e-06  -2.371182e-05   0.0
1 0 1 0    0.000000e+00   0.000000e+00  -6.961352e-03   0.000000e+00   0.0
1 0 1 1    1.432480e-04  -2.702544e-03   0.000000e+00   0.000000e+00   0.0
1 0 1 2    0.000000e+00  -1.240484e-04   1.263185e-05   3.002324e-05   0.0
1 0 2 0    0.000000e+00   0.000000e+00   8.624112e-04   0.000000e+00   0.0
```

152

```
1 0 2 1    0.000000e+00   0.000000e+00 -1.032449e-04   0.000000e+00   0.0
1 0 3 0    0.000000e+00   1.254965e-02  0.000000e+00   0.000000e+00   0.0
1 1 0 0    1.686436e-04   1.794103e-03 -2.142112e-05   0.000000e+00   0.0
1 1 0 1    0.000000e+00   0.000000e+00  0.000000e+00   2.868923e-05   0.0
1 1 0 2    2.058967e-07   0.000000e+00  8.883850e-08   0.000000e+00   0.0
1 1 1 0    0.000000e+00   0.000000e+00  0.000000e+00  -3.347802e-04   0.0
1 2 0 0    0.000000e+00   0.000000e+00  0.000000e+00  -4.851823e-06   0.0
1 2 0 1    0.000000e+00   0.000000e+00  1.803652e-07  -8.074026e-07   0.0
2 0 0 0   -1.504278e-04   0.000000e+00  0.000000e+00  -6.108416e-04   0.0
2 0 0 1    0.000000e+00   0.000000e+00 -4.657323e-06   6.486049e-05   0.0
2 0 0 2   -4.172655e-07   0.000000e+00  0.000000e+00   0.000000e+00   0.0
2 0 1 0    0.000000e+00   0.000000e+00  0.000000e+00  -2.619018e-04   0.0
2 0 1 1    4.849467e-06   0.000000e+00  0.000000e+00   0.000000e+00   0.0
2 0 2 0    0.000000e+00   0.000000e+00  2.701015e-05   0.000000e+00   0.0
2 1 0 0    0.000000e+00  -3.782938e-05  0.000000e+00  -8.881548e-06   0.0
2 1 1 0    0.000000e+00   0.000000e+00  0.000000e+00  -5.967351e-06   0.0
2 2 0 0   -7.723659e-08   0.000000e+00  0.000000e+00   0.000000e+00   0.0
3 0 0 0    1.111153e-06   0.000000e+00 -9.747761e-07  -3.538799e-05   0.0
3 0 0 1    0.000000e+00   0.000000e+00 -7.280191e-08   0.000000e+00   0.0
3 0 1 0    0.000000e+00   0.000000e+00  1.156274e-06   8.338098e-06   0.0
3 1 0 0    0.000000e+00   0.000000e+00  0.000000e+00  -9.553558e-08   0.0
x-offset: -6.191
th-offset: 791.6 1.7827 -0.003859
y-offset: 0.2502 -0.003391 -0.00001084
ph-offset: -0.2373 0.02441 -0.001268
```

153

C.2 OOPS A Matrix

```
24 3 3 3 1
0 0 0 0    0.000000e+00    0.000000e+00    0.0    9.776996e-02    0.0
0 0 1 0   -2.388618e-02   -2.705198e-02    0.0    1.187658e+00    0.0
0 1 0 0    3.277859e-03   -2.985041e-01    0.0   -3.313848e-03    0.0
0 1 1 0   -5.804615e-04    0.000000e+00    0.0    0.000000e+00    0.0
0 1 2 0    0.000000e+00    7.840903e-05    0.0    0.000000e+00    0.0
0 2 0 0    0.000000e+00   -5.580471e-05    0.0   -2.270254e-05    0.0
0 2 1 0    6.836248e-06    0.000000e+00    0.0    0.000000e+00    0.0
0 2 2 0    6.035775e-07    3.304346e-07    0.0    0.000000e+00    0.0
0 3 1 0    1.324237e-07    0.000000e+00    0.0    0.000000e+00    0.0
1 0 0 0    4.452631e+00    3.476126e-01    0.0    0.000000e+00    0.0
1 0 1 0    0.000000e+00   -7.073839e-03    0.0    2.683201e-02    0.0
1 1 0 0    2.205838e-02   -2.941670e-02    0.0    0.000000e+00    0.0
1 1 2 0   -2.572523e-05    0.000000e+00    0.0    0.000000e+00    0.0
1 2 0 0    8.530133e-05   -1.518219e-04    0.0    0.000000e+00    0.0
1 2 1 0   -2.578140e-06    0.000000e+00    0.0    0.000000e+00    0.0
1 3 0 0    0.000000e+00   -5.967521e-07    0.0    0.000000e+00    0.0
2 0 0 0   -3.244286e-01    5.355819e-02    0.0    0.000000e+00    0.0
2 0 1 0    4.554976e-03   -3.003891e-03    0.0    0.000000e+00    0.0
2 0 2 0    0.000000e+00    4.531638e-04    0.0    0.000000e+00    0.0
2 1 0 0   -2.537184e-03    6.816550e-03    0.0    0.000000e+00    0.0
2 1 1 0    8.123325e-05    0.000000e+00    0.0    0.000000e+00    0.0
2 2 0 0    0.000000e+00    3.720568e-05    0.0    0.000000e+00    0.0
3 0 0 0    3.927286e-02   -1.040289e-01    0.0    0.000000e+00    0.0
3 1 0 0    0.000000e+00   -6.108232e-04    0.0    0.000000e+00    0.0
x-offset:  0.674
th-offset: 0.0 -14.217 2.312
y-offset:  -0.701
ph-offset: -13.666
```

154

C.3 OOPS B Matrix

```
28 3 3 2 0
0 0 0 0    0.000000e+00    1.919029e-01    0.0    0.000000e+00    0.0
0 0 1 0   -1.758965e-02   -3.370156e-02    0.0    1.193715e+00    0.0
0 0 2 0    9.416457e-04   -4.093484e-03    0.0    0.000000e+00    0.0
0 1 0 0    5.874842e-03   -2.988193e-01    0.0   -4.396136e-03    0.0
0 1 1 0    0.000000e+00   -7.493271e-04    0.0    3.176559e-04    0.0
0 1 2 0   -5.432312e-05    1.248179e-04    0.0    4.480264e-05    0.0
0 2 0 0    0.000000e+00   -9.374003e-05    0.0   -2.378486e-05    0.0
0 2 1 0    2.013169e-06    4.402918e-06    0.0    0.000000e+00    0.0
0 2 2 0    0.000000e+00    1.336913e-06    0.0    4.934035e-07    0.0
0 3 0 0   -2.516612e-07    0.000000e+00    0.0    0.000000e+00    0.0
0 3 1 0    0.000000e+00    1.559653e-07    0.0    0.000000e+00    0.0
1 0 0 0    4.404693e+00    3.377328e-01    0.0    0.000000e+00    0.0
1 0 1 0    0.000000e+00    0.000000e+00    0.0    2.854176e-02    0.0
1 0 2 0    1.357485e-03   -1.970841e-03    0.0    0.000000e+00    0.0
1 1 0 0    1.995532e-02   -2.865233e-02    0.0    0.000000e+00    0.0
1 1 1 0   -8.350050e-05    0.000000e+00    0.0    2.049927e-04    0.0
1 1 2 0    0.000000e+00   -4.657969e-05    0.0    0.000000e+00    0.0
1 2 0 0    1.131628e-04   -1.264175e-04    0.0    0.000000e+00    0.0
1 2 1 0   -7.635233e-07   -2.524274e-06    0.0    0.000000e+00    0.0
1 3 0 0    5.279752e-07   -2.853204e-07    0.0    0.000000e+00    0.0
2 0 0 0   -2.804561e-01    0.000000e+00    0.0    0.000000e+00    0.0
2 0 1 0    4.257769e-03    0.000000e+00    0.0    0.000000e+00    0.0
2 0 2 0   -3.181752e-04    1.008707e-03    0.0    0.000000e+00    0.0
2 1 0 0   -2.399893e-03    5.316418e-03    0.0    0.000000e+00    0.0
2 1 1 0    6.160784e-05    0.000000e+00    0.0    0.000000e+00    0.0
2 2 0 0   -1.207788e-05    2.905214e-05    0.0    0.000000e+00    0.0
3 0 0 0    2.981360e-02   -9.793311e-02    0.0    0.000000e+00    0.0
3 1 0 0    0.000000e+00   -6.747594e-04    0.0    0.000000e+00    0.0
x-offset:  0.5678 0.0   0.0   0.0   0.0   0.0
th-offset: -1.0527 -13.46 2.5097 0.0   0.0   0.0
y-offset:  1.242 0.0   0.0   0.0   0.0   0.0
ph-offset: 1.808 0.0   0.0   0.0   0.0   0.0
```

C.4 OOPS C Matrix

```
14 3 2 1 2
0 0 0 0    0.000000e+00   0.000000e+00   0.0   0.000000e+00   0.0
0 0 0 1    4.213085e-02   0.000000e+00   0.0   1.618582e-01   0.0
0 0 1 0   -2.830856e-01   0.000000e+00   0.0   0.000000e+00   0.0
0 1 0 0    7.962561e-03  -2.956288e-01   0.0   0.000000e+00   0.0
1 0 0 0    4.440109e+00   0.000000e+00   0.0   0.000000e+00   0.0
1 0 1 0    0.000000e+00   0.000000e+00   0.0   4.392359e-02   0.0
1 1 0 0    2.160741e-02  -2.593087e-02   0.0  -6.501385e-03   0.0
1 1 0 2    0.000000e+00   0.000000e+00   0.0   1.329970e-06   0.0
1 2 0 0    7.911360e-05  -1.156371e-04   0.0   0.000000e+00   0.0
2 0 0 0   -2.427675e-01   0.000000e+00   0.0   0.000000e+00   0.0
2 0 1 1    0.000000e+00   0.000000e+00   0.0  -4.361272e-04   0.0
2 1 0 0   -1.680831e-03   3.409260e-03   0.0   0.000000e+00   0.0
2 2 0 0    0.000000e+00   0.000000e+00   0.0   2.725203e-05   0.0
3 0 0 0    2.068425e-02   0.000000e+00   0.0   0.000000e+00   0.0
x-offset:   0.6285
th-offset:  -0.613 -13.6 1.996
y-offset:   -1.633
ph-offset:  -5.7285
```